Dynamic Electro-Chemo-Mechanical Analysis at the Metal-Electrolyte Interface

Dem Promotionsausschuss der
Technischen Universität Hamburg-Harburg
zur Erlangung des akademischen Grades
Doktor-Ingenieur(in) (Dr.-Ing.)
genehmigte Dissertation

von

Qibo DENG

Aus

Guangxi, China

2014

This thesis is dedicated to the memory of my beloved father, Jiafa DENG.

Acknowledgements

This thesis is the end of my journey in obtaining my Ph.D. It would not have been possible to write this doctoral thesis without the help and support of the kind people around me, to only some of whom it is possible to give particular mention here.

First and foremost I would like to express my sincerest gratitude to my supervisor, Prof. Dr.-Ing. Jörg Weissmüller, for the continuous support of my Ph.D study and research, for his patience, motivation, enthusiasm, and immense knowledge. His guidance helped me in all the time of research and writing of this thesis. I could not have imagined having a better advisor and mentor for my Ph.D study.

The good advice, support and friendship of my previous colleague, Dr. M. Smetanin, has been invaluable on both an academic and a personal level, for which I am extremely grateful.

I acknowledge my gratitude to Prof. Dr. Schimmel at the Institute of Nanotechnology at Karlsruhe Institute of Technology and Prof. Dr.-Ing. Trieu at the Institute of Micro-System Technology at Hamburg University of Technology for using their facilities to prepare my experimental samples utilized in this thesis.

I also would like to express my deep gratitude to all of my colleagues and friends at Institute of Materials Physics and Technology, Hamburg University of Technology. Thanks to them for giving me the help and for sharing their knowledge. A critical reading by Dr. R. Günther and Dr.-Ing. D. Gosslar is gratefully acknowledged.

My time at Hamburg-Harburg was made enjoyable in large part due to the many friends that became a part of my life. I am grateful for time spent with my Chinese friends.

And many thanks to everyone who helped in any way contributing to this thesis.

I take this opportunity to sincerely acknowledge the China Scholarship Council (CSC) for giving me an opportunity to study in Germany and providing the assistance.

Finally, I want to thank my family for the patience, support and understanding.

Abstract

This thesis aims to describe experimentally the link between the mechanical deformation and the electrochemical processes on the surfaces of metal electrodes.

The experimental methods are firstly designed in this thesis to precisely measure the electrocapillary coupling coefficients between the electrochemical variables (*e.g.* electrode potential or reaction current) and elastic strain. These methods, Dynamic Electro-Chemo-Mechanical Analysis (DECMA), are validated as the measurement strategies to investigate the potential- and current- modulation in response to the cyclic elastic strain during a traditional cyclic voltammetry by three independent experimental methods: *i*) current-strain response at constant potential condition; *ii*) potential-strain response at constant charge density condition; and *iii*) potential-strain response at constant current condition. As one-case, DECMA is applied to study the coupling parameter of electrode potential and strain, ς_E, under the different conditions of metals surfaces and electrolytes.

Since the electrochemical variables for a strained electrode surface near equilibrium condition have been identified, theoretical and experimental methods can be taken one step further into the realm of non-equilibrium processes such as an electrocatalytic reaction.

The main target of this thesis is to experimentally investigate the mechanically modulated catalysis by monitoring the modulation of reaction current during the strain cycles on the electrode. As a model process, the experimental work is focused on the hydrogen evolution reaction (HER) on 111-textured, polycrystalline gold and platinum thin film electrodes. This is the first investigation of introducing the strain term into the reaction kinetic equations. The variation of the coupling coefficients, between reactivity of electrode and surface strain, with the electrode state in experiments agrees well with the model expectation. The results reveal the strain-dependence of the hydrogen adsorption enthalpy as well as the reaction activation enthalpy in the hydrogen evolution reaction.

This thesis describes that the reaction rate in heterogeneous catalysis varies considerably with the mechanical deformation when the surface is elastically strained in the tangent plane. This opens the perspective of tuning the elastic deformation - in other words, tuning the lattice parameter of surface atoms - of catalysts, so as to enhance their reactivities. The present approach in this thesis towards monitoring mechanically modulated reaction rates in electrocatalysis can be applied quite generally to the electrocatalytic reactions of interest. It thus evolves into a new tool for studying strain-dependent electrocatalysis and for linking the relevant phenomena to models of the underlying microscopic processes for the investigation of reaction mechanism.

Contents

List of Symbols

Symbol	Meaning	Unit
A	electrode area	cm^2
a_i	the chemical activity for species i	1
C	capacitance	μF
	concentration	mol
c	capacity	$\mu\text{F cm}^{-2}$
$C(0,t)$	species concentration at electrode surface	mol
C_d	double layer capacitance	$\mu\text{F cm}^{-2}$
C^*	species concentration in bulk solution	mol
E	electrode potential	V
e	mechanical strain	1
$\hat{E}$	amplitude of strain-induced potential variation	V
$\hat{e}$	amplitude of area strain	1
E^0	standard potential	V
$E^{0\prime}$	formal potential	V
E^{ad}	electrosorption potential	V
E_{eq}	equilibrium potential of reversible reaction	V
E_{oc}	open circuit potential	V
E_{zc}	potential of zero charge	V
$\Delta E, \eta$	overpotential relative to the equilibrium potential	V
F	Faraday constant	C mol^{-1}
f	surface stress	N/m
ΔG^0	change of standard Gibbs free energy	J cm^{-2}
G^{sl}	(Gibbs) excess free energy	J cm^{-2}
Δg^{ad}	change of adsorption free energy	kJ mol^{-1}
Δh^{ad}	change of adsorption enthalpy	kJ mol^{-1}
Δh^{ex}	change of activation enthalpy	kJ mol^{-1}
$\Delta h^{\text{a--a}}$	change of hydrogen-hydrogen interaction energy	kJ mol^{-1}
I	electrode current	A
$\hat{I}$	amplitude of strain-induced current variation	mA
I_0	exchange current	A
I_l	mass-transfer limiting current	A

j	electrode current density	A cm^{-2}
j_0, j^{ex}	exchange current density	A cm^{-2}
j^{F}	Faraday current density	A cm^{-2}
k^0	standard heterogeneous rate constant	cm sec^{-1}
k_a	rate constant of anodic process	cm sec^{-1}
k_c	rate constant of cathodic process	cm sec^{-1}
l_0	initial length of sample	cm
n	number of moles of a substance	
N_A	Avogadro constant	mol^{-1}
Q	total charge	μC
q	superficial charge density	μ C cm^{-2}
q_0	elementary charge	C
R	universal gas constant	J (mol K)$^{-1}$
R_{ct}	charge-transfer resistance	Ω
R_s	solution resistance	Ω
R_U	uncompensated resistance	Ω
Δs_0^{ad}	change of adsorption entropy	kJ mol^{-1}
T	absolute temperature	K
	periodic time of strain	sec
t	time	sec
$\mathbf{Z}$	electrochemical impedance	Ω
z	number of electrons participated in electrode reaction	
α	transfer coefficient (a measure of the symmetry of energy barrier)	
γ^{sl}	surface tension	N/m
Γ	superficial (excess) density of adsorbed ions	mol cm^{-2}
θ	coverage of hydrogen on metal surface	ML
θ_{eq}	coverage of hydrogen on metal surface at equilibrium condition	ML
Λ	coefficient of pseudo-capacitive current-strain response	mA
ι	coefficient of Faraday current-strain response	mA cm^{-2}
λ	enthalpy-strain coupling parameter	V
μ	chemical potential	J
ν	Poisson ratio	1
ω	frequency of cyclic strain	Hz
ς	electrocapillary coupling coefficient (ς_{E} or ς_{f})	V
ς_{E}	coefficient of potential-strain response	V
ς_{f}	coefficient of surface stress-charge density response	V
ς^{ad}	coefficient of potential-strain response for adsorption enthalpy	V
ς^{ex}	coefficient of potential-strain response for activation enthalpy	V
$\varsigma^{\text{a-a}}$	coupling coefficient for strain-dependence of H-H interaction	V
ψ	surface free energy density	J cm^{-2}

Chapter 1

Introduction

1.1 Background and motivation

Due to the several commercial applications, progress in catalysis can have a positive economic as well as environmental impact. More specifically, the automotive and power generation industries (*e.g.* fuel cells and hydrogen energy economy) benefit most directly from the field of new-style catalysis.

Catalysis is an action by a catalyst in chemical reactions. The *catalyst* can alter the rate of chemical reactions by changing the activation energy and then return to its original form without being consumed or destroyed at the end of the reactions. The types of catalysts are classified based on the ways catalysts work as: *i*) *Homogeneous catalyst* is that both catalyst and all reactants/products are in the same phase; and *ii*) *heterogeneous catalyst* means that the reaction system involves multi-phase, *e.g.* H_2 (gas) + O_2 (gas) → H_2O (liquid).

Heterogeneous catalysis has received an enormous amount of interest, both from an industrial and a scientific perspective. This is demonstrated by the 2007 Nobel Prize in Chemistry awarded to Professor Gerhard Ertl, who introduced surface science techniques to the field of heterogeneous catalysis leading to a deeper understanding of how chemical reactions take place at the surfaces [1–5], thereby bridging the gap between surface science and industrial catalysis. There are many aspects currently under investigation of how surface science significantly affects the activity of catalysts, *e.g.* particle size effect, surface strain effect, shape effect and composition effect [6–12].

Take gold metal as an example. Although bulk gold is practically quite inert, the strain effect has been studied by self-consistent density functional calculation, as one of the detailed three effects[1] which might make gold surface more chemically reactive [13]. Such surface strain can be achieved in experiment by the monolayer of foreign atoms epitaxy to different support substrates crystals, like the experimental studies in Refs. [8, 14, 15].

More recently, advanced materials for heterogeneous catalysis are often in form of bimetallic bulk or alloys [16–20]. In bimetallic or alloy catalysts, an active component is enriched in the surface layer of atoms. Core-shell nanoparticles provide an example for such graded systems [21–23]. An inherent feature of these catalysts is that the atoms of the active component at the surface do not, in generally, see the same interatomic spacing as in their elemental crys-

---

[1]The other two effects are the quantum-size effect and the step effect.

talline state. It implies that the enhanced catalytic activity originates from the enriched active component which is under tensile or compressive strain.

However, the electronic structure in the active layer at such surface is also affected by electron exchange with the underlying substrate (*ligand effect*), and this 'ligand effect' affects the reactivity simultaneously with the lattice parameter change (*strain effect*). Since these two effects are not readily separated, the impact of strain on the catalytic reactivity of materials surfaces is not usually observed in isolation. In fact, quantifiable measures for the reactivity-strain coupling strength have not been reported so far, nor are definitions for the coupling parameters established.

This dissertation directly addresses the question of interest about quantifiable measurement for the reactivity-strain coupling strength, which bridges the surface mechanics and electro-catalysis in material science.

The subsequent sections display the state-of-the-art in the relevant fields in detail.

1.1.1   State-of-the-art

As one of the most significant aspects on the enhancement of metal's catalytic activity, surface strain or surface mechanics has prompted a renewed interest and investigation in the field of catalysis.

Firstly, density function theory (DFT) calculations [24–29] suggested that reaction rates in heterogeneous catalysis can vary significantly when considering an elastically strained surface in the tangential plane. The notion of a tangential elastic strain is here synonymous with a change in the in-plane lattice parameter at the surface. The suggestion of a strain-dependent reactivity rested on computed values for the adsorption enthalpies of the reactants and for the energies of the transition states, which were found to be significantly modified on strained surfaces. The surface strain could induce a shift of the d-band center, which is an important part of the interaction energy. The d-band model of Hammer and Nørskov rationalized the finding, by numerical studies, that expansive lateral strain typically led to an enhanced binding [24, 26, 29].

That finding of strain-dependent enthalpies has been experimentally recently confirmed [15, 30–32]. Enhanced reaction rates on strained catalyst layers have indeed been demonstrated in experiments [33–36]. More specifically, Gsell *et al.* [30] have investigated experimentally the effect of local substrate strain on adsorption energy by scanning tunneling microscopy technique. The strain, introduced in the surface region, strongly influenced the strength of adsorption. They showed that the oxygen atoms preferred adsorbed in the regions with lateral expansion of Ru (0001) surfaces in comparison with unstrained surfaces, whereas it was weaker in the regions of lateral lattice dilatation. The authors suggested (in the literature [30]) that increased theoretical and experimental efforts were required to understand these strain effects in more details since the experimental evidence was not yet clear-cut.

Schlapka *et al.* [31] showed that the strain effect as well as the ligand effect on the CO adsorption energy, by a combination of experimental and theoretical methods. The lattice compression of the Pt monolayer by deposition on a Ru (0001) substrate, as well as the strong Pt-Ru interlayer coupling, led to a significant reduction of the CO adsorption energy, which was understood in terms of the d-band center downshift caused by both effects [31].

More recently, Kibler *et al.* [15] have experimentally tuned the reaction rates by lateral strain on a pseudomorphic palladium monolayer. They found that the shift of the hydrogen desorption

potential depended on the shift of the d-band center, due to the misfit lattice parameters (a static strain) by depositing Pd adlayer on top of different metal substrates. The current density of hydrogen desorption was also changed by such mismatch strain in the meantime.

However, in their novel experiments mentioned above, the strained monolayers were achieved by epitaxy to different support substrate crystals due to the misfit of metal lattice parameters. Thus it was still difficult to separate the strain effect and ligand effect on the shift of the d-band center or the change of properties in those experiments.

1.1.2 Electrocapillary coupling coefficient

This thesis aims to monitor the mechanical modulation of the electrosorption enthalpy as well as of the reaction current in an electrochemical reaction on a strained surface. Since the potential of electrosorption represents the adsorption enthalpy, one of the key coupling coefficients in this study between electrode processes and the mechanics is the response, ς_E, of the electrode potential to elastic strain, defined via $\varsigma_E = \mathrm{d}E/\mathrm{d}e|_q$. Here E denotes the electrode potential, q the superficial charge density, and e a tangential strain variable.

Further, the electrode potential in electrolyte environment at the potential of zero charge condition[1] is closely related to the electron work function[2] of the surface in vacuum. Therefore, ς_E agrees as well with yet another fundamental parameter, the response of the work function to the strain. *Ab initio* computation data [37–40] summarized the atomic and electronic relaxations in charged gold surfaces in vacuum and investigated the effect of tangential strain on the work function for a set of noble and transition metals. The authors evaluated the response value ς_E for Au (111) as -1.86 V and found moreover that such parameter varied strongly with the surface orientation and the surface material.

The experimental measurement of ς_E was first reported in an early work by Gokhshtein [41] (summarized by Valincius in Ref. [42]), who defined the response parameter. Gokhshtein pointed out a Maxwell relation and proposed the 'Estance' method as a technique for measuring $\varsigma_E(E)$. Yet, Gokhshtein's estance experiments did not see a detailed and comprehensive documentation in the literature, and key results remained either obscure - such as the numerical magnitude of ς_E and the procedure by which numbers were derived - or puzzling - such as the several sign changes of $\varsigma_E(E)$ in the potential range near the zero charge.

At equilibrium condition, the Maxwell relation explored by Gokhshtein equates ς_E to another thermodynamic parameter, the derivative of the surface stress, f, of the electrode with respect to its superficial charge density q. In other words, $\varsigma_E = \varsigma_f$, where $\varsigma_f = \mathrm{d}f/\mathrm{d}q|_e$. This Maxwell relation has been experimentally confirmed recently [43, 44].

Until recently, the confirmed quantitative experimental information on ς_E came from the measurements of ς_f. Experiments using cantilever bending or porous metal expansion yielded ς_f near the potential of zero charge between -1 V and -2.5 V for various metal surfaces in weakly adsorbing electrolytes [45–50].

In fact, despite the fundamental relevance of the strain-response of the electrode potential, the phenomenon has remained poorly explored to this day. Numbers for the related quantity $\mathrm{d}E/\mathrm{d}\sigma$ (where σ is a measure for tangential stress in the bulk, which scales with strain e),

---

[1]Potential of zero charge is defined as an electrode potential where there is no excess charge at the electrode surface, the electrode is at neutral condition. *cf.* section 2.1.2.

[2]Work function is the energy needed to move an electron from the Fermi level into vacuum.

reported based on partly more recent experiments, differ by several orders of magnitude and even by sign [43, 51, 52]. Therefore, a direct measurement of ς_E is desirable, especially in view of the nontrivial issue of equilibrium during real electrode processes.

Smetanin *et al.* [43, 53] developed a novel experimental approach of introducing the cyclic strain on the surface of a metal electrode under the open circuit condition[1]. The parameter of interest in their measurement was ς_E exactly and the strain was changed dynamically in opposite to the epitaxy approach used in Refs. [8, 14, 15, 31]. Thus one can clearly address the exact impact of surface strain on the electrode potential separating the ligand effect. However, such novel experimental approach of measuring ς_E is only available under the open circuit condition. If there is no open circuit condition, the electric current directly compensates the variation of potential, which is induced by the strain, under the function of potentiostat instrument.

The presence of this limitation is inconvenient to detect and quantify the value of ς_E for different electrode processes, for instance during a cyclic voltammetry. The approach designed by Smetanin *et al.* therefore needs to be improved further to remove this limitation.

1.2   Scope and structure of this thesis

This dissertation gives a direct answer of how to *in situ* monitor the mechanical modulation of catalytic reactivity for achieving a deeper understanding of the chemical reaction on a strained surface. It thus affords a new tool for studying the strain-dependent catalysis on material surfaces. With regard to the mechanical modulation of reactivity, the interdisciplinary investigation in this thesis focuses on the strain-induced variation of electrode potential and of reaction current. Based on these issues, new measurement strategies are successfully established to *in situ* detect and quantify the relevant coupling coefficients when the electrode is cyclically strained. These novel strategies remove the restriction of open circuit condition and introduce the potential control so as to access the domain of electrocatalytic reaction.

Prior to the quantifiable measurement for the reactivity-strain strength in an electrocatalytic reaction, the experimental methods – dynamic electro-chemo-mechanical analysis (DECMA) – are validated near the potential of zero charge at equilibrium condition. The strain-dependence of adsorption enthalpy thus can be quantified by acquiring the coupling coefficient of potential-strain response in an electrosorption process. Since the methods near equilibrium condition are identified, it can be taken one step further into the realm of non-equilibrium processes for studying the reactivity-strain strength in electrocatalytic reaction as a focus of this thesis. The structure of this thesis is arranged in following chapters:

Since electrochemical technologies are used as basic tool in this study, Chapter 2 gives an introduction to the fundamental principles of electrochemistry. Chapter 3 shows the experimental procedure in detailed description of sample fabrication, tools of sample characterization, electrochemical setup as well as measurement strategies.

DECMA is described and validated in Chapter 4 for precisely measuring the coupling of electrode potential to strain, $\varsigma_E(E)$, and the response of electrode current to strain of electrically conductive solids in aqueous electrolytes during a conventional cyclic voltammetry. By means of an example, the results for gold electrodes are reported within dominantly capacitive regions.

---

[1]Open circuit condition means no potential or current is being applied to the electrochemical experiment. Thus no external electric current flows between the electrodes. *cf.* section 2.1.2.

Three independent experiments are explored for separating the cyclic strain-induced variation of potential or current from the background signal. The finding is that the results of all three experiments are in quantitative agreement and $\varsigma_E(E)$ varies significantly with the electrode potential. Moreover, the impact of ions of the working solution on the behavior of potential-strain responses is investigated as well in different electrochemical systems; for instance, different electrolytes and different concentrations of electrolyte. At the end of Chapter 4, the method of measuring $\varsigma_E(E)$ is taken one step further to the electrosorption processes for different metal electrodes (*e.g.* Au, Pd and Pt) in weakly adsorbing electrolytes. Main part of results obtained in this chapter have been published in the journals of Refs. [44, 54, 55] and submitted to journal *Langmuir* for publication [56].

There are two major merits in the coming Chapter 5. It first introduces the strain-dependence into the kinetic rate equations for strained surfaces, and derives results for the variation of coupling-strength with the electrode state. Chapter 5 also describes a novel experimental scheme through a modified DECMA that allows *in situ* monitoring the strain-induced reactivity modulation in heterogeneous electrocatalysis due to the changes in the lattice parameter of electrode surface. A simple but typical reaction, hydrogen evolution reaction (HER), is focused on 111-textured polycrystalline Au and Pt thin film electrodes in H_2SO_4 solution as the most studied system in literature. Experimental results agree with the model which imposes generally the strain term into the reaction kinetics equations, consequently it brings us towards deeper understanding of electrocatalytic phenomena at metal-electrolyte interfaces, in which the impact of elastic strain on catalysis is governed by the strain-dependence of the hydrogen adsorption enthalpy as well as the reaction activation enthalpy in electrochemical reactions. The results in this chapter have been published in *Journal of Catalysis* [57].

Finally, this thesis is summarized in Chapter 6.

Chapter 2

Theoretical background

2.1 Fundamental description of electrochemistry

Since electrochemical techniques were used as basic tools through this thesis, general description of fundamental electrochemistry, *e.g.* structure of the electrified interface, is presented in the next paragraphs and mainly following the textbooks [58–61].

2.1.1 Electrochemical cell

Electrochemical cells consist of at least two electron conductors, usually metals called *electrodes*, in contact with ionic conductors, called *electrolytes*. Electrochemical cells with current flow can operate either as *galvanic cells*, in which chemical reactions occur spontaneously and chemical energy is converted into electrical energy, or as *electrolytic cells*, in which electrical energy is converted into chemical energy. The electrolytic cells are used in this thesis.

Three electrodes system

The *working electrode* (WE) of interest, which makes contact with the electrolyte, must apply the desired potential under control and facilitate the charge transfer to and from the electrolyte. A second electrode acts as the other half of the electrochemical cell. This second electrode must have a known potential to gauge the potential on the working electrode, furthermore it also must balance the charge added or removed by the working electrode. However, it is extremely difficult for an actual electrode to maintain a constant potential while passing current to counter redox events at the working electrode.

To solve this problem, the role of supplying electrons and referencing potential has been divided into two separate electrodes. In this arrangement, the *reference electrode* (RE) is a half cell[1] with a known electrode reduction potential[2]. Its role is to only act as reference in measuring and controlling the potential on the working electrode and there is no current flow on

---

[1] A half-cell is half of an electrolytic or galvanic cell, where either oxidation or reduction occurs, *e.g.* $AgCl(solid) + e^- \rightleftharpoons Ag(solid) + Cl^-$. The half-cell reaction at the anode is oxidation, while it is reduction at the cathode .

[2] The value of reduction potential is relative to the standard hydrogen electrode, $2H^+_{aq} + 2e^- \rightleftharpoons H_2$, which is declared to be zero for forming a basis in comparison with all other electrode reduction reactions.

it. The *counter* or *auxiliary electrode* (CE) passes all the current needed to balance the current observed at the working electrode. The counter electrode can be any convenient one with larger surface area than the working electrode, since its electrochemical properties do not affect the behavior of the WE of interest. It is usually chosen to be an electrode that does not produce substance by electrolysis that will reach the surface of the WE and cause interfering reactions there.
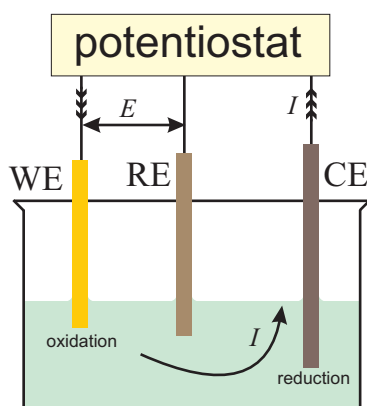

Figure 2.1: Schematic representation of a three electrodes electrochemical cell and circuit, showing the working electrode (WE), reference electrode (RE) and counter electrode (CE). The potential E at the WE relative to the RE is controlled by the potentiostat and the electrical current I flows from the WE to the CE in electrolyte.

These electrodes – the working, reference, and counter – make up the modern three electrodes system, as shown in Fig. 2.1. Such a three electrodes cell is usually required in the work with a potentiostat instrument, which is used to measure the potential difference between the working electrode and the reference electrode. The potentiostat has a high input impedance connected with the reference electrode, so that a negligible current is drawn through the reference electrode. This thesis adopts the three electrodes system in all electrochemical measurements.

Polarisable and nonpolarisable electrodes

A metal electrode at which no charge transfer can occur across the metal-solution interface, regardless of the potential imposed by an outside source of voltage, is called an *ideal polarizable electrode* (IPE). While no real electrode can behave as an IPE over the whole range of potential windows available in a solution, some electrode-solution systems can approach ideal polarisable condition over limited potential ranges. The only reaction current, generated by the reduction or oxidation, that flows in this region is due to charge-transfer reactions of trace impurities (*e.g.*, metal ions, oxygen, and organic species), and this current is quite small in clean systems. In contrast to IPE, an electrode whose potential does not change upon passage of the current is called an *ideal nonpolarisable electrode* (INPE). Typical such electrodes with fixed potential are the reference electrodes. Figure 2.2 illustrates a schematic representation of IPE and INPE.

The relevant electrocapillary coupling coefficients are focused on a polarisable electrode in this thesis. In Chapter 4 below an extreme case of nonpolarisable electrode is comparatively

investigated for the deeper understanding of the different behavior of potential-strain response; for instance, a metal in contact with an electrolyte containing the same metal ion in solution.

a) ideal polarizable electrode   b) ideal nonpolarizable electrode
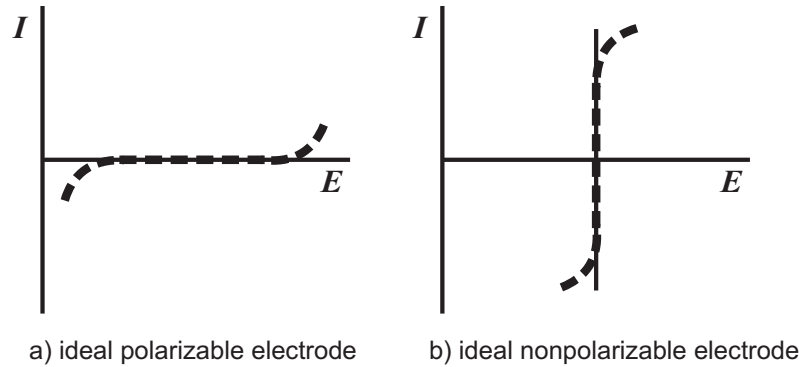
Figure 2.2: The steady-state current-potential curves for ideal **a)** polarisable and **b)** nonpolarisable electrodes. Dashed lines show behavior of actual electrodes that approach the ideal behavior over limited ranges of current or potential. Adapted from Ref. [58].

Residual potential drop between electrodes
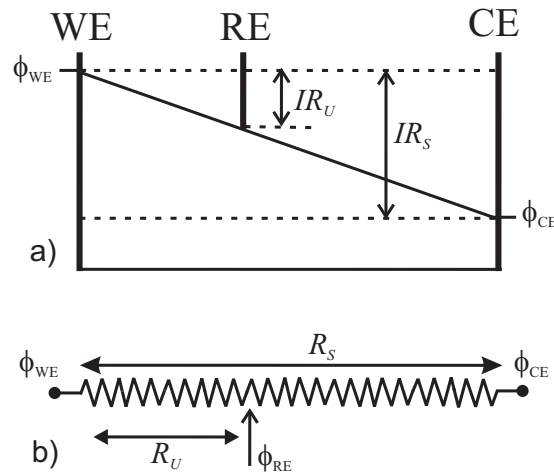
Figure 2.3: **a)** Schematic representation of residual potential drop between electrodes in solution and IR_U measured at the reference electrode; **b)** representation of the three-electrodes cell as a potentiometer. The symbols have following meaning: ϕ_* - potential on the considered electrodes (WE, RE and CE), I - electrode current, R_S - solution resistance between the WE and the CE, R_U - uncompensated resistance between the WE and the RE. Adapted from Ref. [58].

Considering the potential profile in solution between the working and counter electrodes, shown schematically in Fig. 2.3 a), the solution between these two electrodes can be regarded as a potentiometer. If the reference electrode is placed anywhere but exactly at the electrode surface, *residual potential* with definition as IR_U, where R_U is the *uncompensated resistance*

and I denotes the electrode current flowing from the working electrode to the counter electrode, will be included in the measured potential, see Fig. 2.3 b). Even when the tip of the reference electrode is designed for very close placement to the working electrode (*e.g.* use of a fine tip called a *Luggin-Haber capillary*), such design can decrease the effect of IR_U, but not totally eliminate it. Apart from that, some uncompensated resistance usually remains since the distance still remains between the working electrode and the reference electrode. This uncompensated potential drop can be removed later, for example, from steady-state measurements by measurement of R_U and point-by-point correction of each measured potential.

All electrode potentials are corrected for the potential drop in solution by subtracting $I(E)R_U$ from the nominal electrode potential value when studying the mechanically modulated catalysis due to the rather large current in the reaction zone.

2.1.2 Structure of the electrified interface

A common example of an electrochemical system is that of an impermeable interface between a metal and a solution containing ions, where the species (charge carriers) ensures the current flow at each side of the interface but cannot traverse it. In fact, electrochemistry concerns with the interrelation of electrical and chemical effects and reactions that involve reactant and electron. Chemical changes can be caused by the passage of current. The electrochemical reactions occur at the electrified interface of metal-electrolyte. This part of principle and description about the structure of an electrified interface is adapted from Ref. [58].

Electrical double layer

Since charge cannot cross the ideal polarized electrode interface when the potential is changed, the behavior of the electrode-solution interface is analogous to that of a capacitor. The charge is governed by the equation, $Q = CE$, where Q is the total charge stored on the capacitor, E is the electrode potential and C is the capacitance. At a given potential, there will exist a charge on the metal electrode, Q^M, and a charge in the solution, Q^S. The charge on the metal is negative or positive depending on the potential across the interface and the composition of the solution. At all times, however, $Q^M = - Q^S$.

The charges Q^M and Q^S are often divided by the electrode area, A, and expressed as charge densities, $q^M = Q^M/A$, given in unit of $\mu C \text{cm}^{-2}$. The whole array of charged species and oriented dipoles existing at the metal-solution interface is called the *electrical double layer*.

As illustrated in Fig. 2.4, the electrical double layer has a complex structure of several distinct parts according to the Gouy-Chapman theory [62–64]. The solution side of the interface consists of a compact layer (inner and outer Helmholtz layers) plus a diffuse layer. The *inner Helmholtz layer* or *inner Helmholtz plane* (IHP), close to the electrode, contains solvent molecules and specifically adsorbed ions which are not solvated fully. Such inner layer is defined by the location of the specifically adsorbed ions, which is at a distance x_1. The total charge density from specifically adsorbed ions in this inner layer is q^i ($\mu C \text{cm}^{-2}$). The next layer, the *outer Helmholtz layer* (OHP), reflects the imaginary plane passing through the center of solvated ions at their closest approach to the surface; this means that solvated ions can approach the metal only to a distance x_2. The solvated ions are nonspecifically adsorbed and are attracted to the surface by long-range coulombic forces, so that their interaction is essentially indepen-

dent on the chemical properties of the ions. Both Helmholtz layers represent the *compact layer*, also called the *Helmholtz layer*, or *Stern layer*.

Because of thermal agitation in the solution, the nonspecifically adsorbed ions are distributed in a three-dimensional region called the *diffuse layer*. The diffuse layer, beyond the compact layer, extends from OHP to bulk solution. The excess charge density in the diffuse layer is q^d, hence the total excess charge density on solution side of the double layer, q^S, is given by $q^S = q^i + q^d = - q^M$.
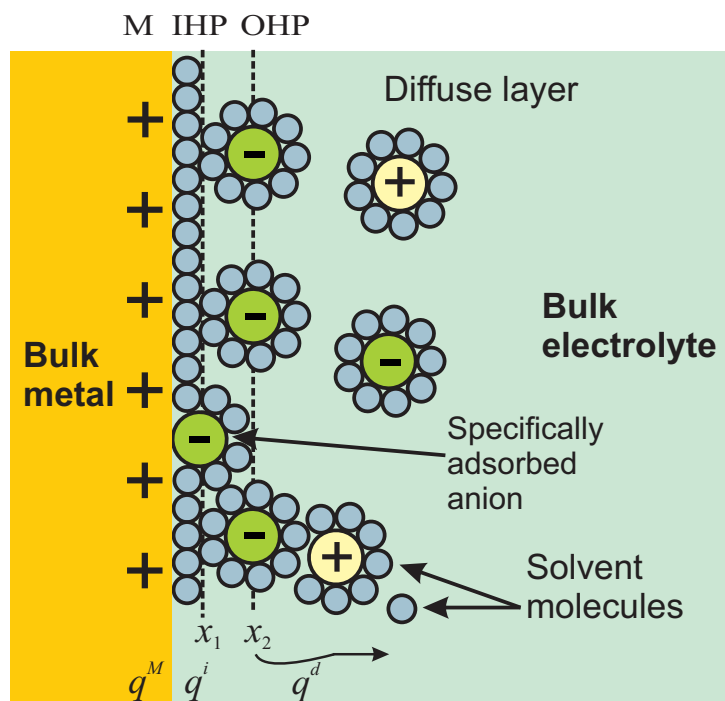
Figure 2.4: Simplified scheme of the electrified double layer region under conditions where anions are specifically adsorbed: compact and diffuse layers with solvated cations and anions in the electrolyte. M = metal surface; IHP = inner Helmholtz layer (at a distance x_1 from the metal surface); OHP = outer Helmholtz layers (at a distance x_2 from the metal surface). Symbols q^M, q^i and q^d denote the total charge density at the metal surface, the inner layer and the diffuse layer, respectively. Adapted from Ref. [58].

Potential of zero charge

The *potential of zero charge* (*pzc*), a fundamental property of the metal-electrolyte interface, is defined as an electrode potential where there is no excess charge at the electrode surface, usually with the symbol E_{zc}. If the electrode potential is positive in relation to *pzc*, then negative ions (anions) are attracted to the metal surface from the electrolyte; if it is negative in relation to *pzc*, then positive ions (cations) are attracted.

Since at the *pzc* the surface tension reaches a maximum value, and the electrical capacitance at the boundary shows a minimum peak, one method to determine the *pzc* is measuring the

minimum peak of differential capacitance during potential sweep. This thesis would provide an alternative and useful probe of the *pzc* of gold.

Open circuit potential

The *open circuit potential* (*ocp*) is the potential of the working electrode relative to the reference electrode when no potential or current is being applied to the cell. Thus no external electric current flows between the electrodes. It is given by the symbol E_{oc}. The metal-solution interface determines the value of the *ocp*, *eg.* the metal materials, the concentration of electrolytes. The *ocp* can be measured using high-input impedance voltmeters, or potentiometers, as in potentiometry.

One major merit in this thesis is to remove the limitation of the open circuit condition and to impose the potential control for measuring the parameter of potential-strain response.

2.1.3   Faradaic and non-faradaic processes

With a phenomenological thermodynamics description, the potential-strain response in this study is a key parameter connecting electrode process to the mechanics. There are two types of processes occurring at electrodes. One type participates in electrochemical reactions where charges (*e.g.*, electrons) are transferred across the metal-electrolyte interface. Electron transfer causes electrochemical reactions (oxidation or reduction) to occur. Since such reactions are governed by Faraday's law (*i.e.*, the amount of the chemical reaction caused by the flow of current is proportional to the amount of electricity passed), they are called *faradaic processes*. The *faradaic current* is the current that corresponds to the electrolytic oxidation or reduction of one or more chemical species at an electrode.

Under some conditions, at a given electrode-solution interface there is a range of potentials where no charge-transfer reactions occur because such reactions are thermodynamically or kinetically unfavorable. However, processes such as adsorption and desorption can occur, and the structure of the electrode-solution interface can change with changing potential or solution composition. These processes are called *nonfaradaic processes*.

The current in nonfaradaic processes flowing through an electrochemical cell is charging or discharging the electrical double-layer capacitance. This current does not involve any electrochemical reactions (charge transfer). It only causes accumulation or removal of electrical charges on the electrode and in the solution near the electrode. There is always some capacitive current flowing when the potential of an electrode is changing, and the capacitive current is generally zero when the potential is constant. It is also called *nonfaradaic* or *double-layer current*, in contrast to the faradaic current. Although charge does not cross the interface, external currents can flow when the potential, electrode area, or solution composition changes. Both faradaic and nonfaradaic processes occur when electrode reactions take place.

Electrode Reaction and Electron transfer

Figure 2.5 describes the processes occurring in a simple electrode reaction. It contains four processes:

i) Mass transfer of the reactant (or product) to and away from the electrode interface;

ii) Proceeding or follow-up chemical reactions;

iii) Surface adsorption or desorption processes;

iv) Electron transfer at the electrode-solution interface.

In the case of reduction, a species (O), capable of receiving an electron diffuses to the surface, receives an electron from the electrode and diffuses away from the surface. Current at the surface is generated by the transfer of electrons from the electrode to the redox species. In solution the current is carried by migration of ions.
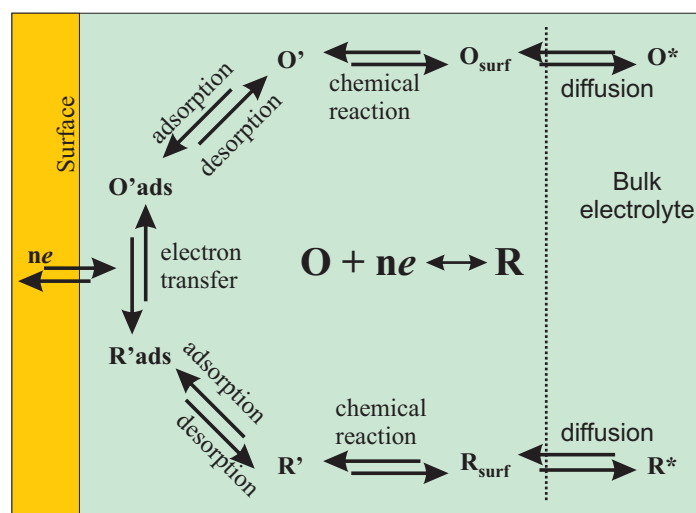

Figure 2.5: Pathway of a general electrode reaction. Adapted from Bard [58].
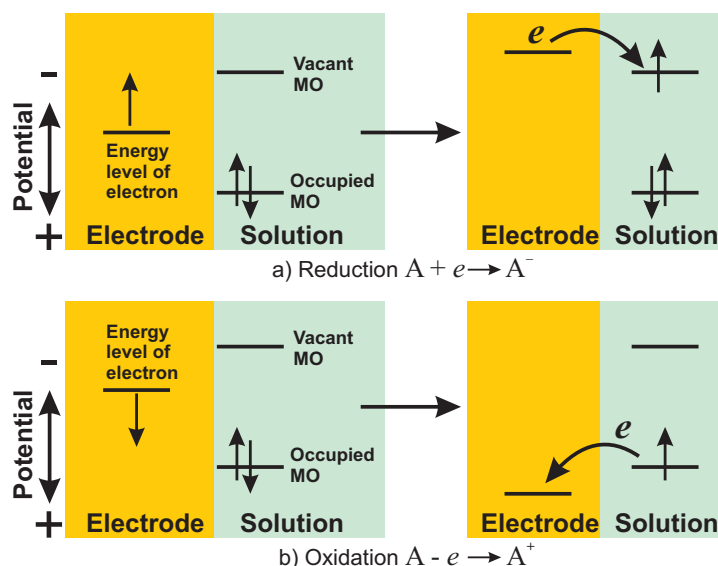

Figure 2.6: Schematic representation of an electrode reaction: **a)** reduction and **b)** oxidation process of a species, A, from solution. The molecular orbitals (MO) of species A shown in figures are the highest occupied MO and the lowest vacant MO. Adapted from Ref. [58].

The magnitude of the potential controls the direction and rate of charge transfer. As illustrated in Fig. 2.6, by driving the potential of the electrode more negatively (*e.g.* by connecting a battery or a power supply to the electrochemical cell with its negative side connected to the working electrode), the energy of the electrons in the electrode increases, thereby the electrons are given sufficient energy to occupy vacant states on the species in the electrolyte. In that case, a flow of electrons occurs from an electrode to solution called *reduction current*. Similarly, by driving the potential more positively, the electrons in the electrode loose energy, thereby making it possible for electrons from species in the electrolyte to lower their energy by transferring to the electrode. Their flow, from solution to electrode, is an *oxidation current*.

2.1.4 Mass transport

The rate of charge transfer can be increased drastically by increasing the electrode potential, but charge can be transferred over a very short distance (of the order of 0.5 nm in inner Helmholtz layer) in the form of an electron only. Another process is required to bring the reacting species close enough to the surface, and to remove the species formed at the surface into the bulk of solution. This process is called *mass transport* [61]. The mass transport phenomena can be macroscopically described with three types of driving forces, roughly portrayed as migration, convection and diffusion accompanying an electrode reaction [58, 59]. In electrochemistry, the region in which diffusion cannot be neglected, compared to other mass transport mechanisms, is known as the diffusion layer.

2.2 Fundamental equations

The ability to predict how a system will behave under certain conditions is essential in an electrochemical experiment. In this regard, the fundamental equations described in this section can be quite useful and mainly adapted from the handbooks of Refs. [58, 61, 65–67].

2.2.1 Faraday's law

Faraday's law of electrolysis that governs the electrochemical reactions can be stated as follows. The number of moles of a substance, n, consumed or produced at one of the electrodes in an electrolytic cell is directly proportional to the electric charge passed through the electrode, Q. Assuming that there are no parallel processes,

$$Q = nzF, \tag{2.1}$$

where z and F are the number of electrons appearing in the electrode reaction equation and the Faraday constant (96 485 C mol^{-1}), respectively. The constant F has a simple relation to two other physical constants:

$$F = q_0 N_A, \tag{2.2}$$

where N_A is the Avogadro constant with value of 6.022×10^{23} mol^{-1} and q_0 is the elementary charge of 1.602×10^{-19} C.

2.2.2 Nernst equation

For an electrode reaction, the equilibrium condition is characterized by the Nernst equation, which links the euilibrium potential of a reversible reaction to the concentration of electroactive species (participants). For simplicity, we only consider a single electron transfer reaction (here $z = 1$) between oxidized species (O) and reduced species (R):

$$O + e^- \rightleftharpoons R. \tag{2.3}$$

In an electrochemical cell, the cell potential relates to the Gibbs free energy change:

$$\Delta G = -FE. \tag{2.4}$$

Here E is the cell potential (electromotive force) relative to reference electrode, also known as open circuit potential (E_{oc}) or equilibrium potential (E_{eq}), which is present when no current is flowing through the cell, and F is the Faraday's constant. If the reactant and product have unit activity[1] (*i.e.* at standard states) and E is for the reaction in the reduction direction (from left to right in Eq. 2.3), then we have

$$\Delta G^0 = -FE^0. \tag{2.5}$$

In this case, the potential is known as the *standard electrode potential* (E^0 [V]) or the *standard potential* and it relates to the *standard Gibbs free energy change* (ΔG^0 [J mol^{-1}]). It should be noted here that due to the minus sign, all spontaneous reactions (*i.e.* with $\Delta G^0 < 0$) will have a positive standard electrode potential ($E^0 > 0$).

At given time t, the concentrations of oxidized species is expressed as $C_O(0,t)$ and of reduced species as $C_R(0,t)$ at the electrode surface. The relationship between the surface concentrations and free energy change is given as [58, 65][2]:

$$\Delta G = \Delta G^0 + RT \ln \frac{a_R}{a_O} = \Delta G^0 + RT \ln \frac{C_R(0,t)}{C_O(0,t)}, \tag{2.6}$$

where R is the gas constant (8.3145 J mol^{-1} K^{-1}), a_i is the chemical activity for the relevant species i and T [K] is the absolute temperature. The critical aspect of this equation is that the ratio of reduced to oxidized species can be related to the Gibbs free energy change.

The mathematical expression describing the correlation between equilibrium potential and concentration for a cell reaction is a central tenet of electrochemistry and is known as the *Nernst equation*:

$$E_{eq} = E^0 + \frac{RT}{F} \ln \frac{C_O(0,t)}{C_R(0,t)}. \tag{2.7}$$

The Nernst equation solves the potential of an electrochemical cell containing a reversible system with fast kinetics, and it is valid only at equilibrium, and it can be applied at the surface of

---

[1]The activity of a species i, denoted a_i, is defined as [68]: $a_i = \exp \frac{\mu_i - \mu_i^0}{RT}$, where μ_i is the chemical potential of the species under the conditions of interest, μ_i^0 is the chemical potential of that species in the chosen standard state, R is the gas constant and T is the absolute temperature.

[2]The symbols here a_R and a_O are the chemical activity for reductant and the oxidant, respectively. $a_i = \Upsilon_i C_i$, where Υ_i is the activity coefficient of species i. Since activity coefficients tend to unity at low concentrations C_i, activities are frequently replaced by simple concentrations [69].

the electrode. The equation (2.7) can be written in a more general case[1]:

$$E_{eq} = E^{0\prime} + \frac{RT}{F} \ln \frac{C_O^*}{C_R^*} = E^{0\prime} + 2.303 \frac{RT}{F} \log \frac{C_O^*}{C_R^*}, \tag{2.8}$$

where $E^{0\prime}$ is the formal potential, and C^* is the bulk concentration for the considered species. At room temperature (25 °C), the term 2.303 RT/F may be treated like a constant and replaced by 59.2 mV for cells. The equilibrium potential of a reversible reaction is thus shifted with the logarithm of the concentration of electrolyte in use as indicated by that value of 59.2 mV.

2.2.3 Current-overpotential equation

The content above section predicts the equilibrium potential of a reversible reaction. Moreover, the potential of an electrode strongly affects the kinetics of reactions occurring on the surface. This part of fundamental concepts is adapted from Ref. [58] to represent the relationship between the kinetic rate and electrode potential in a general electrode reaction, considering only one electron transfer (*cf.* Eq. 2.3).

In electrochemistry, the physical variable overpotential, η (or ΔE), is used rather than the electrode potential, E. The *overpotential* is defined as

$$\eta = E - E_{eq}, \tag{2.9}$$

where E_{eq} is the equilibrium potential of one reversible reaction. This is the extra voltage which drives a Faradaic current. The constant of proportionality linking the cathodic reaction (reduction) rate to $C_O(0,t)$ is the rate constant k_c. The reaction rate for the cathodic process is

$$v_c = k_c C_O(0,t). \tag{2.10}$$

Since the cathodic reaction is a reduction, there is a *cathodic* (reduction) *current*, I_c:

$$I_c = -FAv_c = -FAk_c C_O(0,t). \tag{2.11}$$

Likewise, we have a reaction rate of anodic reaction:

$$v_a = k_a C_R(0,t), \tag{2.12}$$

and the anodic component to the total current I_a is:

$$I_a = FAv_a = FAk_a C_R(0,t). \tag{2.13}$$

Thus, the net overall reaction current is

$$I = I_a + I_c = FA[k_a C_R(0,t) - k_c C_O(0,t)], \tag{2.14}$$

---

[1]Standard conditions for E^0 are T = 298 K, pH = 0 and unit activity. Non-standard conditions or conditions where the activities of oxidized species and reduced species are affected by the medium, then formal potential is used, $E^{0\prime}$, which presents both the oxidized and the reduced species in unit concentration instead of unit activity and depends on the nature of electrolytes in the solution.

where A is the electrode area in above equations.

The reaction rate constants can be written as a function of the standard heterogeneous rate constant, k^0 [cm sec^{-1}], with a charge transfer coefficient, α:

$$k_c = k^0 e^{-\alpha f(E-E^{0'})}, \tag{2.15}$$

$$k_a = k^0 e^{(1-\alpha)f(E-E^{0'})}; \tag{2.16}$$

where the coefficient $f = F/(RT)$, formal potential $E^{0'}$ is the same as in Eq. 2.8 and the transfer coefficient or symmetry factor, α, is a dimensionless parameter with values between 0 and 1, and is often estimated to be 1/2 [58]. The transfer coefficient is a measure of the symmetry of the energy barrier. This transfer coefficient has significance in the kinetic rate of an electrochemical reaction.

By combining the equations (2.14), (2.15) and (2.16) above, the current of the reaction may be described by the complete current-potential characteristic:

$$I = FAk^0[C_R(0,t)e^{(1-\alpha)f(E-E^{0'})} - C_O(0,t)e^{-\alpha f(E-E^{0'})}]. \tag{2.17}$$

This equation is the basis for all accounts of heterogeneous electrode kinetics. In view of the equations (2.8), (2.9) and (2.17), we can obtain

$$I = I_0\Big[\frac{C_R(0,t)}{C_R^*}e^{(1-\alpha)F\eta/RT} - \frac{C_O(0,t)}{C_O^*}e^{-\alpha F\eta/RT}\Big], \tag{2.18}$$

with

$$I_0 = FAk^0(C_O^*)^{1-\alpha}(C_R^*)^{\alpha},$$

where I_0 is the *exchange current* in a dilute solution. This equation (2.18) is known as the *current-overpotential equation*, with the first term describing the anodic component current at any overpotential, and the second showing the cathodic contribution.

The behavior predicted by Eq. 2.18 is depicted in Fig. 2.7. The solid curve shows the actual total current, which is the sum of the component I_a and I_c shown as dashed traces. For a large negative overpotential, the anodic component is negligible; hence the total current curve merges with that for I_c. At a large positive overpotential, the cathodic component is negligible, and the total current is essentially the same as I_a. In going either direction from E_{eq}, the magnitude of the current rises rapidly, since the exponential factors dominate the behavior.

However at extreme η, the current levels off. In these level overpotential regions, the current is limited by mass transfer rather than heterogeneous kinetics. The exponential factors in Eq. 2.18 are then moderated by the factors $C_R(0,t)/C_R^*$ and $C_O(0,t)/C_O^*$, which manifest the reactant supply. The feature of *limiting current*, I_l, is independent of the overpotential. Since the experiments in this thesis do not approach the region of mass-transfer limit, the mass-transfer effect is neglectable. The next few paragraphs with subtitle show approximate forms of the current-overpotential equation in different cases, which are relevant for the experiments below.

Exchange current

When an electrochemical cell is at equilibrium there is no net current ($I = 0$). From Eq. 2.17 we then have, at zero current,

$$FAk^0[C_R(0,t)e^{(1-\alpha)f(E_{eq}-E^{0'})}] = FAk^0[C_O(0,t)e^{-\alpha f(E_{eq}-E^{0'})}]. \tag{2.19}$$
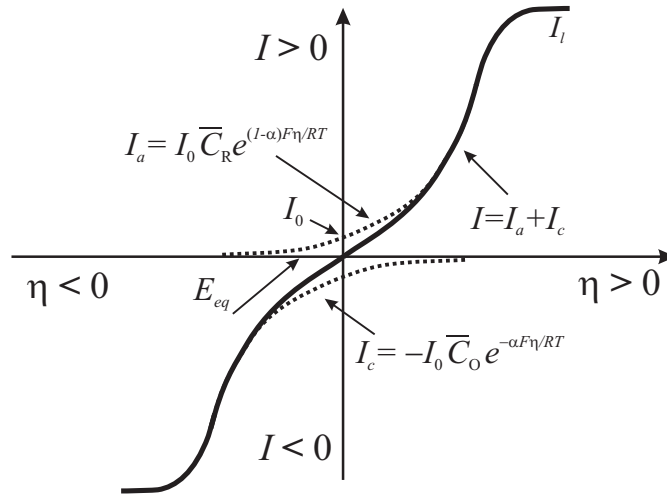
Figure 2.7: Current-overpotential curves for reaction $O + e^- \rightleftharpoons R$ with overpotential $\eta = E - E_{eq}$. The dashed lines show the anodic and cathodic current as I_a and I_c, respectively, where $\overline{C}_R = C_R(0,t)/C_R^*$ and $\overline{C}_O = C_O(0,t)/C_O^*$ in the figure. The limiting current I_l is due to the effect of mass transfer.

Since equilibrium applies, the bulk concentration of O and R are found also the same at the surface, means $C_O(0,t) = C_O^*$ and $C_R(0,t) = C_R^*$; hence

$$e^{f(E_{eq}-E^{0'})} = \frac{C_O^*}{C_R^*}, \tag{2.20}$$

which is simply an exponential form of the Nernst relation (see Eq. 2.7).

Since the net current is zero at equilibrium, the system contains a cathodic current balanced by an equal and opposite anodic current. The balanced faradaic current can be expressed in terms of the exchange current, I_0 in magnitude to either the component current, I_a or I_c. That is

$$I_0 = I_a = -I_c = FAk^0 C_O^* e^{-\alpha f(E_{eq}-E^{0'})}. \tag{2.21}$$

Thus, the exchange current is:

$$I_0 = FAk^0 (C_O^*)^{1-\alpha} (C_R^*)^{\alpha}. \tag{2.22}$$

Often the exchange current is normalized to unit area to provide the *exchange current density*, usually with the symbol j_0 or j^{ex}, $j_0 = I_0/A$. The exchange current density is the rate of reaction at the reversible potential (when the overpotential is zero by definition, it is also called equilibrium potential). At the reversible potential, the reaction is in equilibrium meaning that the forward and reverse reactions progress are at the same rates. This rate is the exchange current density.

No mass-transfer effects

If the solution is well stirred, or currents are kept so low that the surface concentrations ($C(0,t)$) do not differ appreciably from bulk values (C^*), then the current-overpotential equation (Eq.

2.18) reduces to the *Butler-Volmer equation*:

$$I = I_0\big[e^{(1-\alpha)F\eta/RT} - e^{-\alpha F\eta/RT}\big]. \tag{2.23}$$

The Butler-Volmer equation can be used to predict the current that results from an overpotential when mass-transfer limitations are eliminated. It describes how the electrical current on an electrode depends on the electrode potential (precisely, overpotential), considering that both a cathodic and an anodic reaction (or a reversible reaction) occur on the same electrode.

Linear Response

For small values of x, the exponential e^x can be approximated as $1 + x$; hence for a sufficiently small overpotential η, Eq. 2.23 can be reexpressed as

$$I = I_0 F\eta/RT, \tag{2.24}$$

which shows that the net current is linearly related to the overpotential in a narrow potential range near E_{eq}. The ratio η/I has units of resistance and is often called the *charge-transfer resistance*, R_{ct}:

$$R_{ct} = \frac{RT}{FI_0}. \tag{2.25}$$

Tafel equation

For large values of η, one of the bracketed terms in Eq. 2.23 becomes negligible. For example, at large negative potentials, the Eq. 2.23 can be simplified as

$$I = -I_0 e^{-\alpha F\eta/RT} \tag{2.26}$$

or

$$\eta = \frac{RT}{\alpha F}\ln I_0 - \frac{RT}{\alpha F}\ln|I| = a + b \times \log|I|, \tag{2.27}$$

where $b = 2.303RT/(\alpha F)$ is the so called *Tafel slope*. A graphic representation of $\log|I|$ *vs.* η is known as a *Tafel plot*. The value of Tafel slope is used in this thesis to determine the reaction mechanism of hydrogen evolution reaction when studying the strain-dependent catalysis.

2.2.4   Impact of strain on electrocapillarity

This subsection mainly follows the content of Ref. [70] to present the idea of how surface strain takes a significant contribution into Gibbs free energy. A simple special case here is inspected so as to highlight the essential physics. In Ref. [70, 71] the detailed analysis of the mechanics of electrodes starts from first principles and allows for general geometries and processes.

As illustrated in Fig. 2.8, a patch of electrode surface is formed where a droplet of liquid electrolyte wets a planar metal surface. The net free energy of the system (electrolyte plus metal) may be decomposed into contributions from the bulk solid and liquid and from the various interfaces. The excess free energy (or called *Gibbs free energy*), $G^{sl} = \gamma^{sl}A$, is associated with the (solid-liquid-) electrode surface of Lagrangian area A and surface tension γ^{sl}.

Specifically, the variation, δG^{sl}, of that quantity is inspected when the physical surface area, $\overline{A}$, of the electrode is increased by the relative amount ε while the electrode potential, E, is held constant. The process under consideration achieves the variation of $\overline{A}$ in the way of elastic strain.
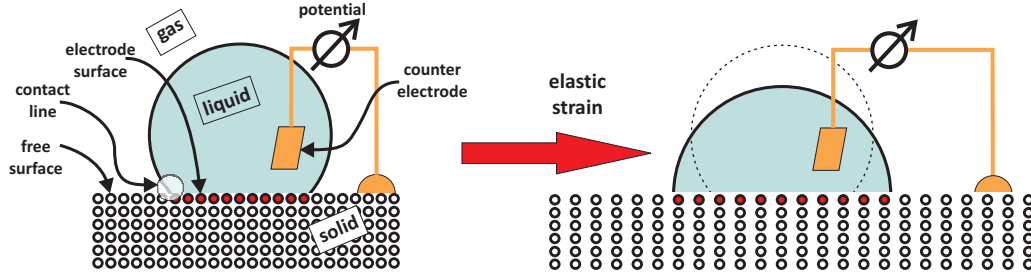
ELECTRODE SURFACE:

$e = 0$	elastic strain	$e = \varepsilon$
$N = N_0$	number of surface atoms	$N = N_0$
$A = A_0$	Lagrangian area	$A = A_0$
$\overline{A} = A_0$	physical area	$\overline{A} = (1+\varepsilon)\,A_0$
$r^{NN} = r_0^{\;NN}$	interatomic distance (in-plane)	$r^{NN} = (1+ \frac{1}{2}\,\varepsilon)\,r_0^{\;NN}$
$\gamma = \gamma_0$	surface tension	$\gamma = \gamma_0 + f\,\varepsilon$
$\delta G = 0$	variation in excess free energy	$\delta G = A_0\,\delta\gamma = f\,A_0\,\varepsilon$

Figure 2.8: Increase of the physical surface area, $\overline{A}$, of an electrode by the elastic strain, e, with relative amount ε, while keeping the electrode potential constant. The electrode surface is formed where a liquid droplet wets a solid metal. Circles represent atoms, red solid circles denoting electrode surface atoms in contact with the liquid. Elastic strain of the metal (right side of graphics) enhances $\overline{A}$ by increasing the in-plane interatomic spacing from r_0^{NN} to $r_0^{NN}(1 + \varepsilon/2)$, while leaving A and the number of surface atoms constant. The variation in excess Gibs free energy here scales with f, the surface stress, $\delta G = f A_0 \varepsilon$. Adapted from Ref. [70].

The process under consideration (right-hand side of Fig. 2.8) is an elastic strain, e, of the electrode in the tangent plane, with the strain magnitude $e = \varepsilon$. This might be brought about by mechanical force applied to the metal in study. The contact line is taken to remain stationary in the Lagrangian frame, in other words, the line is displaced along with the surface atoms. Here, the physical area is varied by the relative amount ε while the number of surface atoms as well as the Lagrangian area of the electrode remain a constant. The variation in G^{sl} is then entirely due to a change in the surface tension, $\delta G^{sl} = A_0 \delta \gamma^{sl}$. The variation in γ^{sl} will not generally vanish, since the strain changes the interatomic spacing between the metal atoms at the electrode surface, thereby modifying the state of the surface. In fact, experiment as well as ab initio computer simulation put the derivative, $f = \partial \gamma^{sl} / \partial e$, of the surface tension of solids with respect to the elastic strain e, at a similar numerical magnitude as the surface tension itself [72–75]. The quantity f is termed the surface stress. In terms of f, we have here

$$\delta G^{sl} = A_0 \delta \gamma^{sl} = A_0 \frac{\partial \gamma^{sl}}{\partial e} e = A_0 f^{sl} \varepsilon \,. \tag{2.28}$$

The relevant capillary parameter is here not the surface tension but rather its strain-derivative, the surface stress. Specifically, the mechanical equilibrium of compliant electrodes is governed by the surface stress and the excess free energy can depend on the strain variable.

2.2.5 Thermodynamic Maxwell relation for electrocapillarity

Consider a polarisable metal electrode in contact with electrolyte and impose a tangential strain on the surface, so that the contribution on surface free energy density, ψ, of the electrode can come from the strain and electrolyte. ψ can depend on the composition parameters through the superficial excess, Γ, of the species in the elctrolyte [71]. The Γ characterizes the adsorbate population and thereby links the charge density, q, *via* $\mathrm{d}q = \Sigma - zF\mathrm{d}\Gamma$ [32]. The Faraday constant is denoted by F, and z labels the valency of ion. To summarize above, the surface free energy density, ψ, depends, at the most, on tangential strain e and superficial charge density q, namely $\psi = \psi(e, q)$.

In continuum mechanics, one assumes that the body starts from an undeformed configuration that is mapped into its deformed configuration in Lagrange coordinates. Surface free energy density, ψ, as well as the superficial charge density, q, are defined as densities per area of the surface in its undeformed state. A suitable strain variable, e, for use with isotropic surfaces is the relative change in physical area, A, during the deformation:

$$e = \delta A / A. \tag{2.29}$$

The state function ψ is related to the surface tension, γ, by a Legendre transform: $\gamma(e, E) = \psi(e, q) - qE$, see details of the derivation in Ref. [51, 71]. In view of Eq. (2.28), the energy-conjugate variables to e and q defined in this way are the scalar surface stress, f, and the electrode potential, E. Thus, the total differential of ψ, at constant pressure condition, is then

$$\mathrm{d}\psi = f\mathrm{d}e + E\mathrm{d}q. \tag{2.30}$$

The parameter of interest, the potential-strain coefficient ς_E, is a second derivative of ψ, namely

$$\varsigma_E = \mathrm{d}E/\mathrm{d}e \,|_q . \tag{2.31}$$

At equilibrium, the Maxwell relation equates ς_E to another coefficient, the derivative of the surface stress with respect to the charge density. In other words, $\varsigma_E = \varsigma_f$ [41–43, 48, 71], where

$$\varsigma_f = \mathrm{d}f/\mathrm{d}q \,|_e . \tag{2.32}$$

In other words, the response of the electrode potential to elastic strain at constant charge density (ς_E) is numerically equal to the response of the surface stress to changes in the superficial charge density at constant strain condition (ς_f).

The electrode potential in electrolyte at *pzc* condition is closely related to electron work function of metal surface in vacuum. Therefore, ς_E also agrees with yet another fundamental parameter, the work function-strain response, in *ab initio* computation [37, 38, 40].

$$\varsigma_{zc} = \frac{\mathrm{d}E}{\mathrm{d}e} \,|_{q=0} = q_0^{-1} \frac{\mathrm{d}W}{\mathrm{d}e} \,|_{q=0}, \tag{2.33}$$

where q_0 is the elementary charge and W is the work function.

The electrocapillary coupling coefficient, ς, can be precisely determined by experiment and by numerical simulation. The experiemntal results of ς_E obtained in this thesis could be supported in comparison with the pubished data of ς_f and ς_{zc} by other techniques.

2.3   Hydrogen evolution reaction

2.3.1   Reaction steps

Electrocatalytic hydrogen evolution reaction (HER) on different electrode materials such as Pt [76–81] and Au [35, 82–85] has been studied extensively, since it is one of the most fundamental electrochemical reactions. Based on the previous reports [77–79, 83, 86–88], the possible reaction steps in HER could be summarized in acid solution circumstances as following.

1) Underpotential deposition of hydrogen:

$$H_{aq}^+ + e^- + M_s \rightleftharpoons MH_{ad,upd}, \tag{2.34}$$

where $MH_{ad,upd}$ is the adsorbed hydrogen ion through underpotential deposition (UPD) and M_s is the metal atom on the surface. The surface is modified by almost complete monolayer of strongly bound UPD species.

2) Overpotential deposition of hydrogen. It is also called *Volmer* or *discharge reaction* in Eq. 2.35:

$$H_{aq}^+ + e^- + M_s \rightleftharpoons MH_{ad,opd}. \tag{2.35}$$

The electro-adsorption of H_{upd} and H_{opd} occurs in two different potential ranges. It has been found that monoatomic hydrogen reaction (2.34) can be generated on platinum electrode at positive potentials to the thermodynamic equilibrium potential of HER, whearas overpotential deposition (OPD) of hydrogen operates near the equilibrium potential of HER.

It is thermodynamically not possible for UPD H to form H_2 since the M-H bond energy is higher than the 1/2 H_2 bond [87, 89, 90]. The more weakly bonded, overpotential deposition (OPD) of hydrogen can contribute as an adsorbed intermediate to the H_2 evolution [77, 87, 90, 91].

The adsorption of H_{upd} is characteristic of Pt group metals only, while the adsorption of H_{opd} takes place at all electrode materials at which H_2 can be electrolytically generated [92]. Thus, the step (2.34) is negligible for gold electrode.

3) Indirect absorption of hydrogen, *i.e.* diffusion of adsorbed hydrogen into electrode bulk:

$$MH_{ad} + M_b \rightleftharpoons MH_{ab} + M_s. \tag{2.36}$$

MH_{ab} represents absorbed hydrogen and M_b is the subsurface or bulk metal atoms.

4) Direct absorption of hydrogen:

$$H_{aq}^+ + e^- + M_b \rightleftharpoons MH_{ab}. \tag{2.37}$$
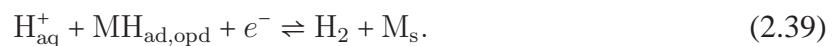
Since gold and platinum in study are the metals being not able to absorb hydrogen, reactions (2.36) and (2.37) are neglectable here.

5) *Tafel* or *combination reaction* in Eq. 2.38:

$$MH_{ad,opd} + MH_{ad,opd} \rightleftharpoons H_2 + 2M_s. \tag{2.38}$$

6) *Heyrowsky* or *ion+atom reaction* in Eq. 2.39:

$$H_{aq}^+ + MH_{ad,opd} + e^- \rightleftharpoons H_2 + M_s. \tag{2.39}$$

2.3.2   Reaction kinetics

As evident from the reactions, Volmer step occurs in series with other two steps, Heyrowsky step or Tafel step, since MH_{ad} is the product in only Volmer step for gold and platinum electrodes. Heyrowsky and Tafel steps are parallel to each other since H_2 is one of the product in both of the steps. Therefore, the HER path may be Volmer - Heyrowsky and Volmer - Tafel [78,93–95].

In serial steps, the step with the slowest rate controls the kinetics of the system. In parallel steps, the fastest step controls the kinetics. Since the Volmer step of HER is taken to be fast, the rate limiting step may be taken as the Heyrowsky reaction or Tafel reaction [76,82,96,97].

Classically, the trends for the mechanism are tested by analyzing current transients into the HER. For platinum, the Tafel and Heyrowsky steps seem equally important and Tafel step dominates at the low overpotential. Since hydrogen adsorption is not very strong for gold, typically a Volmer-Heyrowsky mechanism is relevant.

Since theis thesis will introduce the strain-dependent term into the reaction rate equations of HER, three reaction rates of Eqs. (2.35), (2.38) and (2.39) are stated here. The expressions for the reaction rates of each elementary step can be developed by applying the absolute reaction rate theory [93–95]. Assuming Langmuir adsorption isotherm [58,59,61], the reaction rate of the Volmer reaction is given by [93,94]

$$v_v = k_v \frac{1-\theta}{1-\theta_{eq}} \exp \frac{-\alpha_1 F\eta}{RT} - k_{-v} \frac{\theta}{\theta_{eq}} \exp \frac{(1-\alpha_1)F\eta}{RT}; \tag{2.40}$$

the reaction rate of the Heyrowsky reaction is given by [93,94]

$$v_h = k_h \frac{\theta}{\theta_{eq}} \exp \frac{-\alpha_2 F\eta}{RT} - k_{-h} \frac{1-\theta}{1-\theta_{eq}} \exp \frac{(1-\alpha_2)F\eta}{RT}; \tag{2.41}$$

and the reaction rate of the Tafel reaction is [93,94]

$$v_t = k_t \frac{\theta^2}{\theta_{eq}^2} - k_{-t} \frac{(1-\theta)^2}{(1-\theta_{eq})^2}, \tag{2.42}$$

where θ is the fractional surface coverage of adsorbed hydrogen, θ_{eq} is the hydrogen coverage at equilibrium potential, F is the Faraday constant, R is the gas constant, T is the absolute temperature and η is the net applied overpotential. α_1 and α_2 are symmetry factors for Volmer and Heyrowsky reactions, respectively. k_i is the rate constant of forward chemical reactions (where subscript $i = v$, h, t stand for Volmer, Heyrowsky and Tafel steps) and k_{-i} is the rate constant for backward reactions.

Chapter 3

Experimental procedure

The experimental setup of the dynamic electro-chemo-mechanical analysis is described in this chapter to detect and quantify the electrocapillary coupling parameters of interest. The setup imposes a cyclic strain on the electrode surface, removes the limitation of open circuit condition and then includes the potential control to investigate the potential-strain response, ς_E, as a function of the electrode potential. The experimental setup for measuring the current-strain response, is established for the first time to directly study the mechanical modulation catalysis as well. This chapter illustrates the process of sample preparation first.

3.1   Sample preparation

Two types of physical vapor deposition, evaporation and sputtering, were used to prepare the samples in this study[1]. The choice of polyimide film (Upilex-S) as the substrate of samples was due to its outstanding mechanical and chemical resistance properties[2] over a wide temperature range up to 400°C [98].

Since the gold, platinum and palladium metals have been studied widely in the experiments of measuring the electrocapillary parameters [14, 15, 43, 48, 100–103], the gold thin films were prepared by evaporation deposition to validate the measurement strategies for measuring the parameter of potential-strain response, $\varsigma_E(E)$, in Chapter 4. Taking one step further to the mechanical modulation of electrocatalysis, the gold and platinum metals prepared by the sputtering deposition were then chosen to investigate the impact of strain on the hydrogen evolution reaction in Chapter 5.

Here it lists some advantages and disadvantages of each deposition method:

i.) Evaporation deposition

---

[1]The evaporation method was available at the Institute of Nanotechnology (INT), of the Karlsruher Institut für Technologie (KIT). The sputtering method was preferred to use during studying at the Technische Universität Hamburg-Harburg for its good performance. That is why two deposition methods were used in this thesis.

[2]The high tensile strength of Upilex-S allows to apply the high elastic strain on the samples. Upilex-S is insoluble in all organic solvents, and is sufficiently resistant to inorganic acid solutions. The advantages of these chemical-resistance properties are that *i.*) it is easier to clean the substrate with organic solution prior to metal film deposition, and *ii.*) the substrate film is quite stable in acid solution environment during the DECMA experiments. Upilex-S features low water absorption and hygroscopic expansion. This property of higher hydrophobicity, comparing with the traditional Kapton polyimide [98, 99], makes the deposition metal film stronger adhesion to the substrate in the present experiments.

Advantages: higher purity due to the lower pressure, less residual stress after deposition.

Disadvantages: poor step coverage, difficult to form alloy, lower throughput due to low vacuum.

ii.) Sputtering deposition

Advantages: better step coverage, higher packing density, less radiation damage than e-beam evaporation, easier to deposit alloys.

Disadvantages: some plasma damages, sample including implanted argon.

3.1.1   Evaporation deposition

Thermal evaporation is the vaporization of a material by electron beam heating to a temperature such that the vapor pressure becomes appreciable and atoms or molecules are lost from the surface in a vacuum. The schematic diagram is shown in Fig. 3.1 a). The high vacuum allows vapor particles traveling directly to the substrate, where the particles condense back to the solid state.
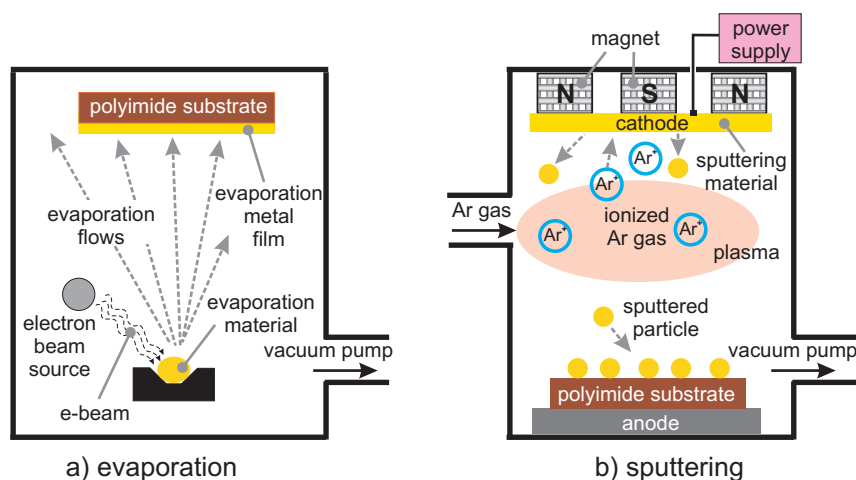
Figure 3.1: The schematic diagram of two types of physical vapor deposition for samples preparation: **a**) evaporation and **b**) sputtering. The polyimide films (upilex-S) were used as substrate.

In Chapter 4, 20 nm thin gold films were thermally evaporated through a shadow mask onto 125 μm thick Upilex-S polyimide substrates. Prior to the metal deposition, the substrates were rinsed with ethanol and ultrapure water, dried in nitrogen atmosphere, subjected to argon plasma etching for 5 minutes and then kept in 10^{-7} mbar vacuum for 12 hours. Then 1~2 nm titanium was deposited as an adhesion promoter, followed by vapor deposition of the Au electrode proper at a deposition rate of 0.02 nm s^{-1}. The deposited thickness of metal film was controlled by a quartz microbalance. Thickness standard deviation was about 5%.

Before the electrochemical experiments, the electrodes with deposited metal film were annealed at 250°C for one hour in a vacuum of 10^{-8} mbar and then cold down slowly to the room temperature.

These electrodes were fabricated using facilities available at the Institute of Nanotechnology (INT) of the Karlsruher Institut für Technologie (KIT) in the group of Prof. Dr. Schimmel.

3.1.2 Sputtering deposition

Sputtering deposition is a process where atoms are ejected from a solid target material due to bombardment of the target by energetic particles and then deposits onto a substrate. A schematic diagram is shown in Fig. 3.1 b). Magnets are employed in sputtering sources to utilize strong electric and magnetic fields to confine charged plasma particles close to the surface of the sputter target. Two types of sputtering are classified based on the ways of power supply as [104]:

i.) DC sputtering: Sputtering can be achieved by applying large direct current (DC) voltages to the target (cathode). A plasma discharge is established and the Ar ions (Ar$^+$) are attracted to the target. And then the Ar ions impact the target sputtering off target atoms. In the DC sputtering method the target must be electrically conductive, otherwise the target surface charges up with the collection of Ar ions and repel other Ar ions, halting the process.

ii.) RF sputtering: Radio Frequency (RF) sputtering allows the sputtering of targets that are electrical insulators (*e.g.* SiO$_2$). The target attracts Ar ions during one half of the cycle and electrons during the other half cycle. The electrons are more mobile and build up a negative charge, called *self bias*, that aids in attracting the Ar ions which does the sputtering. RF Sputtering can operate at lower Ar pressures, is easier to keep plasma going and fewer gas collisions.

The working electrodes (WE) were 50 nm thin gold films and 50 nm platinum films in Chapter 5, by the sputtering deposition onto the polyimide substrates. Prior to the metal deposition, the substrates were cleaned with the same processes as in the evaporation deposition, like rinsing with ethanol and ultrapure water, drying in argon atmosphere, subjecting to argon plasma etching. Then 3 ~ 5 nm thick titanium was deposited at 280 W sputtering power for 3 seconds as an adhesion promoter by DC sputtering, followed by RF sputtering of the Au (or Pt) electrode proper at 100 W power for 120 seconds in 7.9×10^{-3} mbar vacuum and 99.995% Ar gas flowing with the rate of 43 sccm (Standard Cubic Centimeters per Minute) in the chamber. Thickness standard deviation was about 10%.

The samples utilized in this thesis by the sputtering method were prepared using the facilities (Sputtering machine Z550) at the Institute of Micro-System Technology of the Technische Universität Hamburg-Harburg in the group of Prof. Dr. -Ing. Trieu.

3.1.3 Sample geometry
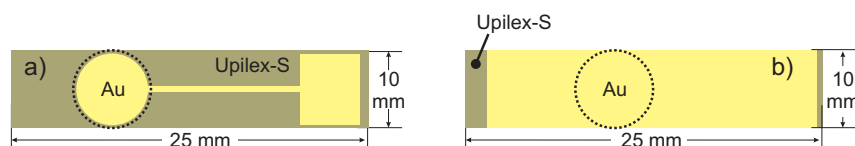
Figure 3.2: The schematic diagrams of samples geometry, Au metal thin films deposition on Upilex-S substrates: **a**) disc shape layer with a homemade mask; **b**) full layer covering on the top of the substrate. Yellow shadow shows the deposition metal layer. The dashed line represents the contact area between the metal and the electrolyte.

In the experiments of potential-strain response, constant charge density in referential coordinates was implemented by patterning the electrode so that it occupied only a part of the wetted

area of the polyimide film, see Fig. 3.2 a). This geometry warranted that the entire electrode surface was wetted at all times. In this way, the charge resided on the same referential area (same atoms) irrespective of the strain.

During the experiments of hydrogen evolution reaction in Chapter 5, the product of H_2 by the high reaction current, invading the side face of cohesion layers, may lead to the decohesion of the deposition metal layer from the polyimide substrate. A full deposition metal layer was thus adopted to avoid this delamination, as shown in Fig. 3.2 b). Since the amplitude of cyclic strain in this study is sufficiently small on the order of 10^{-4}, the constant wetted referential area is a good approximation. Moreover, the coupling coefficient for reactivity-strain strength is independent on the area by measuring the relative variation of the Faraday current in Chapter 5.

Overall, the geometrical area of the working electrodes were 0.78 ± 0.15 cm^2. Knowledge of the area is useful in the interest of comparing the capacitance magnitude and the current density in a cyclic voltammogram to that of published data. It is emphasized, however, that the area is never a parameter in the experimental determination of potential-strain response, ς, and reactivity-strain strength, λ.

3.2   Sample characterization

3.2.1   X-ray diffraction

The X-ray diffraction (XRD) was performed on the electrode specimens using reflection mode. Therefore, a Panalytical X'Pert $\theta - \theta$ diffractometer was used in Bragg-Brentano geometry with Ni-filtered Cu-K$_\alpha$ radiation and a position-sensitive solid-state detector. This technique is based on observing the scattered intensity of an X-ray beam hitting a sample as a function of incident and scattered angle.

3.2.2   Scanning electron microscopy

The scanning electron microscopes (SEM; LEO 1530) were operated at 15 kV for the surface topography of samples. The value of working distance (WD) was 6 mm between the surface of a specimen and the low portion of the lens.

3.2.3   Atomic force microscopy

Atomic Force Microscopy (AFM) technique, Multimode Nanoscope III (Veeco, Digital Instruments) in a tapping mode, was used to characterize the surface topography of electrodes with the lateral resolution in nanometer scale. The advantages of tapping mode are the elimination of a large part of permanent shearing forces and the causing of less damage to the sample surface, even with stiffer probes. The images were taken at a scan rate of 2 μm s^{-1} over scanned areas of 1 μm $\times$ 1 μm in 512×512 pixels.

3.3 Dynamic electro-chemo-mechanical analysis stage

3.3.1 Mechanical setup

Figure 3.3 illustrates the mechanical setup of the dynamic electro-chemo-mechanical analysis, for the dimensions see more detail in Ref. [53]. The working electrode was clamped between a fixed and a mobile grip, the latter being cyclically displaced by a piezo-actuator. Buckling of the electrode was prevented by a slight pretension, $\lesssim 1\%$ static tensile strain, which was determined by acquiring the imposed load on substrate through piezo-actuator. The thin metal film was strongly adhered to the substrate without crack even under this slight pretension. Typical displacement amplitudes were $10 \sim 20 \, \mu$m, yielding the amplitude of cyclic strain in the order of 10^{-4}. The entire mechanical and electrochemical equipments were enclosed in an O-ring sealed, high vacuum type stainless steel, which was repeatedly evacuated and purged with high purity (99.9999%) Ar gas and then sealed under Ar at atmospheric pressure during an experiment.
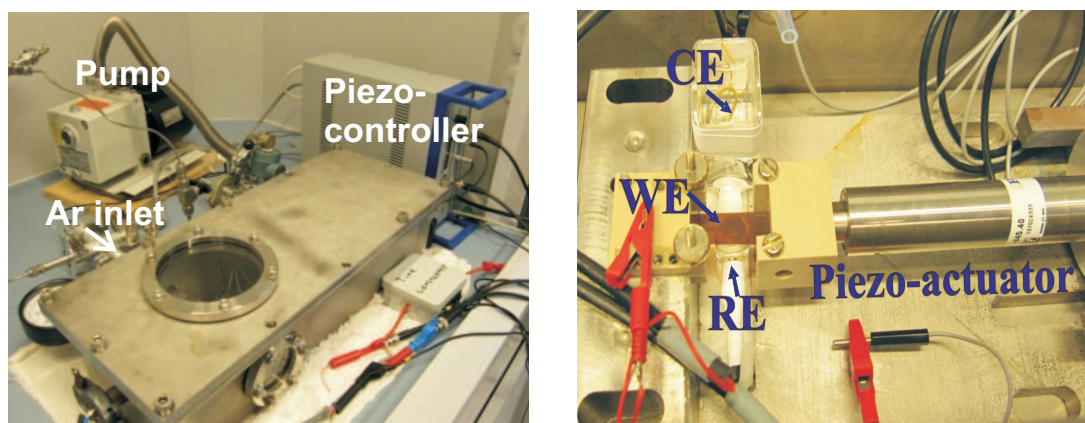
Figure 3.3: Photographs of the experimental setup. WE - working electrode, RE - reference electrode, CE - counter electrode. Cyclic strain was generated by the piezo-system and corresponding signal was recorded by means of an external lock-in amplifier.

3.3.2 Electrochemical system

The sample was mounted in a miniaturized mechanical testing stage, with metal side of the WE facing down and contacting from below by a standing meniscus. The glass electrochemical cell consisted of the main body and a counter electrode (CE) compartment, which was separated by a channel. A schematic view is show in Fig. 3.4. A gold (or platinum) wire was used as CE while the Au (or Pt) electrode played the role of WE in measurements. The reference electrode (RE), Ag/AgCl in 3.5 M KCl (World Precision Instruments), was separated from the main body of the electrochemical cell by a Luggin capillary ending about 2 mm from the sample surface. All potentials in this thesis were quoted *versus* the standard hydrogen electrode (SHE), which is positive by 197 mV compared to potentials measured *versus* Ag/AgCl in 3.5 M KCl [58].

The electrolytes used in all experiments were prepared from H_2SO_4 or $HClO_4$ (Suprapur, Merck) and ultrapure water (18.2 MΩ cm, Sartorius), and then deaerated with 99.9999% Ar for

1 hour. Prior to starting an experiment, all glassware was cleaned in pirani solution (5 volume parts of concentrated H_2SO_4 + 1 part of 30% H_2O_2) for 24 hours and then rinsed thoroughly with ultrapure water.
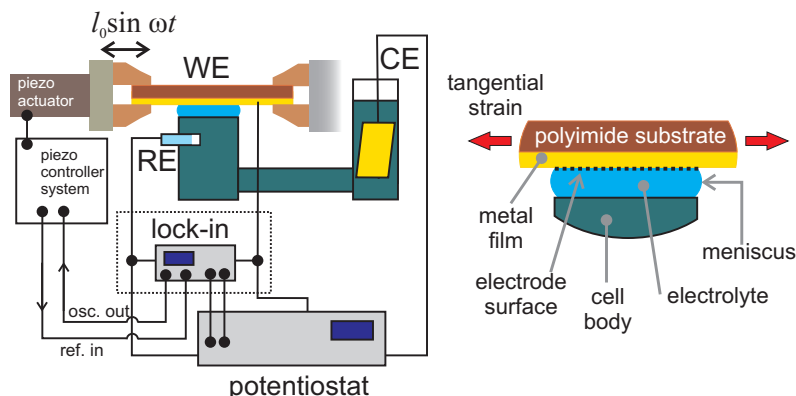

Figure 3.4: Schematic views of the experimental setup represent general setup (left-hand side) and blow-up of the electrode geometry (right-hand side). The electrochemical cell was made from glass and had separate compartments for the WE and the CE. The RE was placed close to the WE. The excitation signal from a lock-in amplifier was applied to piezo-controller system. Then the grip displacement, $l_0 \sin(\omega t)$, was given from the sensor in piezo-actuator and used as the reference signal in the amplifier. The amplifier output was the potential- or current-modulation by the electrode deformation. A potentiostat controlled the potential on the WE.

3.3.3   Measurement electronics

A schematic view of the connection in the experimental setup is also shown in Fig. 3.4. The separate functions of measurement electronics are listed here for the DECMA setup in detail.

Potentiostat

A potentiostat (PGSTAT 302N, Metrohm AUTOLAB) was used equipping with linear scan generator, staircase module for controlling the electrode potential and an impedance module for measuring the electrochemical impedance. In a traditional cyclic voltammetry experiment, the potential of the WE was scanned by the potentiostat in a fixed potential range with the two limit values, E_1 and E_2, at a constant rate, v, as an example shown in Fig. 3.5. The scanning starts from any potential between E_1 and E_2 to positive direction, and when it reaches E_2 the scan is reversed to E_1 till returning to the initial potential. The current response to this modulation of electrode potential is recorded and then plotted as a function of varied potential, giving rise to a so-called *cyclic voltammogram*.

   This thesis used two types of potential scan, linear scan and staircase sweep, as shown in Fig. 3.5. The linear scan is quite good to record the capacitive current. Thus, the experiments used the linear scan in Chapter 4 for measuring the coupling coefficient ς_E in the capacitive region. The staircase way is a particular format of cyclic voltammetry. In the staircase mode (Fig. 3.5 b), a potential step profile is applied to the electrochemical cell, and the current response

is measured at the end of each step. This allows to measure only the Faraday current, since the capacitive current, which appears at the beginning of step, has a much higher decay rate. Chapter 5 adopted this staircase mode to explore the strain-dependence of catalysis.
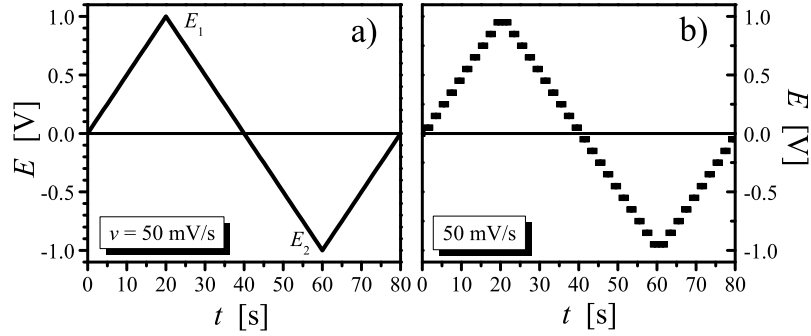
Figure 3.5: The electrode potential, E, changing *versus* time, t, in a typical cyclic voltammogram with different modes: **a**) linear scan; and **b**) staircase sweep. E_1 and E_2 denote the two limit values. Scan rate $v = 50$ mV s^{-1}.

Piezo-actuator system

In the DECMA setup, a cyclic elastic strain on the sample of interest was imposed by a piezo-actuator (PI-840 Physical Instruments), which incorporated a displacement sensor. A sinusoidal excitation signal of frequency ω from the function generator in a lock-in amplifier was applied to the piezo-controller system. This sinusoidal signal drove the grip displacement in the closed-loop control mode. The grip displacement, $l_0 \sin(\omega t)$, at any time was given from the sensor in the piezo-actuator (with the capacitive strain gauge) and was used as the reference signal in the lock-in amplifier.
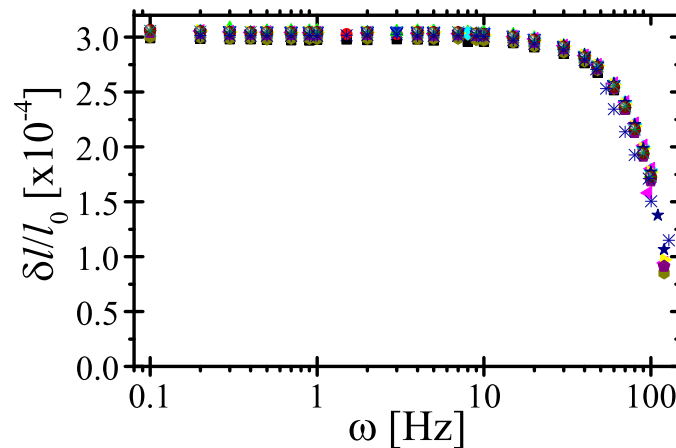
Figure 3.6: The actual amplitudes of axial strain are plotted as a function of frequency. Individual symbols refer to the different measurements of sample.

31

The inertia of the grip system, along with heating-up of the piezo-actuator during fast strain cycles, limits the accessible frequency range to $\omega \lesssim 100$ Hz[1]. The amplitude of the elastic strain applied to the sample is shown in Fig. 3.6 as a function of frequency. The axial strain is defined here as $\delta l/l_0$ with l_0 the initial sample length. The actual axial strain decreases at higher ω due to the heat generation in dynamic operation, which is a restriction of the piezo-system.

This thesis utilized the strain frequencies of 20 Hz and 70 Hz in measurements, below 100 Hz, due to the precise and stable performance of the piezo-actuator.

Lock-in amplifier

The cyclic variation of potential or current in response to the strain cycles was detected by means of a lock-in amplifier (SR 7270 Signal Recovery). The main function of the lock-in amplifier was to separate the DC potential (or current) and the variation of potential (or current) that induced by the cyclic strain.

The lock-in amplifier requires a signal with frequency, ω, or with period, T, as its reference signal. The present DECMA setup puts the dynamic signal of grip displacement, $l_0 \sin(\omega t)$, from the displacement sensor of the piezo-actuator as the reference signal. For a strain-induced signal, $S(t)$, the lock-in amplifier output for the in-phase ('real part') and out-of-phase ('imaginary part') amplitudes relative to the strain signal is

$$\hat{s}(t) = \frac{\sqrt{2}}{T} \int_{t-T}^{t} \sin(\omega\tau + \phi)S(\tau)d\tau \tag{3.1}$$

with $\phi = 0$ and $\pi/2$ for the real and imaginary part, respectively. Since the strain is modulated using sine function, the lock-in outputs need to be multiplied by $\sqrt{2}$, as shown in Eq. (3.1), in order to obtain the amplitudes of potential- and current- modulation, $\hat{E}$, $\hat{I}$. Both real and imaginary parts of output signals were recorded then conjugate to the electrode potential during *in situ* cyclic voltammetry.

3.3.4   The sign of lock-in amplifier

The signal input of the amplifier was set for differential voltage mode operation (A-B). This mode measured the difference in voltage between the port A and port B, shown in Fig. 3.7. The followed subsections describe the meaning of the sign of lock-in amplifier output which represents the amplitude of strain modulated potential or current.

Potential-strain response

In the potential-strain response measurements, port A of the lock-in amplifier was connected to the working electrode while port B was connected to the reference electrode, as shown in Fig. 3.7 a). The in-phase ('real part') amplitude of the amplifier output was the strain-induced potential, $\hat{E} = V_A - V_B$, where V_A and V_B denote the voltage on the port A and on port B of amplifier, respectively.

---

[1]The heat generation, or power loss, in piezo actuator in dynamic operation is a function of operating power and frequency. *cf.* Ref. [105].
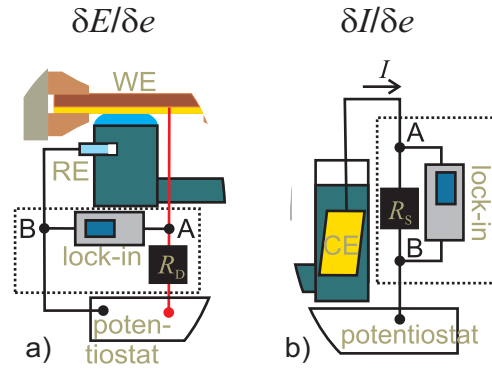
Figure 3.7: The placement and connection of a lock-in amplifier for measuring **a**) potential-strain response and **b**) current-strain response, respectively. Symbols R_D and R_s denote the resistances. Note that 'A' and 'B' are the two ports of the lock-in amplifier.

Positive value of $\hat{E}$ means that the tensile strain shifts the potential more positive, namely the parameter $\varsigma_E > 0$. During an electrosorption process, the electrode potential reflects the adsorption enthalpy, namely $E = -\Delta h / zF$ with the meaning of E the electrode potential, Δh the change of adsorption enthalpy, z the electron number and F the Faraday constant. Therefore, the positive value of ς_E implies that the tensile strain can decrease the adsorption enthalpy of the electrode ($z > 0$), thereby enhancing the reactivity of the electrode.

Current-strain response

In order to get the strain-induced current amplitude, a small value resistance, R_s, was in series to the counter electrode, as shown in Fig. 3.7 b). The value of current variation, $\hat{I}$, then converted to the difference in voltage between ports of A and B, namely $\hat{I} = (V_A - V_B)/R_s$. Thus, the sign of strain-induced variation relates to the difference of voltages ($V_A - V_B$). This thesis adopts the current direction as the same definition in the potentiostat, in which the positive current (anodic current) flows from the CE in the electrochemical cell to the potentiostat, or from port A to port B, as shown in Fig. 3.7 b).

The positive output value of the lock-in amplifier, $\hat{I}$, means that the tensile strain induces more anodic current for an electrochemical reaction. The tensile strain can thus enhance the electrode reactivity by producing more reaction current while the DC reaction current is an anodic current as well.

3.3.5   Amplitude of area strain

The grip displacement, δl, was measured by a factory-calibrated displacement sensor integrated into the piezo-actuator system. The calibration factor, 6.00 ± 0.2 μm V^{-1}, was also confirmed using a mechanical gauge.

Hooke's law, along with the solids for transverse elastic contraction, implies that the total relative change in surface area - which is the state variable in the present theoretical framework

- can be calculated using following expression:

$$\hat{e} = (1 - \nu)\frac{\delta l}{l_0}, \tag{3.2}$$

where ν denotes the Poisson ratio. In the data analysis, the value $\nu = 0.35$ was used for polyimide [98, 106]. Finally, the calculated amplitude of the area strain on the Upilex substrate was $\sim 2 \pm 0.2 \times 10^{-4}$ at the frequency of 20 Hz, and $1.6 \pm 0.2 \times 10^{-4}$ at the frequency of 70 Hz, in the experiments of this thesis.

It is essential that the metal film deforms elastically and coherently with the substrate. This condition was confirmed in $E(e)$ during slow cycles [43]. Note also that the strain amplitude in the experiment never exceeded 10^{-3}. The *in situ* magnetization and x-ray diffraction experiments under load have established that the substrate deformation is precisely transferred to the electrode up to the much larger strain amplitudes of 1% [107, 108]. This is further supported by the signal reversibility and reproducibility in the present DECMA studies in Chapter 4 and by the precise agreement of the electrocapillary coupling coefficients determined there with independent results from surface stress measurements [48, 109] and DFT [38].

Chapter 4

Dynamic electro-chemo-mechanical analysis

This chapter detects and quantifies the electrocapillary coupling parameter of potential-strain response, ς_E, during a cyclic voltammetry. Firstly, the terminology is briefly established in a theory section for discussing the present experiments of measuring the coupling parameter. The measurement strategies, dynamic electro-chemo-mechanical analysis (DECMA), are then verified by three independent experiments based on the theoretical analysis. The DECMA method is applied generally to investigate the behaviors of ς_E at different electrochemical conditions (*e.g.*, polarisable/nonpolarisable electrodes, different concentration of electrolytes, different nobel metals as well as different electrosorption processes).

4.1 Theory section

The present chapter starts out with introducing cyclic strain into a phenomenological description of an electrode/electrolyte system. The phenomenological description of the coupling between cyclic strain and electrode potential/current rests on the theory below of the electrocapillarity of an electrode surface at equilibrium. The phenomenological approach identifies the relevant state variables yielding equilibrium condition.

4.1.1 Potential-strain response at equilibrium condition

Consider an experiment where the area strain, e, is varied cyclically with time, t:

$$e = \hat{e} \sin(\omega t) \tag{4.1}$$

with frequency ω and amplitude $\hat{e}$. Consider further that the electrode is ideally polarisable (no Faraday processes) and that open circuit conditions apply. The potential will then vary, in phase with the strain, as

$$E = \hat{E} \sin(\omega t) = \varsigma_E \hat{e} \sin(\omega t) \tag{4.2}$$

with amplitude $\hat{E}$. Therefore, the coupling parameter ς_E can be obtained as the ratio of the amplitudes of E and e, that is, $\varsigma_E = \hat{E}/\hat{e}$ (as the definition of ς_E in Chapter 2).

As will become apparent below for an alternative experimental method of measuring ς_E, it is also of interest to introduce a measure for the current-strain response. Let us also consider an experiment where e is cycled at constant potential and assume small strain and a linear charge-strain relation. Thus the charge density will vary according to

$$\delta q = \mathrm{d}q/\mathrm{d}e|_E \delta e. \tag{4.3}$$

This variation may be related to ς_E by means of the identity $\mathrm{d}X/\mathrm{d}Y|_Z = -\mathrm{d}X/\mathrm{d}Z|_Y \mathrm{d}Z/\mathrm{d}Y|_X$ [110], for state variables X, Y, Z. In the present charge-strain relation, this implies

$$\mathrm{d}q/\mathrm{d}e|_E = -\mathrm{d}q/\mathrm{d}E|_e \mathrm{d}E/\mathrm{d}e|_q. \tag{4.4}$$

Since $\mathrm{d}q/\mathrm{d}E|_e$ represents the capacity, c, we have

$$\mathrm{d}q/\mathrm{d}e|_E = -\varsigma_E c. \tag{4.5}$$

Therefore, the charge density at equilibrium varies as

$$q = -\varsigma_E c \hat{e} \sin(\omega t), \tag{4.6}$$

which implies that the net current density, j, varies, out of phase with the strain, as

$$j = \mathrm{d}q/\mathrm{d}t = \hat{j} \cos(\omega t) \tag{4.7}$$

with

$$\hat{j} = -\varsigma_E c \omega \hat{e}, \tag{4.8}$$

or equivalently

$$I = \mathrm{d}Q/\mathrm{d}t = \hat{I} \cos(\omega t) \tag{4.9}$$

with

$$\hat{I} = -\varsigma_E C \omega \hat{e}, \tag{4.10}$$

where I, Q and C represent net current, net charge and net capacitance of the electrode, which are accessible in the experiment even when the electrode area is not known. Let us define a notation of current-strain response, Λ, at constant potential condition as

$$\Lambda = \mathrm{d}I/\mathrm{d}e \,|_E = \hat{I}/\hat{e}. \tag{4.11}$$

Then a simple relation, $\Lambda = -C\omega\varsigma_E$, shows that the current-strain response, Λ, takes a opposite sign of parameter ς_E at equilibrium near the potential of zero charge (*pzc*).

4.1.2   Potential-strain response at finite frequency

In order to probe the potential-strain response in an experiment exploiting Eq. (4.2), it is required that Faradaic currents are sufficiently small so that $q =$ constant is a good approximation. This can typically be enforced by performing the experiment at a sufficiently large strain frequency [43, 44]. Such high-frequency strain cycles can lead to a limited equilibration, for instance due to the finite transport rate in the electrolyte or due to slow adsorption rates. This leads to phase shifts in the potential- and /or current- response that require discussion.

Let us again consider a cyclic strain, $\hat{e}\sin(\omega t)$, as the same in Eq. (4.1). When the potential-strain response is linear, the potential variation at constant q and finite frequency will be

$$E = \varsigma_E \hat{e} \sin(\omega t - \phi), \tag{4.12}$$

with ς_E here being an apparent potential-strain response parameter and ϕ a phase shift relative to the cyclic strain. It is important to note the analogy to conventional electrochemical impedance spectroscopy (EIS). As in a conventional EIS experiment, potential variation and current variation are interrelated by the complex impedance, $\mathbf{Z} = Z_{re} + i Z_{im}$, where i is imaginary unit. The phase angle, φ, of this complex impedance is

$$\tan \varphi = Z_{im}/Z_{re}. \tag{4.13}$$

The cyclic potential variation in a EIS experiment is imposed by the potentiostat, and the impedance $\mathbf{Z}$ describes the response of the cyclic current. Therefore, the strain-induced variation of cyclic potential, in the dynamic electro-chemo-mechanical analysis, gives rise to a responding cyclic current. This current variation signal is again phase-shifted relative to the potential variation by φ due to the electrochemical impedance. Since the amplitude of the potential variation is here given by $\hat{E} = \varsigma_E \hat{e}$, a combination of the standard definition of the impedance [58] and Eq. (4.10) implies that the current signal is then

$$I = \hat{I}\cos(\omega t - \phi - \varphi) \tag{4.14}$$

with

$$\hat{I} = -\varsigma_E \hat{e}/|\mathbf{Z}|. \tag{4.15}$$

The current-response is again governed by $\mathbf{Z}$. This implies that the function $\mathbf{Z}(\omega)$ can be measured by conventional impedance spectroscopy. Thus, the parameter ς_E can be measured alternatively by equation:

$$\varsigma_E = -\hat{I}|\mathbf{Z}|/\hat{e} = -\Lambda|\mathbf{Z}|. \tag{4.16}$$

In the part of current-strain response measurements in this chapter, the relation of Eq. (4.16) was exploited for measuring the variation of strain-induced current $\hat{I}$ in a DECMA experiment and combining the signal with the $\mathbf{Z}$ value as determined by an impedance spectroscopy experiment performed under nominally identical conditions, in order to determine ς_E in the potential interval accessible to cyclic voltammetry. The experimental processes of interest are limited to surfaces with e near zero, and therefore ignoring the strain-dependence of ς_E here.

The subsequent sections display the description and validation of the measurement strategies in detail. The characterization of samples is first discussed.

4.2   Samples and characterization

The working electrodes (WE) were 20 nm thin gold films by evaporation deposition with the thermally annealled treatment. The scanning electron micrograph of gold electrode surface in Fig. 4.1 a) shows an equilibrated grain structure with polygonal crystallites several hundred nm in size. This is also confirmed by the atomic force microscopy (AFM) image, shown in Fig. 4.1 b), which displays the planar facets of 100 ~ 200 nm in size. The AFM images were taken

at a scan rate of 2 μm s^{-1} over randomly selected areas of electrode surfaces showing highly reproducible results. The root-mean-square height variation of the electrode surface was ~ 6 ± 2 nm. Moreover, the roughness factor, defined as the ratio between the real and projected surface area, was estimated at ~ 1.04 ± 0.02 by the software (v700; NanoScope). All observations imply that the surfaces of the gold electrode were quite smooth in the present study.
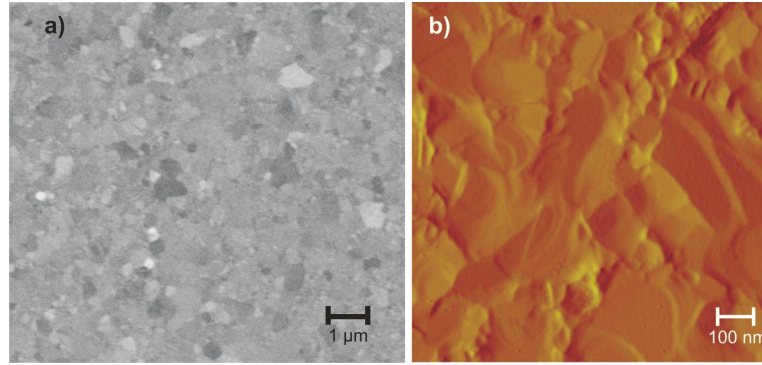
Figure 4.1: Electrode surface topology of Au electrodes with thermally annealing treatment. **a)** Scanning electron micrograph. **b)** Atomic force microscopy image of 1 μm × 1 μm area.

Figure 4.2 shows the crystallographic orientation of the as-prepared and annealed gold films by X-ray diffraction (XRD) measurement. The only reflection, appearing in the θ-θ X-ray scans, corresponds to the (111) peak, and then indicates a strongly (111)-textured surface. The intensity of the (111) peak of the annealed sample in the θ-θ scans is considerably larger. The full width of the rocking curve, inserted graph in Fig. 4.2, at half maximum (FWHM) is 11.47° for the as-prepared electrode, whereas the value is 6.69° for the annealed sample. The XRD results imply that the gold electrode has better a preferentially 111-oriented texture after thermal annealing, probably due to thermal stress/strain relaxation.

Figure 4.2: X-ray diffraction characterization of Au electrodes. Main graph: intensity *versus* scattering angle 2θ. Inserted graph: Rocking curve of intensity *versus* inclination angle for the (111) reflection. The black curve is for the annealed Au electrode; the red one is for the as-prepared sample.

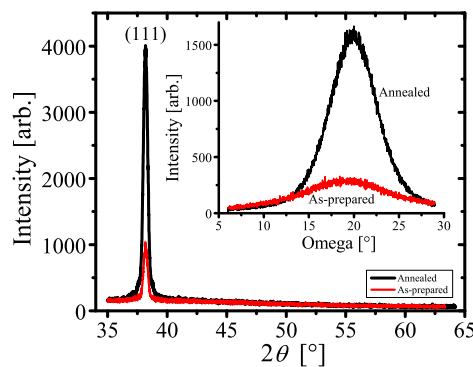Overview cyclic voltammograms (CVs) in 10 mM $HClO_4$ in Fig. 4.3 are consistent with clean gold surface [43, 111]. Most CVs in this chapter were at an unusually small scan rate of 1 mV s^{-1} with linear potential scans module, so that even small Faraday currents showed up prominently. It is emphasized that all results are compatible with clean electrolytes at low oxygen concentration, in spite of the noticeable Faraday current.
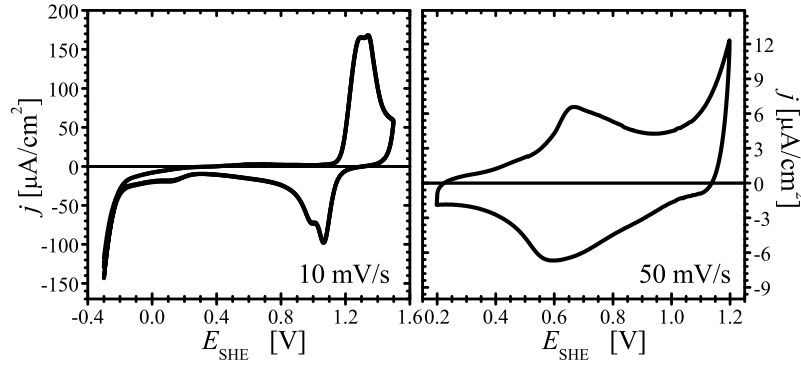

Figure 4.3: Cyclic voltammograms of current density, j, *versus* electrode potential, E, of the annealed gold electrode in 10 mM $HClO_4$ and two different potential windows. Scan rates are indicated in the figures.

4.3 Measurement strategies and validation

The task here is to separate the cyclic strain-induced potential variation and potential cycle during a cyclic voltammetry. Typical CVs used linear potential scans with a scan rate of 1 mV s^{-1}, a potential interval of 1 V, and a total cycle time of around 30 minutes or 0.6 mHz. Strain cycles with frequencies, ω, of up to 100 Hz - up to 5 orders of magnitude faster than the potential cycle - were applied simultaneously. The amplitude of the strain-induced cyclic potential variation was in the order of 0.1 ~ 1 mV, much smaller than the potential range of the voltammogram. As detailed in Chapter 3, a lock-in amplifier was used to separate such two signals. Implementation of this scheme imposed two challenges: first, the potential variations on the two different time scales and with two quite different amplitudes need to be separated. Second, a distinguishing feature of cyclic voltammetry in potentiostatic mode is that the potentiostat controls the electrode potential at each time to the respective setpoint. Thereby, the potentiostat compensates and suppresses the effect that is to be measured.

Three different and independent strategies are explored now to take account of these issues for measuring the parameter ς_E.

4.3.1 Current-strain response in potentiostatic mode

In this part of measurements, a conventional cyclic voltammogram is recorded while the electrode is cyclically strained. Even at $\omega = 100$ Hz, the strain cycles are sufficiently slow for the potentiostat to accurately compensate the strain-induced potential variation. This entails a cyclic

modulation of the current, which can either be directly recorded as a part of the voltammogram or be analyzed in terms of amplitude and phase by the lock-in amplifier. The second alternative was preferred in the present experiments, since the first requires a high sampling rate for the current and leads to prohibitively large data sets.

The potential-strain coefficient can be determined from the current amplitude according to Eq. (4.16), provided that the impedance is also known. Moreover, the sign of the coefficient ς_E is opposite to the modulation current. The ac-impedance measurements have therefore simultaneously performed and under identical conditions as the experiments with cyclic strain.

Figure 4.4 a) illustrates the experimental configuration for the current-strain response strategy. A shunt resistance of known magnitude, $R_S = 46\ \Omega$, was inserted between the potentiostat and the counter electrode, and the current amplitude $\hat{I}$ was determined from the amplitude of the potential drop over R_S. By means of illustration a constant potential has been imposed and then recording the time-dependence of strain, current, and electrode potential by an oscilloscope, and Fig. 4.4 b) shows the results. It is readily seen that E is held constant, in spite of the cyclic strain. It is also seen that the current variation is excellently resolved, in spite of the small strain amplitude. Phase shift of the current variation is observed relative to the strain signal due to the complex impedance, consistently with Eq. (4.14).

Figure 4.4: Measurement strategy of current-strain response in potentiostatic mode. Part **a)** is a schematics of the electronics setup, showing working, counter and reference electrodes (WE, CE and RE), potentiostat as well as the shunt resistance ,R_S. Part **b)** shows oscilloscope traces of the relevant signals in the time (t) domain. Axis labeled E, I and e refers to variations in electrode potential, electrode current and elastic strain, respectively.

4.3.2 Potential-strain response in potentiostatic mode

Here, the potential-strain response experiment is modified so that ς_E can be measured directly, without the need of separate current response and capacitance data. To this end, a delay resistance, R_D, is connected in series with the working electrode (shown in Fig. 4.5 a) as the function of low pass filter, ensuring that the strain cycles are approximately at constant charge. This resistance adds to the uncompensated solution resistance, R_U, which determines the potential drop between the RE and WE [112]. The result is an increase in the time constant for the potential control at the WE, preventing the potentiostat from compensating the potential varia-

tion due to the cyclic straining. As a consequence, the strain-induced potential variation can be measured by a lock-in amplifier connected between the WE and RE in potentiostatic mode.

Figure 4.5 b) exemplifies the results for $e(t)$, $I(t)$, and $E(t)$ at an arbitrary chosen potential and confirms the suppression of cyclic current. This verifies that conditions of near constant charge have been achieved, as required by the definition of ς_E. At the same time, the potential acquires an oscillation caused by cyclic strain of an electrode. A comparison of Fig. 4.4 b) and Fig. 4.5 b) illustrates the difference between these two measurement strategies of this and the previous sections, notably the switch between constant potential and constant charge conditions.
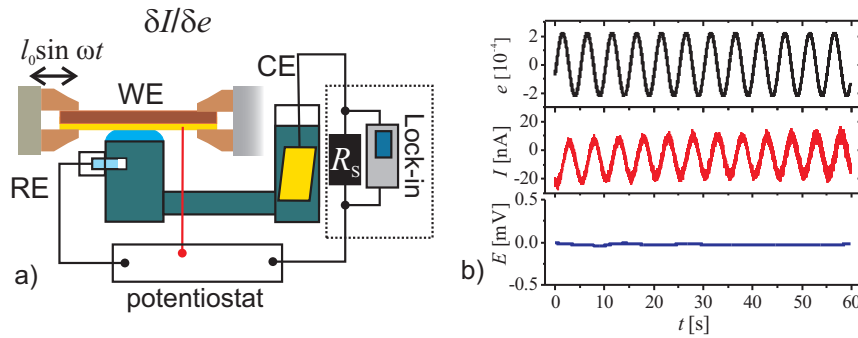

Figure 4.5: Measurement strategy of potential-strain response in potentiostatic mode. Part **a)** is the schematics of the electronics setup. Part **b)** shows oscilloscope traces of the relevant signals in the time (t) domain.

Correction of electrode potential
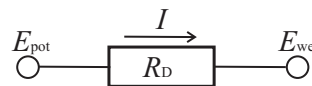
Figure 4.6: Simplified electrical circuit for measuring ς_E in potentiostatic mode. E_{pot} and E_{we} are the potential value at each port of the delay resistance R_D, respectively. The arrow indicates the direction of current.

An external resistance R_D is connected in series with the WE, the different potential values thereby display at two ports of R_D. The simplified circuit is shown in Fig. 4.6. The relation can be written as [113]:

$$E_{we} = E_{pot} - I R_D, \tag{4.17}$$

where E_{pot} is the value of electrode potential from the potentiostat, E_{we} is the actual potential on the WE and I is the net current. As will appear below, the experimental results show a comparison of the graphs of ς_E as the functions of E_{we} as well as E_{pot} in capacitive process and electrosorption region.

4.3.3   Potential-strain response in galvanostatic mode

In galvanostatic mode, the current is controlled rather than the potential. For small current values and fast mechanical cycling, each cycle represents a process at constant charge. Here, the potential-strain response can be measured directly, without the need for the delay resistance, R_D. The drawback is the lack of control over the potential scan rate. This method is only briefly touched, which provides an additional verification of procedures.

The lock-in amplifier was connected as the same as shown in Fig. 4.5 a), but the resistance R_D was removed (shown in Fig. 4.7 a)). Figure 4.7 b) illustrates a galvanostatic cycle. The current limits were between -3 μA and 3 μA with a current sweep rate of 0.1 μA s^{-1} and the corresponding potential value was observed in the range of 0 V ~ 0.9 V.
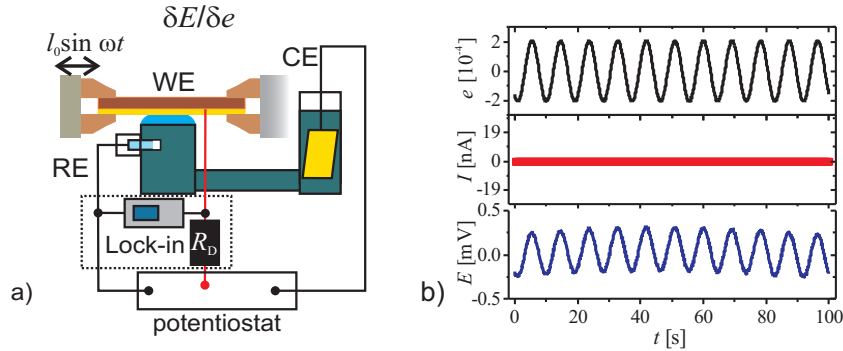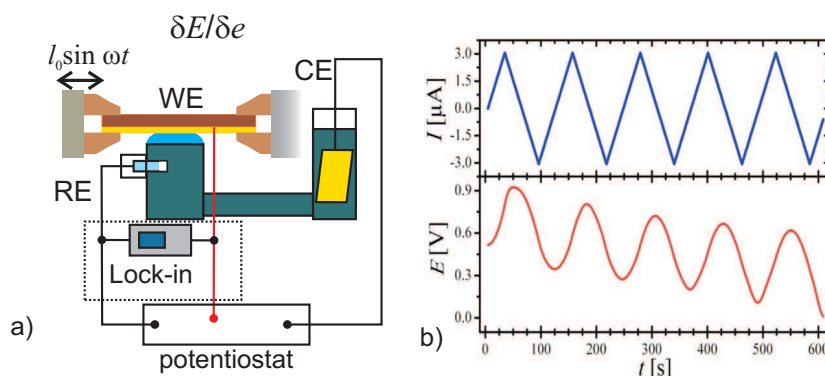

Figure 4.7: Measurement strategy of potential-strain response in galvanostatic mode. Part **a)** is the schematics of the electronics setup. Part **b)** shows the galvanostatic cycles by imposing the current and recording the corresponding potential variation.

4.3.4   Experimental results of three strategies

The section here exhibits the obtained quantitatively consistent results in study. Unless otherwise stated, the electrolyte was 10 mM $HClO_4$, and the measurements used a strain frequency of 20 Hz with a strain amplitude of $\hat{e} = 2 \pm 0.2 \times 10^{-4}$.

Current-strain response in potentiostatic mode

As mentioned above, in order to determine ς_E the amplitude of strain-induced current $\hat{I}$ was first measured in a DECMA experiment, and then combined with the impedance value **Z** as determined by an impedance spectroscopy experiment.

Figure 4.8 summarizes the results of the present strategy, starting out with the voltammogram and the apparent capacitance values. Both graphs show a capacitance maximum at $E \approx$ 650 mV *vs* SHE. Figure 4.8 c) shows the current-strain response, Λ, which is defined as the amplitude, $\hat{I}$, of the current modulation normalized to the strain amplitude, $\hat{e}$. The graph appears similar to the capacitance curve, but a closer look reveals that the maximum of Λ is at the potential 590 mV *vs* SHE, 60 mV lower than the capacitance maximum. The similar deviation in the potentials of the respective maxima was found in all experiments.
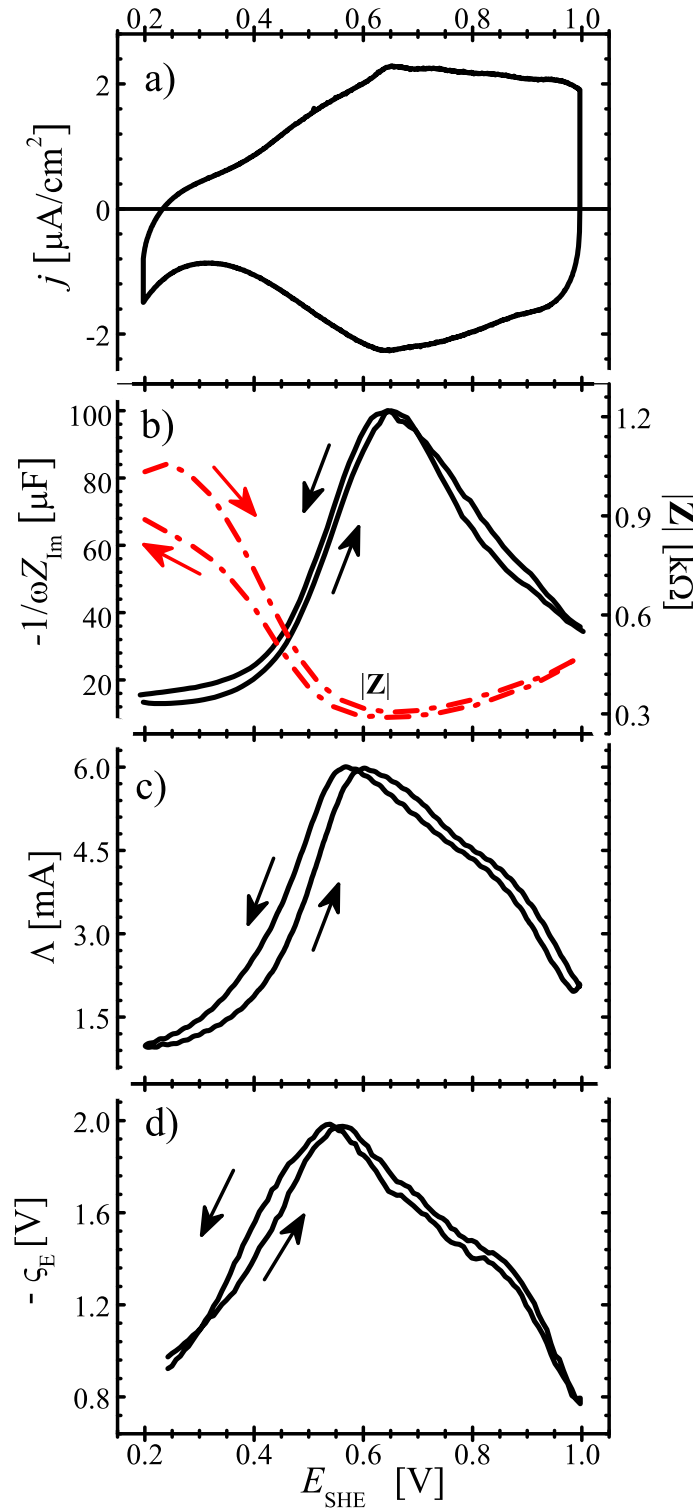
Figure 4.8: DECMA-data based on current-strain response under potentiostatic control. **a)** A *in situ* conventional cyclic voltammogram. **b)** Apparent differential capacitance, $-1/(\omega Z_{Im})$. Also plotted (right ordinate) is the magnitude, $|\mathbf{Z}|$, of the impedance (red dashed line). **c)** Magnitude of current-strain response, $\Lambda = \hat{I}/\hat{e}$. **d)** Potential-strain response computed via Eq. (4.16). Electrolyte: 10 mM $HClO_4$, potential sweep rate: 10 mV s^{-1}, cyclic strain frequency: 20 Hz.

By means of Eq. (4.16) along with $|\mathbf{Z}|$ (Fig. 4.8 b), ς_E can be determined from the current modulation and the impedance magnitude. Since the current modulation graph exhibits a slight hysteresis, the impedance data were measured during the positive as well as negative going potential scans and the respective branches used with Eq. (4.16). The result, Fig. 4.8 d), shows ς_E negative valued in the entire potential range. For ease of comparison with the impedance and current modulation data, the negative of ς_E is plotted as the ordinate. Similar to the apparent differential capacitance and current-strain response, the graph of $-\varsigma_E$ also exhibits a maximum peak. This feature is shifted to negative E relative to the peaks in capacitance curve and, though to a much lesser amount in current-strain response.

Potential-strain response in potentiostatic mode

By gradually increasing R_D, it is found that the current oscillation associated with the cyclic strain became negligible (*cf.* Fig. 4.5 b) at $R_D \approx 50$ kΩ. For a typical electrode capacitance of $C = 100$ μF (compare Fig. 4.8 b) this yields time constants ($\tau = RC$) of around 5 s, much longer than the cycle time of the mechanical strain but much shorter than the time to complete a sufficiently slow voltammogram. Electrochemical impedance spectroscopy suggested a solution resistance, R_U, of 350 Ω in these experiments. Even though $R_D \gg R_U$, cyclic voltammograms measured with and without the resistance R_D (Fig. 4.9 a) exhibit only minor differences at the small scan rates in question.
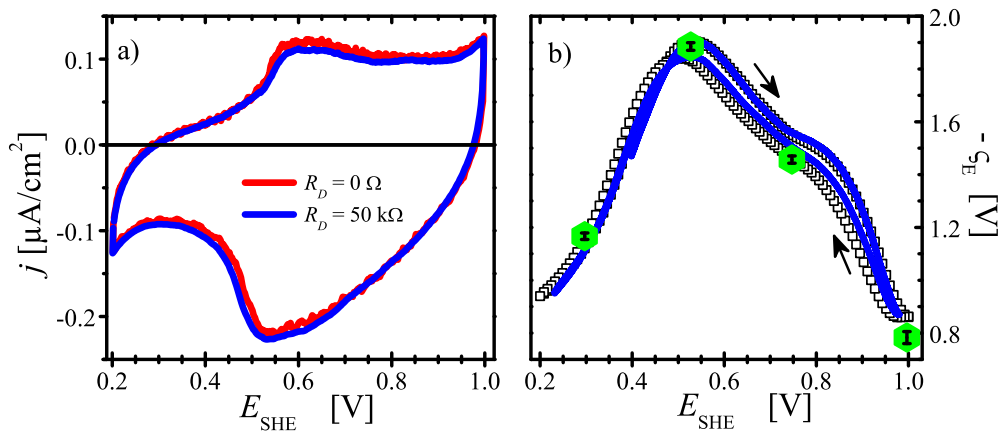
Figure 4.9: Results of DECMA based on the potential-strain response under potentiostatic control in 10 mM $HClO_4$. Scan rate: 1 mV s^{-1}. **a)** Cyclic voltammograms made without (red solid curve) and with (blue solid line) delay resistance $R_D = 50$ kΩ. **b)** Potential-strain response using $R_D = 50$ kΩ: the parameter $-\varsigma_E$ as a function of the experimental potential from the potentiostat (black dot curve with symbol □); blue solid line is plotted a function of the corrected potential on the WE via Eq. (4.17); the data of chrono-amperometry are here measured at potential setpoints of 0.3 V, 0.53 V, 0.75 V and 1 V (the green dots) with error bars (in black color).

Figure 4.9 b) shows the result of ς_E obtained from the present strategy with and without the potential correction of the WE via Eq. (4.17). A combination of Eq. (4.17) and Fig. 4.9 b) illustrates the value of E_{we} is approximate to E_{pot} in capacitive regime, since current I is quite

small in the case of slow scan rate. The agreement with the results of Fig. 4.8 d) is apparent in Fig. 4.9 b) (the blue solid line). The slightly hysteresis on forward and backward directions found here may be understood as the consequence of anion adsorption.

The chrono-amperometry measurement[1], at each potential setpoint (0.3 V, 0.53 V, 0.75 V and 1.0 V) during 600 seconds with an interval time of 5 s, was used to ensure the accuracy of ς_E measured in potentiostatic mode. The error bar of measurement is less than 3 % and the agreement of experimental data proofs the explored approach of measuring ς_E in potentiostatic mode.

4.3.4.1 Potential-strain response in galvanostatic mode

This experiment was executed between the current limits -1 μA and 1 μA with a current sweep rate of 10 nA s^{-1} and with cyclic strain applied. The corresponding potential is in the range of 0.2 V ~ 1 V. The magnitude of potential variation would be obtained by the lock-in amplifier when imposing the strain excitation signal. Figure 4.10 shows ς_E measured in the present galvanostatic mode. The result exhibits the direct observation of ς_E behaviors to proof those two experimental approaches above.
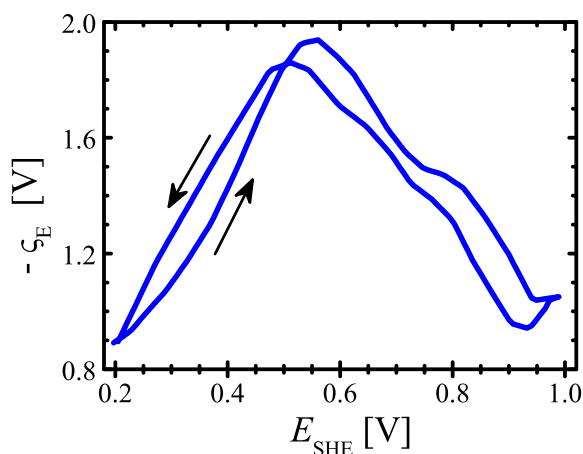
Figure 4.10: Potential-strain response, -ς_E, *versus* potential, E, measured in galvanostatic mode. Electrolyte is 10 mM $HClO_4$.

4.3.5 Discussion

Figure 4.11 summarizes the results for $\varsigma_E(E)$ from the three independent approaches. It is seen that the graphs agree, within narrow margins, throughout the entire potential range. It indicates that these experiments provide valid data for the quantity of interest, the response of the electrode potential to strain at constant (Lagrangian) superficial charge density.

---

[1]Chrono-amperometry ($\Delta t > 0.1$ s) is an electrochemical technique in which the potential of the working electrode is stepped relative to the reference electrode and the considered signal is recorded as a function of time. As the same strategy as potentiostatic mode (Fig. 4.5), the variation of strain-induced potential is monitored *in situ* as a function of time at each controlled potential step with $R_D \approx 50$ kΩ.
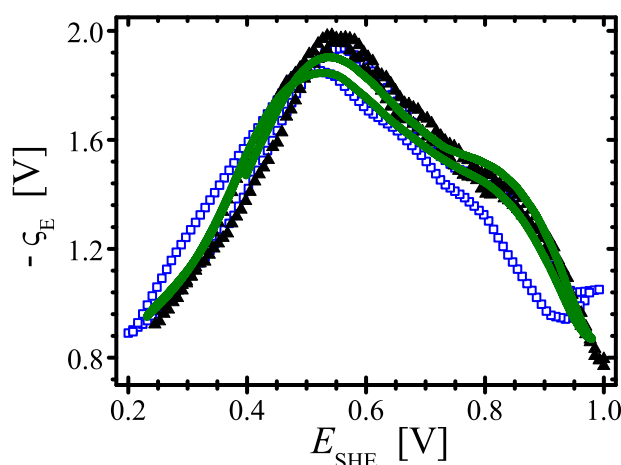
Figure 4.11: Results of potential-strain response, ς_E, obtained by three methods: current-strain response combining with impedance (▲ in black color); potentiostatic mode (– in olive color); and galvanostatic mode (□ in blue color). Note the excellent agreement.

4.3.5.1   Potential-strain response in galvanostatic mode

Here, current and strain are controlled and the potential variation is measured. Therefore, this mode is most directly linked to the derivative in question, a potential variation with strain at constant charge. However, the drawback is the weak connection to the established voltammogram database, which is measured under conditions of controlled potential, not controlled current. Furthermore, the software of standard potentiostat system does not allow itself to easy control of the vertex potential in galvanostatic mode.

4.3.5.2   Current-strain response in potentiostatic mode

Here, the current in response to strain is measured, and a separate measurement of the interfacial impedance is required to compute the potential-strain response by means of Eq. (4.16). This strategy has the advantage of introducing a separate database (current modulation and capacity as opposed to potential variation), making the verification more meaningful (*e.g.*, the method of current modulation can be applied to study the strain-induced Faraday current in a chemical reaction). The drawbacks are twofold. First, there is a need for separate impedance experiment. Second, and more importantly, the impedance measurement is not always conveniently done under identical conditions as the current modulation experiment. By using software (Fra 4.9, Metrohm), the potential is stepped and the impedance is measured at constant potential, typically for a succession of frequencies. By contrast, conventional cyclic voltammetry as well as current modulation data involves - at least approximately - a continuously varying potential. Therefore, whenever there is a hysteresis and/or scan-rate dependence in the electrode processes, the impedance data will not be measured at the same state of the electrode as the current modulation data. This difference is at odds with the requirements of Eq. (4.16).

4.3.5.3   Potential-strain response in potentiostatic mode

This appears as the most practicable method, which will directly supply ς_E based on a single measurement. This measurement can be performed under identical conditions as a cyclic voltammogram. The obvious advantage is that features in ς_E can directly be related to the known features in the voltammogram. The need for a delay resistance appears as a drawback, since features in the voltammogram will be shifted on the potential axis. However, after the potential correction, the impact on the voltammogram can be minimized when the mechanical cycling is fast and the potential scan rate is slow. In the present study, the delay resistance led to insignificant changes in the voltammogram where there is capacitive regime.

4.4   Application of measurement strategy

4.4.1   Polarisable and nonpolarisable electrodes

The potential-strain response, ς_E, was investigated in the potentiostatic mode using silver electrodes as polarisable electrode (PE) and nonpolarisable electrode (NPE) conditions.

A 100 nm thick vapor-deposited Ag film and a silver wire were used as the working and counter electrodes, respectively and the electrolyte consisted of 10 mM NaF as PE condition. Figure 4.12 shows that the potential-strain response of Ag and Au near the open circuit potential, E_{oc}, and under PE conditions vary in similar fashion with the frequency, ω, of the strain cycles. In particular, ς_E is indeed found negative for Ag, around -0.52 ± 0.05 V at large ω, and it was also found that $E_{oc} = 0.42 \pm 0.02$ V (*vs* SHE).
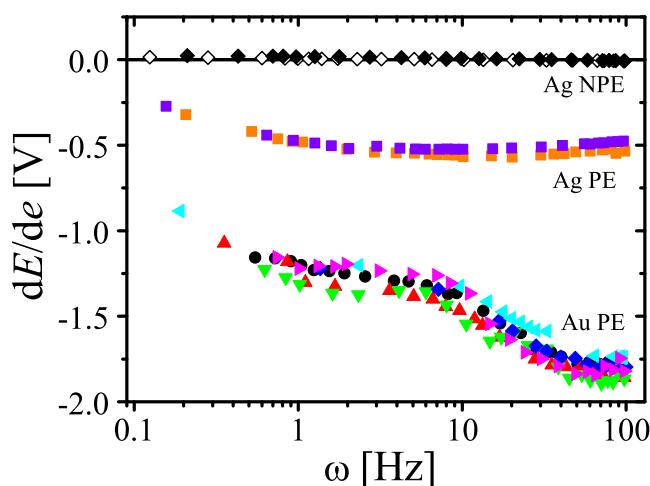
Figure 4.12: Potential-strain response, dE/de, at different conditions *versus* frequency, ω, of the strain cycles. Individual symbols refer to the response of different samples of Au in 10 mM HClO$_4$ (Au PE, data from Ref. [43]), Ag in 10 mM NaF (Ag PE), and Ag in 10 mM AgNO$_3$ (Ag NPE).

The experiment with the Ag electrode was also done under NPE conditions, using aqueous 10 mM AgNO$_3$ + 0.1 M KNO$_3$ as the electrolyte. Open circuit conditions were maintained at

all times in order to prevent dissolution. The resulting ς_E values for the NPE (Fig. 4.12) are positive signed for the frequencies below ~ 10 Hz and negative above this frequency. The ς_E magnitudes never exceed 25 mV here.

4.4.2 Frequency dependence

Figure 4.13 shows the dependence of ς_E for Au electrodes in 10 mM $HClO_4$ on cyclic strain frequency. In the higher frequency range ($\omega \gtrsim 3$ Hz) the measurement here used the potential-strain response method with the lock-in amplifier. The potential was $E_1 = 547$ mV, close to the potential of maximum $|\varsigma_E|$, shown in Fig. 4.11. At lower frequencies the data were recorded by means of chrono-potentiometry under open circuit conditions after conditioning at E_1. During the measurement the potential here remained within few mV of E_1. The magnitude of the (negative-valued) ς_E increases slightly with increasing frequency, apparently saturating around a value of -2 V at and beyond the strain frequency of 20 Hz.
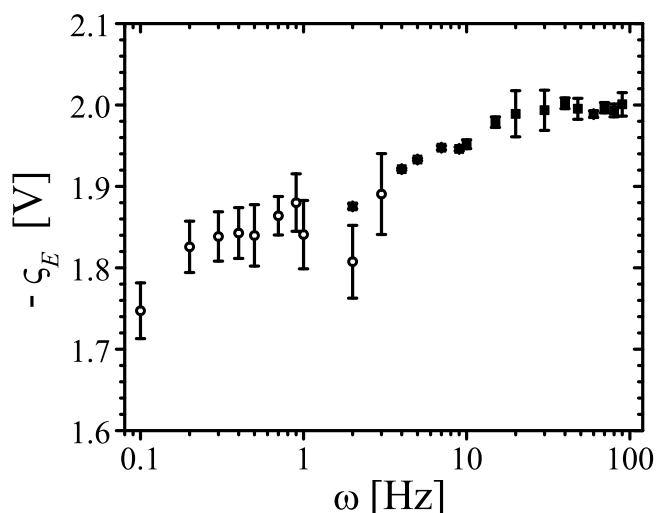
Figure 4.13: Potential-strain response, - ς_E, in 10 mM $HClO_4$ as the function of cyclic strain frequency, ω. Potential value is 547 mV, close to the maximum in $|\varsigma_E|$ shown in Fig. 4.11. Measurement of ς_E uses chrono-potentiometry under open circuit conditions (∘) or potential-strain response using a lock-in amplifier (∎) with the error bar (black line).

4.4.3 Application to different electrolytes

Further dynamic electromechanical spectroscopy experiments studied identically prepared Au electrodes but different electrolytes and different concentrations. Figure 4.14 summarizes results obtained with 1, 10 and 100 mM concentration solutions of $HClO_4$ as well as H_2SO_4. The experiments here show a sample-to-sample reproducibility in ς_E of ~ 5%. To further enhance the comparability, all results for each of the two types of electrolytes were here obtained with the identical sample, in sequence of increasing concentration.
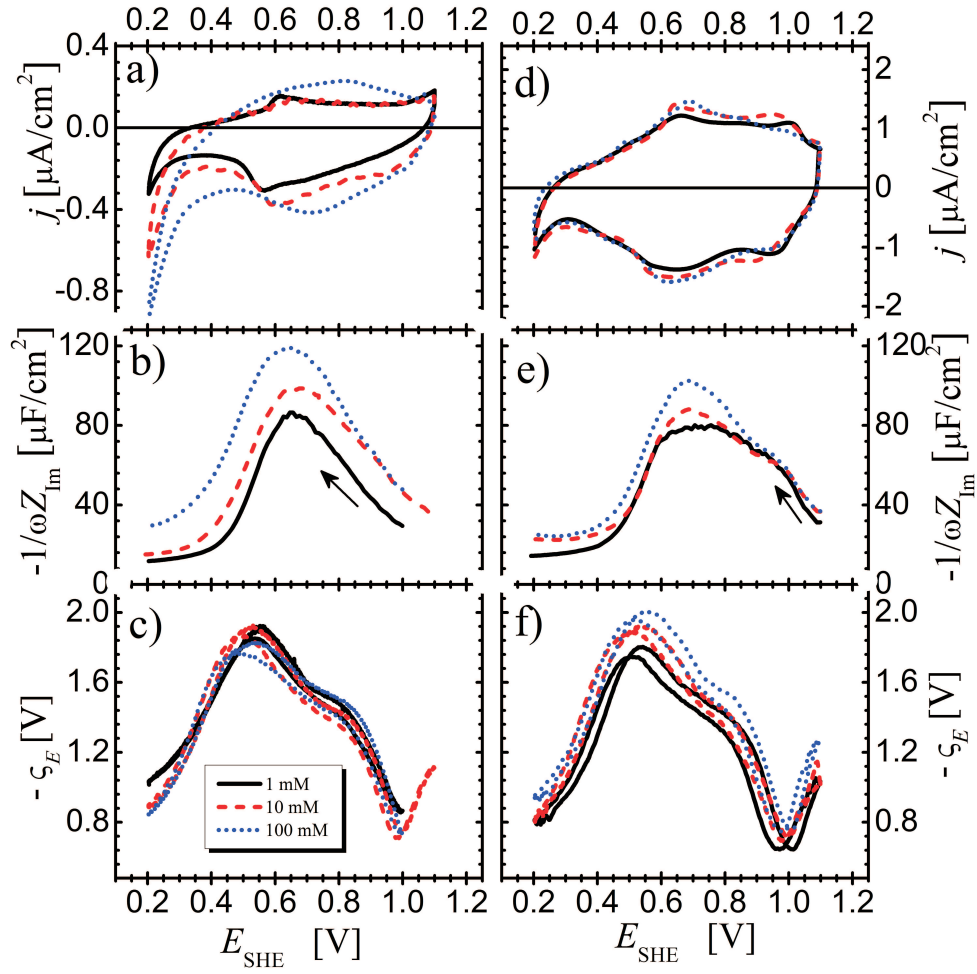
Figure 4.14: Results of dynamic electro-chemo-mechanical analysis of the gold surface measured in $HClO_4$ (left column) and H_2SO_4 (right column). Top row: cyclic voltammograms recorded *in situ*. Center row: apparent differential capacitance. Bottom row: response parameter, ς_E, measured via potential-strain response under potentiostatic control. Potential sweep rate: 1 mV s^{-1} in $HClO_4$ and 5 mV s^{-1} in H_2SO_4; frequency for impedance and potential-strain measurements, 20 Hz. Concentration of $HClO_4$ and H_2SO_4 depicted as: 1 mM - solid black line, 10 mM - dashed red line, 100 mM - dashed blue dots.

It is seen that the graphs of ς_E in $HClO_4$ and H_2SO_4 in Fig. 4.14 are quite similar. Their most prominent feature is the maximum in $|\varsigma_E|$. By averaging the potential, E_{max}, of the maximum over the electrolytes with different molarities and over both scan directions it is found that $E_{max} = 532 \pm 42$ mV in $HClO_4$ and $E_{max} = 532 \pm 40$ mV in H_2SO_4. Thus, the position of the maximum is independent of the electrolyte within narrow margins. E_{max} is invariably found negative of the potential of maximum capacitance as read from the CV or from the impedance data (665 $\pm$ 20 mV in $HClO_4$ and 680 $\pm$ 20 mV in H_2SO_4).

It is also seen that all graphs exhibit shoulders at around 800 mV and an inversion in slope at around 1000 mV. These features are also quite reproducible and independent of the elec-

trolyte. The most notable difference between the results of perchloric and sulfuric acid is the concentration dependence: as the function of molarity, the scans in $HClO_4$ exhibit a noticeable variation in capacitance but practically no variation in ς_E. By contrast, scans in H_2SO_4 give lesser capacitance variation yet a noticeable variation in ς_E.

4.4.4   Application to electrosorption processes

DECMA method of measuring potential-strain response, ς_E, in the potentiostatic mode is applied into specific adsorption processes on different transition noble metals (Au, Pt and Pd). The central differences here are the extension of the potential range in measurement to include the regimes of hydrogen and oxygen species electrosorption on the surfaces.

Gold electrode
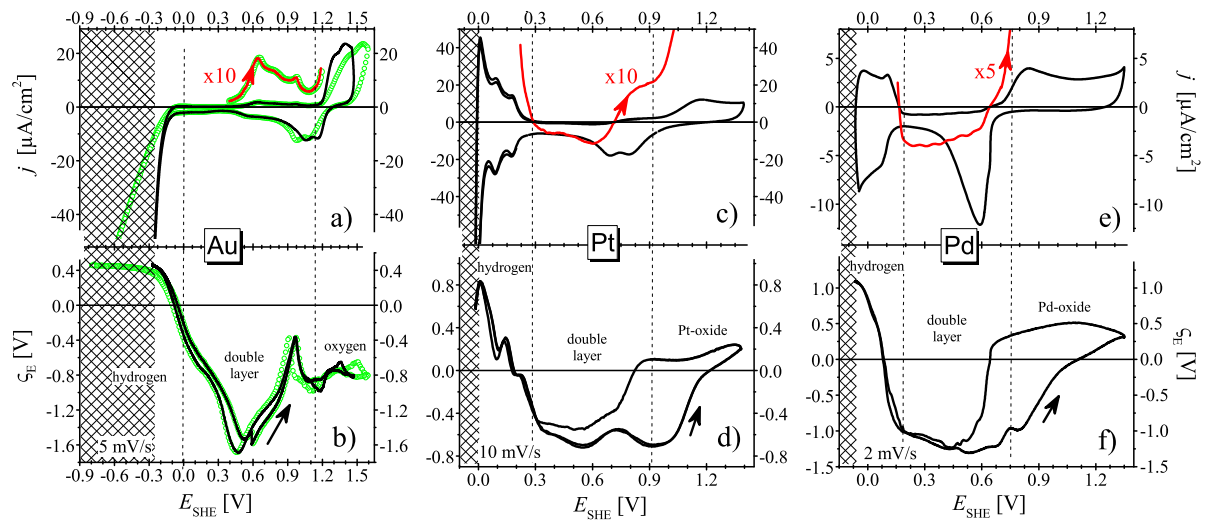
Figure 4.15: Results of dynamic electro-chemo-mechanical analysis at the strain frequency of 20 Hz: Au electrode in 0.1 M H_2SO_4 (left column); Pt electrode in 0.5 M H_2SO_4 (middle column) and Pd electrode in 0.01 M H_2SO_4 (right column). Top row: the *in situ* cyclic voltammograms. Bottom row: potential-strain response parameter, ς_E, as a function of the corrected electrode potential. The enlarged time on current scale, potential sweep rate and direction are indicated in the figures. Note the curves in a) and b) are also plotted as the function of the potential of E_{pot} (green dot lines) and of E_{we} (black solid lines) for a comparison.

Figure 4.15 (left column) show the DECMA data of the potential-strain coupling coefficient of the 111-textured polycrystal gold electrode in 0.1 M H_2SO_4. The *in situ* cyclic voltammogram recorded during DECMA is used to determine the electrode processes.

The parameters of interest, current density j in Fig. 4.15 a) and potential-strain response ς_E in Fig. 4.15 b), are plotted as the function of electrode potential, without (green dot lines) and

with (black solid lines) the correction of potential by Eq. (4.17)[1]. The potential range becomes smaller after the potential correction. More specifically, at the negative end of potential scan, the potentiostat displays a value of -0.8 V on the potential axis whereas the accurate potential on the gold electrode takes the value of -0.25 V. It is also seen that the ς_E exhibits an apparent plateau at highly negative electrode potential values, which is an artifact of the uncompensated solution resistance and which vanishes once the potential is corrected. The potential correction on the working electrode is therefore necessary and has been done to access the true potential value in this thesis.

Now turn to the observation of ς_E behavior. It varies significantly with the electrode process. The negative sign is consistent with the previous section in capacitive regime. Figure 4.15 b) implies that the amplitude of ς_E decreases with the more Gibbs excess of ions on the surface. The peak ($E \approx 1000$ mV), appearing on the *in situ* cyclic voltammogram, corresponds to the saturation of adsorbed anions SO_4^{2-} on the surface [114]. It is also seen that ς_E exhibits an inversion in slope at around 1000 mV.

Extending the scope to a wider potential range, and at the negative end of the potential scan, ς_E shows a positive-sign value of $\sim$ +0.5 V during the hydrogen adsorption. At the positive end of the potential scan, ς_E keeps the negative-signed value in whole oxygen electrosorption regime. The negative sign of oxygen species adsorption on the Au surface is in agreement with computational data in Ref. [13].

Platinum electrode

The DECMA results of 111-textured polycrystal platinum electrode in 0.5 M H_2SO_4 are shown in Fig. 4.15 (middle column), with typical Pt-H underpotential deposition, capacitive process and Pt-oxide regions.

The capacitive process is in a range of $E = 300 \sim 750$ mV, in which ς_E has its maximum amplitude value with a negative sign. Figure 4.15 d) shows parabolic dependence on the electrode potential as well, like the behavior of Au electrode. Further positive potential sweep around $E = 750$ mV in Fig. 4.15 d), the local minimum of ς_E in amplitude may be due to the saturated excess of anions (SO_4^{2-} and HSO_4^-). At the onset of oxidation ($E \approx 900$ mV), $|\varsigma_E|$ has a local extreme again and then starts to decrease until the sign of ς_E changes from negative to positive.

In the backward sweep, ς_E is positive valued in the regime of capacitive process on oxygen-covered surface or oxidized Pt surface. At the onset of backward sweep, the amplitude of ς_E increases within a narrow potential range ($\sim$ 50 mV). After that, ς_E decreases linearly until the electrode potential of $E = 1000$ mV, and keeps a constant value within potential window from $E = 1000$ mV to $E = 900$ mV.

The oxidized surface is reduced and ς_E starts to change rapidly after $E = 900$ mV, and with a sign change at $E \approx 800$ mV, then its amplitude reaches a maximum at $E \approx 550$ mV. However the amplitude of ς_E does not reach the identical state as it was at the onset of oxidation since the oxidized surface is not reduced completely. It is seen that the electrode reverts to clean surface again around the potential of 300 mV. When $E < 300$ mV, in the hydrogen electrosorption process, two peaks are exhibited corresponding to the underpotential deposition peaks, consistent with the *in situ* cyclic voltammogram shown in Fig. 4.15 c).

---

[1]The potential on the working electrode is affected by the presence of the delay resistance between the WE and potentiostat. For detail about the correction of electrode potential, see section 4.3.2.

One maximum peek appears at the curve of ς_E with a value of +0.85 V around the negative end of the potential scan. That is also around the equilibrium potential of the hydrogen evolution reaction ($E_{eq} = 0$ V *vs* SHE). The features of Fig. 4.15 for Pt metal are well compatible with observations of the surface stress variation with charge density during porous metal dilatometry experiments [32, 101].

Shaded regions mark the potential regime where the technique is inappropriate since the requirement of dominantly capacitive process is violated. There is not constant charge density condition for measuring ς_E in the potential regime of hydrogen evolution reaction. The hydrogen evolution reaction will be focused to study in the next Chapter 5 for further understanding in details (*e.g.*, the relationship between this mysterious peak and frequency of cyclic strain).

Similar physical phenomenon is observed for the Pd electrode shown in Fig. 4.15 as Pt.

Palladium electrode

As another example for the application of DECMA, Fig. 4.15 e) and f) show the *in situ* cyclic voltammogram as well as the data of $\varsigma_E(E)$ for Pd in dilute sulfuric acid. The potential interval here includes several electrode processes like Pt metal. Furthermore, it is seen that the values of $\varsigma_E(E)$ provide signatures of these processes.

At intermediate potentials, in the nominally capacitive regime of the voltammogram, ς_E exhibits a negative value at clean surface. In forward sweep direction, anions (SO_4^{2-} and HSO_4^-) adsorption at more positive potentials is accompanied by a decrease in $|\varsigma_E|$ and reach saturation around $E \approx 700$ mV. Around $E \approx 800$ mV, ς_E has a local extreme again, which can be considered as the onset of Pd oxidation. Then it starts to decrease its amplitude until the sign of ς_E changes from negative to positive. These features are also reproducible and similar as for the Pt metal except the different electrode potentials at the electrode states.

Since oxygen species are rather stable on the Pd surface, the negative-going scan at positive potentials involves dominantly capacitive processes on an oxygen-covered surface. Within this pseudo-capacitive process, ς_E has different features from the oxygen-covered Pt surfaces. In backward scan direction, there is firstly a larger potential range (~ 250 mV) for increasing the magnitude of ς_E than in the Pt situation. Then ς_E decreases with a slow rate in the potentials from $E = 1100$ mV to $E = 700$ mV without the performance of keeping the constant value process like Pt metal.

As the potential is lower than 700 mV (the negative sweep), the electrode process on the oxygen-covered surface converts from the pseudo-capacitive to the oxygen desorption. It is distinguished by a sharp decreasing value in $|\varsigma_E|$, then the sign of ς_E returns to negative. The Pd surface becomes clean at the potential of 450 mV since the values of ς_E are identical at forward and backward scans. At larger and negative potential, hydrogen adsorbs on the surface as well as absorbs into the bulk of Pd. This regime is again characterized by positive-valued ς_E with a value of +1.2 V at the negative end of the potential scan. The features of Fig. 4.15 f) are well compatible with the observations of porous metal expansion and pseudomorphic layer experiments [15, 32].

The notable difference between the DECMA results of Pd and Pt metals are the capacitive processes on oxygen-covered surfaces. The graphs in Fig. 4.15 d) and f) illustrate that ς_E exhibits more details for understanding the adsorption processes, which are not always apparent from cyclic voltammograms.

4.4.5 Discussion

Polarisable and nonpolarisable electrodes

In fact, the phenomenon of the strain-response of the electrode potential remains to this day either obscure – such as the numerical magnitude of $\varsigma_E(E)$ – or puzzling – such as the sign of $\varsigma_E(E)$ in the potential range near the *pzc* [43, 52, 115]. More specifically, the experimental results for gold electrodes as a polarisable electrode (PE) reported by Smetanin *et al.* [43] yielded a potential-strain response of $\varsigma_{oc} = -1.83$ V at the open circuit potential, close to the potential of zero charge for the Au electrode. However, the effect of mechanical stress on the potential of the silver electrode has studied earlier by Horváth *et al.* [52]. They obtained the value of potential-strain response, $\delta E_{zc}/\delta e = +1.0$ V, for Ag metal in aqueous AgNO$_3$ solution.

For the different results in the above two experiments one reason is that two electrode materials are different, Ag in Ref. [52] and Au in Ref. [43]. Since the presence of Ag$^+$ in solution makes the Ag electrode a nonpolarisable electrode (NPE), one more reason is that - at least nominally - the experiment in Ref. [52] is under NPE condition whereas the measurement in Ref. [43] at PE condition. Even for the same material, *ab initio* investigation so far shows the surface stress in response to charging, $\varsigma_f = -2.31$ V, of (111) surfaces for Ag metal [40]. Thus, the controversy, over the numerical magnitude and the sign of response near the *pzc*, comes from the misunderstanding, which should originate in the use of nonpolarisable electrode.

The theory of Ref. [43] has admitted separate values for the respective response parameters, $dE/de|_q$ for the PE and $dE/de|_\mu$ for the NPE (q: surface charge density, μ: chemical potential of the metal atom). Here, the comparative experiments with Ag electrodes clarified these issues under PE as well as NPE conditions to investigate the individual feature of potential-strain response. It thus provides a striking demonstration of the difference between the potential-strain response of polarisable and nonpolarisable electrodes. When using Ag metal as NPE in this study, the response value was positive signed for the frequencies below ~ 10 Hz and negative above this frequency. The response magnitude never exceeded 25 mV. While the Ag electrode as PE system, ς_{oc} was indeed found negative, around -0.52 ± 0.05 V at large ω. Open circuit potential, E_{oc}, was found at a potential of 0.42 ± 0.02 V *vs* SHE, which was around 1 V more negative than the potential of zero charge, E_{zc}. By applying Eq. (11) of Ref. [43], $\varsigma_{oc} = \varsigma_{zc} - (E_{oc} - E_{zc})$, to the processes far from E_{zc}, it is concluded that ς_{zc} may be as small as -1.52 V, which magnitude is close to the result of *ab initio* computation with an agreement of negative sign [40].

The impact of strain on the potential of zero charge (E_{zc}) of the PE dominates $dE/de|_q$. At a nonpolarizable electrode, the exchange current density near equilibrium is large enough to fix the electrode potential at the value given by the Nernst equation. The derivation $dE/de|_\mu$ of the NPE then represents the strain-dependence of the Nernst potential. The two parameters are thereby linked to variations of the chemical potential of the electron (PE) and of the metal atom (NPE), respectively. The strain-dependence of the Nernst potential is zero when measured at a NPE. The present experimental results show that the magnitude of $dE/de|_\mu$ for the NPE is about two orders less than the magnitude of $dE/de|_q$ for the PE condition, coinciding with the prediction of theory in Ref. [43].

The present results confirm: *i*) the prediction that ς_E of the NPE is small and *ii*) the speculation that ς_{zc} of Ag should be negative valued, similar to Au, which has since been supported by recent computational data [40]. In regard to the large and positive value of ς_E reported

in Ref. [52] for Ag material under nominally NPE conditions, it can be presumed as the Ag surfaces covered by an oxygen monolayer since the large and positive value of ς_E for oxygen-covered Pt surfaces has been observed [101]. The adsorbate might also reduce the exchange current density, making the electrode effectively polarisable even with Ag ions in solution.

Frequency dependence

By inspection of Fig. 4.13 it is seen that the magnitude of ς_E increases slightly with ω, apparently saturating at and above 20 Hz. The trend of $|\varsigma_E|$ increasing with increasing strain frequency agrees with earlier reports in Ref. [43], which is also shown in Fig. 4.12. There, the frequency dependence could be modeled as the consequence of Faraday loss currents, which violate the condition of constant q. The present data, however, vary much less with ω than what was found in the earlier work of Ref. [43]. The more stable behavior in the present experiments suggests a suppression of Faraday currents, which may be understood as the consequence of higher purity.

Different electrolytes

The experiments indicate that the graphs of $\varsigma_E(E)$ in $HClO_4$ and H_2SO_4 are in close agreement. These graphs are also at most weakly dependent on the electrolyte concentration. The value of $\varsigma_E(E)$ at the extremum, -1.9 ± 0.2 V in $HClO_4$, agrees with previously reported findings for ς_E at the open circuit potential [43].

The graphs of $\varsigma_E(E)$ of gold in the present work show identical sign in a wide potential interval around the pzc. Several authors have reported a dependency of the value of ς_E near the pzc on an effective strength of adsorption. When this latter parameter was varied, either by varying the ion [46] or the concentration [100], stronger adsorption was found to entail a smaller magnitude of ς_E. The observation has been linked to charge transfer between the electrode and the adsorbate and to the electrosorption valency [46, 48]. The present observations do not confirm that picture. The finding, that ς_E is essentially independent of the ion and of the solution concentration, appears to link ς_E exclusively to the behavior of the metal surface.

The data also offer no apparent link between the potential dependence of ς_E and simple concepts of the double-layer behavior near the pzc. For instance, the potential of maximum $|\varsigma_E|$ is near the potential of maximum capacitance, but the offset between the two potentials appears significant, preventing explanations based on a one-to-one correlation between ς_E and capacitance.

The most obvious empirical correlation to the known electrode processes is the good agreement between the potential of maximum $|\varsigma_E|$, E_{max}, and the potential of zero charge, E_{zc}. Within error bars, the value of E_{max} agrees with the pzc of Au(111) in $HClO_4$, 560 mV [116], and in solutions containing SO_4^{2-}, ~500 mV [117]. Note that the electrocapillary maximum of the surface tension is a forceful result of thermodynamics. By contrast, thermodynamics will neither require nor rule out an extremum of $\varsigma_E(E)$ near the pzc. More recently, Lafouresse *et al.* [50] experimentally studied another parameter at Maxwell relation, coefficient of surface stress in response to charge density (ς_f), in a wide potential range within double layer. They obtained results of potential-dependent ς_f of Au metal in agreement with the present results here. However, their experiments showed the value of E_{max} was not exact at E_{zc}. Further experimental and theoretical analysis are therefore required to understand in detail. Yet, if the finding, linking the

E_{max} and E_{zc}, was confirmed, and if the controlling role of the metal in the surface potential-strain response was taken at face value, then the extremum of $\varsigma_E(E)$ would provide a useful probe of the pzc of gold, which could be applied in general in electrochemical studies.

Irrespective of the above issue, an interpretation of $\varsigma_E(E)$ as a signature of the metal surface imposes the question of the origin of the dependency on potential or superficial charge density. One might speculate about band-filling by the excess charge, and in fact the issue would seem to be open to investigation by *ab initio* density functional theory approaches such as those of Refs. [37–40, 118].

Electrosorption processes

Measurement of the potential variation with strain, ς_E, was first reported in early work by Gokhshtein [41] (summarized by Valincious in Ref. [42]), who proposed the estance method as a technique for measuring ς_E. The results of DECMA-data of ς_E of Pt metal under the present study are decomposed into two curves of forward and backward scans, respectively, so as to compare with the earlier results published by Gokhshtein, shown in Fig. 4.16.
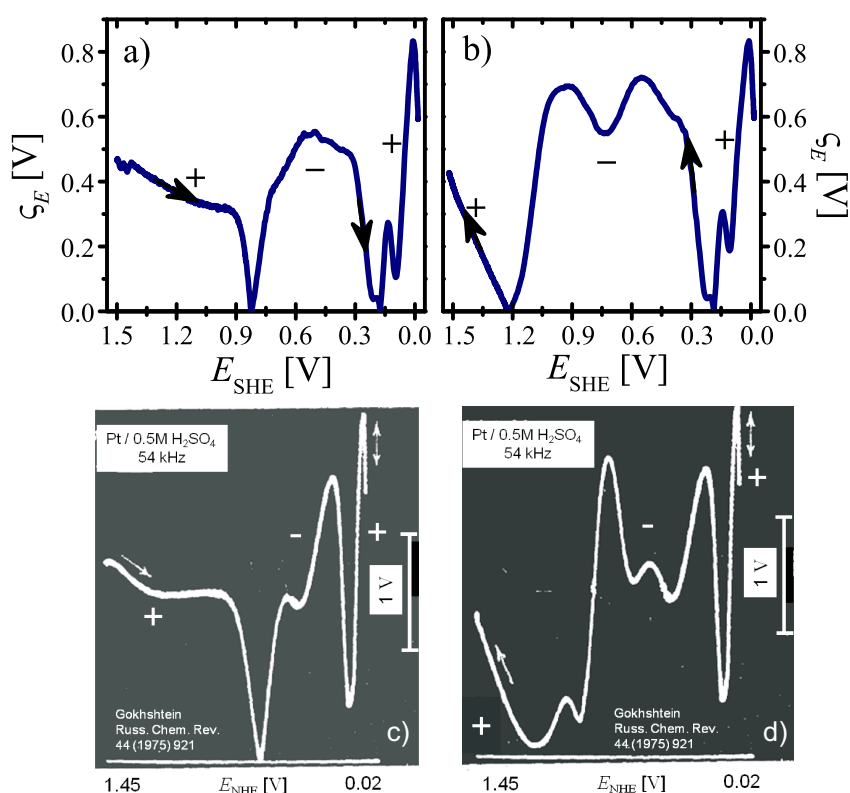
Figure 4.16: Experimental verification by a comparison of DECMA and estance methods. Top graphs **a,b**): present DECMA results of Pt surface in argon-purged 0.5 M H_2SO_4. Bottom graphs **c,d**): curves taken from Ref. [41] by Gokhshtein's estance method. Arrow indicates scan direction for forward and reverse curves of ς_E. Marks "+" and "-" indicate the sign of ς_E in the respective regions of the graph. Representation of present data has been adapted to compare the features of the reference data: **a,c**) negative and **b,d**) positive sweeps.

A comparison of DECMA and estance methods illustrates the agreement of major features in both scan directions. Yet, the absolute values of ς_E by DECMA are here smaller than the results of estance method [41]. These values in different electrode processes by DECMA method will now be discussed in relation to the literature.

The parameter ς_E here is quantified -0.8 ± 0.1 V by DECMA for clean surfaces of Pt electrodes near *pzc*. The value here is consistent with the earlier published data, which show the parameter ς_f, surface stress *versus* charge density, of -1.0 ± 0.1 V [101]. Moreover, DECMA observations conclude that ς_E for hydrogen adsorption is positive valued with a lower bound of +1.2 ± 0.2 V on Pd and of +0.9 ± 0.2 V on Pt. The findings of ς_E are consistent with positive value +1.7 ± 0.3 V in experiments for Pd [32, 102, 103] and +1.5 ± 0.1 V for Pt [32, 101] for hydrogen electrosorption. In the present DECMA experiments of ς_E, the metal electrodes typically worked under study with the surfaces, which were not perfectly single crystals. They contained defects such as step edges and terraces. The difference in magnitude in comparison with literature may be as a result of the surface roughness. Irrespective of the above issue, the present measurement of DECMA is thus a convenient and precise tool of quantifying $\varsigma_E(E)$.

An alternative method to investigate the parameter ς_E is the strained monolayers by epitaxy to different substrate crystals as in Ref. [15], in which the value of ς_E was calculated in Ref. [32] showing +1.4 ± 0.2 V for hydrogen desorption on Pd surface. The agreement of ς from two approaches demonstrates cyclic and misfit strain displaying the same electrochemical processes. Moreover, the trend observed in the data of Ref. [15] for hydrogen electrosorption on pseudomorphic layers is in fact dominated by the response of adsorption potential to strain. In other words, the present experiment supports the finding, the impact of change in interatomic spacing on the reactivity, that has been predicted on theoretical analysis [25–28], For using cyclic strain method (DECMA), one of the advantages is quite convenient to study the strain effect for continuous change of electrode potential during cyclic voltammetry. It can also avoid the challenging steps of preparing the pseudomorphic layers and measuring their precise strain.

By the DECMA technique, the parameter of potential-strain response of interest for all active electrosorption processes can be detected and quantified within one measurement. The present findings of ς_E exhibit that the different signs of ς_E in different electrode states for Au, Pd and Pt transition nobel metals. At clean metal surfaces, the sign of ς_E stays negative within capacitive regime. The parameter ς_E changes its sign during oxygen species adsorption on Pt and Pd electrodes. However, no sign inversion has been seen in the present experiments during the whole potential range of oxygen adsorption on Au. This observation relates to the formation of an oxide monolayer on Pd and Pt but not on Au. One of the reasons is that the Au metal is not so active as Pd and Pt materials to oxidize. In other words, the oxidized rate of Au is quite slow than the cyclic strain. As one example to support this view, Jin *et al.* [119] found that positive sign of ς_f in capacitive processes using nanoporous gold material formed with a monolayer of strongly adsorbed oxygen.

Pseudo-capacitive processes during negative-going scans with the oxygen-covered surface exhibit positive ς_E, while pseudo-capacitive processes on the nominally clean surface have negative ς_E. For all metals in study (Au, Pt and Pd), the ς_E values are positive during hydrogen adsorption at surfaces. In fact, quantifiable measurement of ς_E during hydrogen adsorption on gold surfaces have not been reported so far, even the sign. These experiments therefore imply the same trend, enrichment for tensile strain, for adsorption of hydrogen as well as oxygen.

4.5 Conclusion

This chapter has successfully established the strategies for measuring the coupling parameter of electrode potential and elastic strain, ς_E, at constant superficial charge density condition. The parameter ς_E can be detected and quantified during a traditional cyclic voltammetry by removing the restriction of open circuit condition and imposing a cyclic strain control. The strategies successfully separate the cyclic variation of potential/current from the voltammogram proper.

The strategies have been validated by three independent different experimental methods in this chapter. When applied to gold electrodes in weakly adsorbing electrolytes, 10 mM $HClO_4$, all three strategies provided consistent results for ς_E. This prefect agreement of data, from the strategies with narrow margins throughout the entire potential range in study, gave a strong indication that the experiments provided valid data for the electrocapillary parameter ς_E. The first finding is that ς_E is strongly dependent on electrode state, in other words, this parameter is a function of electrode potential, namely $\varsigma_E = \varsigma_E(E)$. The second finding of ς_E is that its sign is always negative in the capacitive (or pseudo-capacitive) process at clean gold surfaces. The third finding is that $\varsigma_E(E)$ has an extremum value, -1.9±0.2 V in 10 mM $HClO_4$, in agreement with previously published data for ς_E near the potential of zero charge.

The agreement of the various methods validated the analysis of the underlying science and showed that the developed method, dynamic electro-chemo-mechanical analysis (DECMA), can be used as a tool for characterizing electrode processes. The DECMA method for measuring $\varsigma_E(E)$ was thus applied to study different electrochemical systems.

The polarisable electrodes (PE) and nonpolarisable electrodes (NPE) were investigated as well to clarify the confusion of different behavior of potential-strain response. At a nonpolarizable electrode, the exchange current density near equilibrium was large enough to fix the electrode potential at the value given by the Nernst equation. The derivation $dE/de|_\mu$ of the NPE then represents the strain-dependence of the Nernst potential while the impact of strain on the potential of zero charge of the PE dominated $dE/de|_q$. The two parameters were thereby linked to variations of the chemical potential of the electron (PE) and of the metal atom (NPE), respectively. Experimental results showed that the magnitude of $dE/de|_\mu$ for the NPE was about two orders less than the magnitude of $dE/de|_q$ for the PE condition. The $dE/de|_q$ for the PE condition showed a really negative-signed value whereas positive-signed $dE/de|_\mu$ for the NPE at low strain frequency.

As a case-study the DECMA method has been applied to gold electrodes in $HClO_4$ and H_2SO_4 of different concentrations. The most obvious observation was a peak in the magnitude of $\varsigma_E(E)$ at a potential which coincided with the pzc. Furthermore, the experimental graphs of $\varsigma_E(E)$ were at best weakly dependent on the nature of the electrolyte, suggesting that the experiment probed the signature of electronic processes in the metal surface.

The DECMA measurement was applied further to the electrosorption processes on different surfaces of noble metals (Au, Pt and Pd). The results of ς_E showed several changes of the sign during the different electrode processes. It was found that the ς_E value was positive during hydrogen adsorption for three metals in study. Contrary to Au, ς_E changed its sign during oxygen adsorption for Pd and Pt metals. This observation related to the formation of an oxide monolayer on Pd and Pt but not on Au. Since the electrode potential measured the adsorption enthalpy in the hydrogen or oxygen adsorption, no zero value of parameter ς_E implied that the

strain affected significantly the adsorption enthalpy. The study of strain-dependent enthalpies will be continued in the subsequent chapter.

Besides the successful database of potential-strain response, another important coefficient, the response of electrode current to strain at constant potential condition, has been also determined, which can be applied directly to study the strain-dependence of Faradaic current in an electrochemical reaction. The study in Chapter 5 will focus on the impact of surface strain on the catalytic activity by the strain-dependent adsorption enthalpy and the strain-dependent activation enthalpy.

Chapter 5

Mechanically modulated electrocatalysis

This chapter explores the focus of research of how the catalytic activity is affected by the surface strain, focusing on the hydrogen evolution reaction (HER) on gold and platinum electrodes in H_2SO_4 solution as a model process. The kinetic rate equations for Heyrowsky and Tafel steps of the HER are introduced firstly to allow the strain-dependence of the hydrogen adsorption enthalpy as well as the barrier energy. In the experiments, the modulation of reaction current can be precisely detected *in situ* by a modified DECMA while a small cyclic elastic strain is imposed on the electrode material.

5.1 Theory section

5.1.1 Modulation of reaction current at constant potential

The task here is to analyze the modulation of the reaction current in response to the cyclic strain at constant potential condition. This requires a distinction between capacitive or pseudo-capacitive processes (where charge is stored in the outer or inner Helmholtz layers) on the one hand and Faraday reactions (where charge is transported to or from the electrode by the products of a catalytic reaction) on the other.

Considering a cyclic strain, $e = \hat{e}\sin(\omega t)$ as the same as in Eq. (4.1), on polarizable electrodes, the experiment of pseudo-capacitive behavior near equilibrium has been explored in Chapter 4, with either the charge density or the electrode potential held at constant value, respectively, in the potential- or current- modulation:

$$
\begin{aligned}
E &= \varsigma\hat{e}\sin(\omega t) & (\text{constant } q)\,, & \quad (5.1) \\
j &= -\varsigma c\omega\hat{e}\cos(\omega t) & (\text{constant } E)\,. & \quad (5.2)
\end{aligned}
$$

The DECMA experiments in previous chapter have verified that the electrocapillary coupling parameter, ς[1], can be consistently measured by each of the two experimental approaches.

---

[1]Since the parameter of surface stress-charge response is not involved in this chapter, the notation of potential-strain response, ς_E shown in Chapter 4, is replaced by simple ς.

We now turn to non-equilibrium processes and start out by assuming that the specific charge density q remains well-defined there. The net current density, j (current per area), can then be decomposed into pseudo-capacitive ($j^{\mathrm{pc}} = \mathrm{d}q/\mathrm{d}t$) and Faraday ($j^{\mathrm{F}}$) current contributions. The interest in this thesis is in processes where potential and/or strain vary, and it is assumed that the transitions, in which j^{F} takes on the new steady-state value for the current values of E and e, occur much faster than the potential- or strain cycles[1]. Then, j satisfies

$$j = \mathrm{d}q/\mathrm{d}t + j^{\mathrm{F}}(E, e).$$ (5.3)

The expression $j^{\mathrm{F}} = j^{\mathrm{F}}(E, e)$ is the constitutive assumption for the Faraday current. With attention to small strain, as in a DECMA experiment, the expression can be expanded to first order as $j^{\mathrm{F}}(E, e) = j_0^{\mathrm{F}}(E) + \iota e$, with

$$\iota = \mathrm{d}j^{\mathrm{F}}/\mathrm{d}e|_E$$ (5.4)

a current-strain coupling coefficient. As will become apparent below, it is also of interest to introduce an alternative measure for the current-strain coupling in the form of the coefficient λ, defined as

$$\lambda = \frac{RT}{F} \frac{1}{j^{\mathrm{F}}} \frac{\mathrm{d}j^{\mathrm{F}}}{\mathrm{d}e}|_E.$$ (5.5)

This parameter measures the relative variation (variation of $\ln j^{\mathrm{F}}$) of the Faraday current.

The notation introduced so far can be written

$$j = j_0^{\mathrm{F}} - \varsigma c \omega \hat{e} \cos(\omega t) + \iota \hat{e} \sin(\omega t)$$ (5.6)

for the modulated current during strain cycles at constant potential condition. The first term on the right-hand side of Eq. (5.6) is the Faraday current at $e = 0$, the second term originates from pseudo-capacitive processes as in Chapter 4, and the third term is the modulated Faraday current of interest in this chapter.

With attention to DECMA experiments at small strain (in the present work, $\hat{e} \approx 2 \times 10^{-4}$) all materials parameters in Eq. (5.6) are taken as evaluated at $e = 0$ and this thesis focuses on their potential-dependence alone. Thus, $c = c(E)$, $\varsigma = \varsigma(E)$, $\iota = \iota(E)$, and $\lambda = \lambda(E)$.

Equation (5.6) suggests characteristic signatures of the pseudo-capacitive and the Faraday processes which afford their separation in experiment: the pseudo-capacitive modulated current is phase-shifted by 90° relative to the strain signal, whereas the modulated Faraday current is in phase of strain. Furthermore, the modulated pseudo-capacitive current scales with the frequency of strain, whereas the modulated Faraday current is invariant during frequency change.

5.1.2   Kinetic rate equation of hydrogen evolution reaction

A rate equation is introduced in this section. With attention to the hydrogen evolution reaction (HER) on Au, it is assumed that the rate-controlling step may be taken as the ion+atom

---

[1]Potential relaxation experiments on Au in acidic solution indicate that the hydrogen coverage follows potential jumps in the HER regime with a characteristic transition time constant, τ, of ~ 1ms [120]. This is much faster than the strain cycles of our experiments at frequencies ≤ 70 Hz, thereby justifying the assumption of quasi-instantaneous equilibration.

(Heyrowsky) reaction, $H_{aq}^+ + H_{ad} + e^- \rightleftharpoons H_2$ [96, 97]. The discharge (Volmer) step of hydrogen evolution reaction, $H_{aq}^+ + e^- \rightleftharpoons H_{ad}$, is taken to be fast. Consistent with that assumption, the coverage θ with hydrogen at any given value of the electrode potential is assumed to take on the equilibrium value consistent with the appropriate adsorption isotherm. Based on these assumptions, Parsons [93] has given a rate equation for the reaction kinetics as in Chapter 2, and the resulting Faraday current can be written in the form (see, for instance, Ref. [121])

$$ j^{\mathrm{F}} = j^{\mathrm{ex}} \left\{ \frac{1-\theta}{1-\theta_{\mathrm{eq}}} \exp\left(\frac{(1-\alpha)F\Delta E}{RT}\right) - \frac{\theta}{\theta_{\mathrm{eq}}} \exp\left(\frac{-\alpha F\Delta E}{RT}\right) \right\}. \tag{5.7} $$

The symbols have the following meaning: ΔE - overpotential relative to the equilibrium potential of the HER, F - Faraday constant, R - gas constant, T - temperature, α - symmetry parameter, θ - coverage, defined as the fraction of occupied adsorption sites, θ_{eq} - coverage at the equilibrium potential of the HER. The exchange current density, j^{ex}, obeys

$$ j^{\mathrm{ex}} = \mathrm{const.} \exp\left(-\frac{\Delta h^{\mathrm{ex}}}{RT}\right), \tag{5.8} $$

where the activation enthalpy Δh^{ex} relates to the energy barrier for the combination of proton and adsorbed hydrogen, which can be defined as indicated in Fig. 5.1. The two summands in the curly bracket of Eq. (5.7) represent the backward and forward reaction rates, consistent with the notion that the forward HER step consumes adsorbed H (scaling with θ) whereas the backward step inserts H into vacancies of the adsorbate phase (scaling with $1-\theta$). The denominators, which depend on θ_{eq}, may be viewed as normalization factors that assert the principle of detailed balance at $\Delta E = 0$. The exponentials account for the fact that the overpotential acts to shift the energies of the initial and final states, relative to each other, by the amount $F\Delta E$.
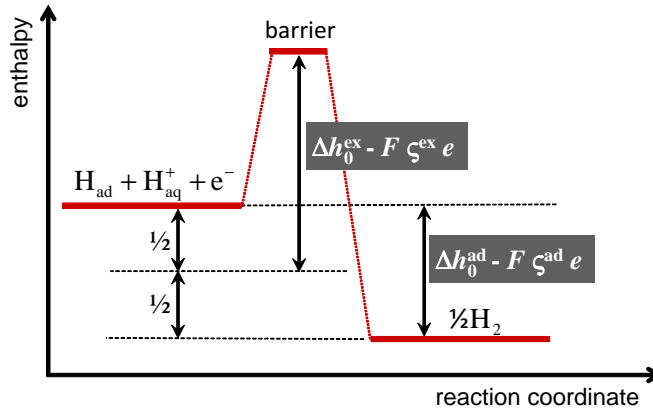
Figure 5.1: Schematic representation of enthalpy terms in the rate-equation for the Heyrowsky reaction with symmetry factor $\alpha = \frac{1}{2}$. The small strain e is taken to affect the values of the adsorption enthalpy Δh^{ad} and of the barrier height Δh^{ex} through the coupling parameters ς^{ad} and ς^{ex}, respectively.

The implications of Eq. (5.7) for the kinetics can be inspected for the idealized case where the adsorbate may be described as an ideal solution on a lattice with a fixed number of sites,

neglecting the adsorbate-adsorbate interaction energy. The coverage then follows the Langmuir isotherm, which can be represented by the function [94, 122]

$$\theta^{\mathrm{L}} = \left(1 + \exp\frac{\Delta g^{\mathrm{ad}} + F\Delta E}{RT}\right)^{-1}, \tag{5.9}$$

with

$$\Delta g^{\mathrm{ad}} = \Delta h^{\mathrm{ad}} - T\Delta s_0^{\mathrm{ad}}, \tag{5.10}$$

the free energy of adsorption. All molar quantities are per mole of H. The adsorption enthalpy Δh^{ad} represents the change in molar enthalpy for the reaction $\frac{1}{2}\mathrm{H}_2^{\mathrm{gas}} \to \mathrm{H}_{\mathrm{ad}}$ (see Fig. 5.1), and Δs_0^{ad} refers to the corresponding entropy change, accounting for the entropies in the gas and for a θ-independent vibrational entropy of the adsorbed H, but excluding the configurational entropy of the adsorbate phase.

Figure 5.2 is a schematic display of selected quantities of the model, showing the Langmuir isotherm in part a). The potential of electrosorption, E^{ad}, marks the transition between low and high adsorbate coverage. Figure 5.2 b) shows a schematic Tafel plot for the HER as modeled by Eq. (5.7). It is noteworthy that the "Tafel slope", $\mathrm{d}E/\mathrm{d}\ln j^{\mathrm{F}}$, changes at E^{ad}.

5.1.3 Impact of strain on reaction rate equation

The impact of strain on the reaction kinetics is inspected now as embodied in Eq. (5.7). The coupling coefficients ι and λ are used as a measure for the strain-dependence and the values of coefficients are governed by the strain-derivative of the rate equation. The terms $F\Delta E$ in the kernels of the exponentials in Eq. (5.7) represent the driving force for the reaction. This driving force is independent of the strain of the electrode, since the reactants and products are in solution. However, the established strain-dependence of the adsorption and barrier energies requires that the coverage terms θ and θ_{eq} and the exchange current density j^{ex} are allowed to depend on the strain. Denoting the respective strain-derivatives by θ', θ'_{eq} and $j^{\mathrm{ex}\prime}$, one can express the strain-derivative of Eq. (5.7) by

$$
\begin{aligned}
\iota = {} & j^{\mathrm{ex}\prime}\left\{\frac{1-\theta}{1-\theta_{\mathrm{eq}}}\exp\left(\frac{(1-\alpha)F\Delta E}{RT}\right) - \frac{\theta}{\theta_{\mathrm{eq}}}\exp\left(\frac{-\alpha F\Delta E}{RT}\right)\right\} \\
& + j^{\mathrm{ex}}\left\{\frac{(1-\theta)\theta'_{\mathrm{eq}} - (1-\theta_{\mathrm{eq}})\theta'}{(1-\theta_{\mathrm{eq}})^2}\exp\left(\frac{(1-\alpha)F\Delta E}{RT}\right) - \frac{\theta\theta'_{\mathrm{eq}} + \theta_{\mathrm{eq}}\theta'}{\theta_{\mathrm{eq}}^2}\exp\left(\frac{-\alpha F\Delta E}{RT}\right)\right\}.
\end{aligned}
\tag{5.11}
$$

Besides the strain-dependent exchange current density, the terms θ' and θ'_{eq} in this equation emphasize that the coupling of reactivity to strain is formally linked to variations of the coverages not only at potential (θ') but also at equilibrium (θ'_{eq}).

The implications of the strain-dependent terms in Eq. (5.11) may be inspected in more detail when the strain-dependent energies - as suggested by theory and experiment - are explicitly introduced. Specifically, here the impact of strain on the reaction kinetics is taken to be mediated by two factors, namely i) a strain-dependence of the activation enthalpy for the ion+atom reaction step, and ii) an independent strain-dependence of the hydrogen adsorption enthalpy.
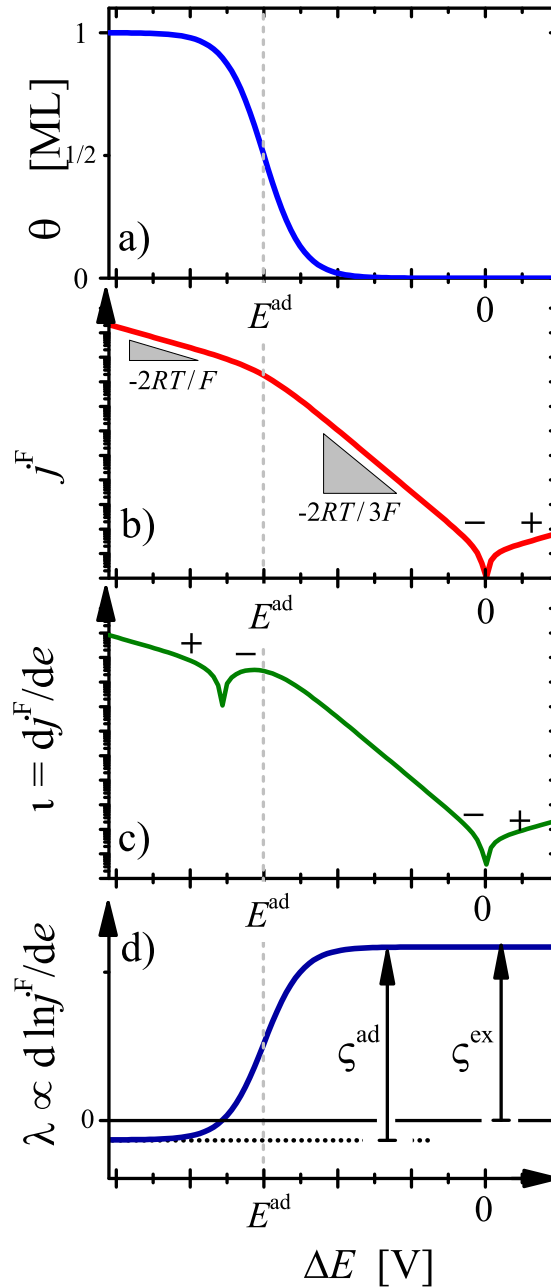
Figure 5.2: Schematic representation of variation, as the function of overpotential, ΔE, of quantities relevant for the discussion of Heyrowsky reaction kinetics: **a.)** surface hydrogen coverage, θ. **b.)** Tafel plot of current density, j^F on logarithmic scale. Note change in Tafel slope (as indicated by labels, here for symmetry factor $\alpha = 1/2$) at the potential, E^{ad}, of hydrogen electrosorption. **c.)** current-strain response, ι, also on logarithmic scale. **d.)** current-strain coupling coefficient, λ. A jump in λ by the amount ς^{ad} concurs with the transition between dilute ($\theta \ll 1$) and concentrated ($\theta \approx 1$) hydrogen adsorbate population at E^{ad}. ς^{ad} and ς^{ex} measure the strain-dependence of the H adsorption enthalpy and the activation barrier energy, respectively. The graph of $\lambda(E)$ also depends on the strength of adsorption, see main text and Table 5.1. Marks "+" and "-" indicate the sign of parameters j^F and ι in the respective regions of the graph.

It is advantageous to define, for the two enthalpies in question, response parameters ς^{ad} and ς^{ex}, so that they correspond to the potential-strain response in certain limiting cases. This is achieved by expressing the strain response through Ref. [32], ignoring the impact of strain on the vibrational entropy:

$$\Delta h^{\mathrm{ad}} = \Delta h_0^{\mathrm{ad}} - F\varsigma^{\mathrm{ad}}e \,, \tag{5.12}$$

$$\Delta h^{\mathrm{ex}} = \Delta h_0^{\mathrm{ex}} - F\varsigma^{\mathrm{ex}}e \,. \tag{5.13}$$

The strain-dependence of Δh^{ad} propagates into a strain-dependence of the coverage at equilibrium, and for the Langmuir isotherm specifically $\theta = \theta^{\mathrm{L}}(E, e)$. With attention to Eq. (5.11) it is important to note that the strain-dependence needs to be carried through to the coverage at the equilibrium potential. Otherwise, the principle of detailed balance would be violated for the strained surface and the reaction current at equilibrium deviate from zero. Thus, we have $\theta_{\mathrm{eq}} = \theta^{\mathrm{L}}(E_{\mathrm{eq}}, e)$.

Equation (5.11) can be drastically simplified by exploiting the assumptions introduced above concerning the adsorption isotherm and the strain-dependent enthalpies. Equations (5.9) and (5.12) for the isotherm imply

$$\frac{\mathrm{d}\theta^{\mathrm{L}}}{\mathrm{d}e}\Big|_{\Delta E} = \frac{F\varsigma^{\mathrm{ad}}}{RT}\theta^{\mathrm{L}}\left(1 - \theta^{\mathrm{L}}\right) \tag{5.14}$$

for the strain-derivative of the coverage function θ^{L}. Similarly, the strain-dependent activation enthalpy has the consequence that the exchange current density varies with strain as

$$\frac{\mathrm{d}j^{\mathrm{ex}}}{\mathrm{d}e} = \frac{F\varsigma^{\mathrm{ex}}}{RT}j^{\mathrm{ex}} \,. \tag{5.15}$$

By inserting the above two results into Eq. (5.11), and in view of Eq. (5.7), it is readily found that

$$\iota = \frac{F}{RT}\left(\varsigma^{\mathrm{ex}} + \left(\theta_{\mathrm{eq}} - \theta\right)\varsigma^{\mathrm{ad}}\right)j^{\mathrm{F}} \,. \tag{5.16}$$

In view of its definition through Eq. (5.5), the response parameter λ takes on the even simpler form

$$\lambda = \varsigma^{\mathrm{ex}} + \left(\theta_{\mathrm{eq}} - \theta\right)\varsigma^{\mathrm{ad}} \,. \tag{5.17}$$

The analysis above can readily be applied to the kinetics when the Tafel reaction, $2\mathrm{H}_{\mathrm{ad}} \rightleftharpoons \mathrm{H}_2$, is the rate-determining step, which has been suggested for the HER on Pt surfaces at low overpotential [77, 120, 123, 124]. Here, instead of Eq. (5.7), the reaction current is given by (see, e.g., Ref. [123])

$$j^{\mathrm{F}} = j^{\mathrm{ex}}\left\{\frac{(1-\theta)^2}{(1-\theta_{\mathrm{eq}})^2}\exp\left(\frac{(1-\alpha)2F\Delta E}{RT}\right) - \frac{\theta^2}{\theta_{\mathrm{eq}}^2}\exp\left(\frac{-\alpha 2F\Delta E}{RT}\right)\right\} \,. \tag{5.18}$$

Proceeding as before, the coupling coefficient can be obtained as

$$\lambda = \varsigma^{\mathrm{ex}} + 2\left(\theta_{\mathrm{eq}} - \theta\right)\varsigma^{\mathrm{ad}} \,. \tag{5.19}$$

Equations (5.17) and (5.19), the central results of analysis here, are forceful consequences of assuming Heyrowsky or Tafel kinetics, respectively, with a Langmuir isotherm and strain-dependent adsorption and activation enthalpies. The result expresses the current-strain coupling

coefficient λ as a weighted sum of the two relevant electrocapillary coupling parameters, ς^{ad} and ς^{ex}. The weighting factor emerges as linearly dependent on the H coverage. That implies that λ may vary significantly near the potential of electrosorption E^{ad}, while it takes on approximately constant values at more negative or more positive potentials. The results for Heyrowsky and Tafel kinetics are formally similar, and differ only by the fact that the adsorption-strain coupling in the Tafel case is weighted by an extra factor of two.

Figures 5.2 c) and d) illustrate the predicted mechanical modulation of the reactivity by means of qualitative graphs of $\iota(E)$ and $\lambda(E)$, respectively. The figure refers to Heyrowsky kinetics with a Langmuir isotherm as an example. It is remarkable that the coupling parameter λ remains well-behaved near the equilibrium potential of the reaction. When the current density (j^{F}) inverts its sign along with the overpotential, ι also changes sign as is apparent from a cusp in the logarithmic graph of ι at $\Delta E = 0$ in Fig. 5.2 c). Yet, λ retains the constant value ς^{ex} at and around $\Delta E = 0$. As Table 5.1 puts $\lambda \approx \varsigma^{ex}$ near equilibrium, it is seen that this coefficient here measures the strain-dependence of the exchange current density.

Table 5.1: Values of the reaction rate-strain coupling coefficient λ as predicted by Eq. (5.17) for Heyrowsky kinetics with a Langmuir isotherm. Results are for surfaces with different free energy of adsorption, Δg^{ad}, for hydrogen. Examples for materials with the respective adsorption strength are indicated for illustration. The three limiting cases of the overpotential, ΔE, refer to concentrated (coverage $\theta \approx 1$) and dilute ($\theta \ll 1$) adsorbate and to the equilibrium, at $\Delta E = 0$, of the hydrogen evolution reaction ($\theta = \theta_{eq}$). Electrocapillary coupling parameters for the activation barrier of the Heyrowsky reaction and for the hydrogen adsorption enthalpy are denoted by ς^{ex} and ς^{ad}, respectively. Note that λ jumps by $-\varsigma^{ad}$ when the surface undergoes the transition from dilute to concentrated adsorbate during hydrogen electrosorption.

	$\Delta E \ll -\Delta g^{ad}/F$ $\theta \approx 1$	$\Delta E = 0$ $\theta = \theta_{eq}$	$\Delta E \gg -\Delta g^{ad}/F$ $\theta \ll 1$
$\Delta g^{ad} \gg 0$ (Au)	$\varsigma^{ex} - \varsigma^{ad}$	ς^{ex}	ς^{ex}
$\Delta g^{ad} \approx 0$ (Pt)	$\varsigma^{ex} - \varsigma^{ad}/2$	ς^{ex}	$\varsigma^{ex} + \varsigma^{ad}/2$
$\Delta g^{ad} \ll 0$ (Ni)	ς^{ex}	ς^{ex}	$\varsigma^{ex} + \varsigma^{ad}$

With attention to λ, the most important features in Fig. 5.2 d) are nearly constant values on either side of the potential of electrosorption or underpotential deposition, E^{ad}. Within a small potential interval around E^{ad}, the value of λ jumps by the amount ς^{ad}. When $|\varsigma^{ad}| > |\varsigma^{ex}|$, as in the example of the figure, this jump is accompanied by a change of sign in λ at a potential negative of E^{ad}. This also lets ι change sign, as is manifest in a cusp in the graph of Fig. 5.2 c) at the corresponding potential.

As can be seen in the compilation of limiting values, Table 5.1, the values of λ on each side of E^{ad} depend on the strength of adsorption. For the example of H on Au (weak adsorption), λ near equilibrium and at small magnitude of the overpotential is governed by the strain-dependence of the activation enthalpy, in other words, $\lambda \approx \varsigma^{ex}$. By contrast, $\lambda \approx \varsigma^{ex} - \varsigma^{ad}$ for Au at large and negative overpotential. If assuming that the two coupling coefficients ς^{ad} and ς^{ex} are of same sign and of not too dissimilar magnitude, then the net strain-dependence of

the reactivity is predicted strongest for electrodes with a negative adsorption enthalpy (as for Ni in the example of Table 5.1) and at positive overpotential and weakest for positive adsorption enthalpy (as for Au) and at negative overpotential.

5.1.4 Impact of H-H interaction on strain-dependent rate equation

As already pointed out in Ref. [93], the Langmuir isotherm is unrealistic inasmuch as it ignores the consequences of the adsorbate-adsorbate interaction. This is of relevance for the HER, since the hydrogen-hydrogen interaction energy, $\Delta h^{\text{a-a}}$, in the adsorbate layer is known to be important (see, *e.g.*, Ref. [125, 126]). The possible consequences for the strain-dependence are twofold. Firstly, the isotherm $\theta(E)$ will adopt a different functional form if $\Delta h^{\text{a-a}}$ takes on noticeable values. In view of Eq. (5.7), this will lead to a modified Tafel graph of the conventional, strain-free surface. Secondly, a strain-dependence of $\Delta h^{\text{a-a}}$ will need to be considered. There is no fundamental obstacle to introduce those generalizations into the rate equations and expressions for the reactivity-strain coupling such as Eq. (5.11). Yet, the task is complicated by the lack of realistic closed-form expressions for $\theta(E)$ allowing for adsorbate-adsorbate interaction. Now this section inspects the issue of that interaction with attention to the Heyrowsky reaction.

The energetics of interacting adsorbate molecules on a lattice with fixed number-density, Γ_0, of sites may be represented by a regular solution model [127] with the surface free energy function

$$\psi = \psi_0 + \Gamma_0 \left(\Delta g^{\text{ad}}\theta + \frac{1}{2}\Delta h^{\text{a-a}}\theta^2 + RT\left(\theta \ln \theta + (1-\theta)\ln(1-\theta)\right) \right), \qquad (5.20)$$

where ψ_0 is the free energy of the clean surface and $\Delta h^{\text{a-a}}$ denotes an adsorbate-adsorbate interaction energy. Equilibrium at the electrode requires (see, *e.g.*, Ref. [71])

$$\frac{1}{\Gamma_0}\frac{\partial \psi}{\partial \theta} = \mu - zF\Delta E \qquad (5.21)$$

with μ the chemical potential of the adsorbing ion, of valency z, in solution. For hydrogen (H) with Eq. (5.20), this equation (5.21) implies

$$-F\Delta E = \Delta g^{\text{ad}} + \Delta h^{\text{a-a}}\theta + RT \ln \frac{\theta}{1-\theta}. \qquad (5.22)$$

In the limit $\Delta h^{\text{a-a}} \to 0$ the equation (5.22) yields the conventional Langmuir isotherm as in Eq. (5.9). Repulsive adsorbate-adsorbate interaction ($\Delta h^{\text{a-a}} > 0$) may broaden the potential range of the transition from dilute to concentrated adsorbate at the effective electrosorption potential E^{ad}, whereas attractive interaction may, at sufficiently low temperature, lead to a surface miscibility gap and to the coexistence, at E^{ad}, of regions of dilute and concentrated adsorbate regions.

The general form of Eq. (5.22) with $\Delta h^{\text{a-a}} \neq 0$ is not readily inverted to obtain an analytical expression for the adsorption isotherm $\theta(\Delta E)$ applicable to the full range of coverage. However, the limiting behavior at high dilution ($\theta \ll 1$, $\Delta E - E^{\text{ad}} \ll RT$) and near saturation ($\theta \approx 1$, $E^{\text{ad}} - \Delta E \ll RT$) is readily seen to satisfy

$$\theta = \exp -\frac{\Delta g^{\text{ad}} + F\Delta E}{RT} \qquad (\theta \ll 1) \qquad (5.23)$$

and

$$\theta = 1 - \exp \frac{\Delta g^{\mathrm{ad}} + \Delta h^{\mathrm{a-a}} + F\Delta E}{RT} \qquad (\theta \approx 1), \tag{5.24}$$

respectively.

Allowing for strain-dependence of the interaction enthalpy via $\Delta h^{\mathrm{a-a}} = \Delta h_0^{\mathrm{a-a}} - F\varsigma^{\mathrm{a-a}}e$ and accounting for the definition of ς^{ad}, one readily obtains

$$\frac{\mathrm{d}\theta}{\mathrm{d}e}\Big|_{\Delta E} = \frac{F}{RT}\varsigma^{\mathrm{ad}}\theta \qquad (\theta \ll 1) \tag{5.25}$$

and

$$\frac{\mathrm{d}\theta}{\mathrm{d}e}\Big|_{\Delta E} = \frac{F}{RT}\left(\varsigma^{\mathrm{ad}} + \varsigma^{\mathrm{a-a}}\right)(1 - \theta) \qquad (\theta \approx 1). \tag{5.26}$$

With the above equations we may inspect the current-strain coupling, provided that both, the acting overpotential ΔE and the equilibrium potential E_{eq} of the reaction are sufficiently far from the electrosorption potential E^{ad} so that in each case one of the limits applies, dilute or concentrated adsorbate layer. While materials with E^{ad} close to E_{eq}, such as Pt, are excluded from this approximate analysis, useful conclusions are obtained for materials with weak or strong adsorption, such as the examples of Au and Ni in Table 5.1. The procedure is now exemplified for Au at large negative overpotential. By virtue of Eq. (5.15) for $j^{\mathrm{ex}\prime}$, and ignoring the inverse reaction rate (which is negligible at large negative overpotential), Eq. (5.11) evaluates to

$$\iota = \frac{F}{RT}j^{\mathrm{F}}\varsigma^{\mathrm{ex}} + j^{\mathrm{ex}}\frac{\theta\theta_{\mathrm{eq}}' - \theta_{\mathrm{eq}}\theta'}{\theta_{\mathrm{eq}}^2}\exp\left(\frac{-\alpha F\Delta E}{RT}\right). \tag{5.27}$$

Since $\theta_{\mathrm{eq}} \ll \theta$ while–by virtue of Eq. (5.26)–the derivative θ' becomes arbitrarily small at sufficiently negative ΔE, the term $\theta_{\mathrm{eq}}\theta'$ in the enumerator in the second summand can be dropped. Since weak adsorption implies that the coverage at the equilibrium potential is dilute, θ_{eq}' is given by Eq. (5.25). This leads to

$$\iota = \frac{F}{RT}j^{\mathrm{F}}\varsigma^{\mathrm{ex}} + \frac{F}{RT}j^{\mathrm{ex}}\varsigma^{\mathrm{ad}}\frac{\theta}{\theta_{\mathrm{eq}}}\exp\left(\frac{-\alpha F\Delta E}{RT}\right). \tag{5.28}$$

By comparing this result to Eq. (5.7) for j^{F}, one then obtains ι in the limit of large negative overpotential as

$$\iota \approx \frac{F}{RT}j^{\mathrm{F}}\left(\varsigma^{\mathrm{ex}} - \varsigma^{\mathrm{ad}}\right) \qquad (\theta_{\mathrm{eq}} \ll 1, \theta \approx 1), \tag{5.29}$$

which implies that $\lambda = \varsigma^{\mathrm{ex}} - \varsigma^{\mathrm{ad}}$, a result which agrees with Eq. 5.17 in Section 5.1.3 and Table 5.1. Other limiting cases are readily treated in an analogous way, and the results are compiled in Table 5.2.

With attention to the above result in Table 5.2 for the HER on Au at large forward bias ($\Delta E \ll 0$), it is remarkable that the results for the coupling strength is independent of $\varsigma^{\mathrm{a-a}}$, even though the adsorbate layer is here concentrated. The finding can be traced back to the very fact that the adsorbate layer is nearly saturated at large forward bias. Strain can then not noticeably affect the coverage, irrespective of its impact on the adsorbate-adsorbate interaction. The impact of strain on the reaction rate is therefore here a consequence of the variation of the normalization factors which, in Eq. (5.7), depend on θ_{eq}. This is a variation in a dilute adsorbate population, and is thereby independent of $\varsigma^{\mathrm{a-a}}$.

Table 5.2: Values of the reaction rate-strain coupling coefficient λ of the Heyrowsky reaction in various limiting cases. This table is similar to Table 5.1, except that an interacting adsorbate is considered. Symbols: E^{ad} - electrosorption potential, ΔE - overpotential, θ - adsorbate coverage. Electrocapillary coupling parameters for the activation barrier, for the hydrogen adsorption enthalpy, and for the hydrogen-hydrogen interaction enthalpy are denoted by ς^{ex}, ς^{ad} and $\varsigma^{\mathrm{a-a}}$, respectively. Non applicable combinations are denoted by "n. a.".

		$\Delta E \ll 0$		$\Delta E \gg 0$	
		$\Delta E \ll E^{\mathrm{ad}}$ $\theta \approx 1$	$\Delta E \gg E^{\mathrm{ad}}$ $\theta \ll 1$	$\Delta E \ll E^{\mathrm{ad}}$ $\theta \approx 1$	$\Delta E \gg E^{\mathrm{ad}}$ $\theta \ll 1$
$\Delta E^{\mathrm{ad}} \ll 0$ (Au)	$\theta_{\mathrm{eq}} \ll 1$	$\varsigma^{\mathrm{ex}} - \varsigma^{\mathrm{ad}}$	ς^{ex}	n. a.	ς^{ex}
$\Delta E^{\mathrm{ad}} \gg 0$ (Ni)	$\theta_{\mathrm{eq}} \approx 1$	ς^{ex}	n. a.	ς^{ex}	$\varsigma^{\mathrm{ex}} + \varsigma^{\mathrm{ad}} + \varsigma^{\mathrm{a-a}}$

It is shown that Eq. (5.11) can be evaluated in limiting cases where the adsorbate coverage at potential is either very dilute or very concentrated, and where one of those limits also applies at the equilibrium potential. This excludes the interesting case of the HER on Pt, but includes surfaces on which H adsorbs either very strongly or very weakly, and in particular Au surfaces. Here, the limiting behavior on either side of E^{ad} agrees with that of Table 5.1. As a central consequence of the derivation, the jump in λ around the electrosorption potential is thus expected even when the H-H interaction is strong. In other words, the H-H interaction on Au surfaces affects the reactivity, but its impact on the relative change of reactivity with strain is moderate. For surfaces with the strong H adsorption strength (as the example of Ni), a strain-dependent H-H interaction is predicted to change the reactivity-strain coupling at positive ΔE (hydrogen oxidation reaction), see Table 5.2.

Beyond replacing the Langmuir isotherm with a more realistic one that accounts for H-H interaction, generalizations of Parsons' rate equation, Eq. (5.7), may allow for the barrier energy and/or the symmetry factor α to depend on the coverage. This introduces additional coefficients which, themselves, may be strain-dependent. In the interest of conciseness, the present study aims to compare the simplest meaningful theory to experiment. In that spirit, the present study ignores these additional details.

The following section discusses an experimental approach which explores the mechanical modulation of electrocatalytic reactivity and compares first results to the theory.

5.2 Samples and characterization

The working electrodes under study were 50 nm thin gold or platinum films by sputtering deposition on polyimide substrates, $\approx$ 1 cm $\times$ 2 cm in size. The X-ray rocking curves of films prepared in this manner reveal a strong (111)-texture for Au and Pt, as shown in Fig. 5.3.

The HER in argon-purged 0.5M H_2SO_4 solution was studied on 111-textured thin films of gold and platinum, providing examples for weak (Au) and intermediate (Pt) hydrogen adsorption strength. Figure 5.4 shows cyclic voltammograms of the Au and Pt electrodes. The data is consistent with the clean surfaces of the polycrystalline, thin film metal electrodes [128, 129].
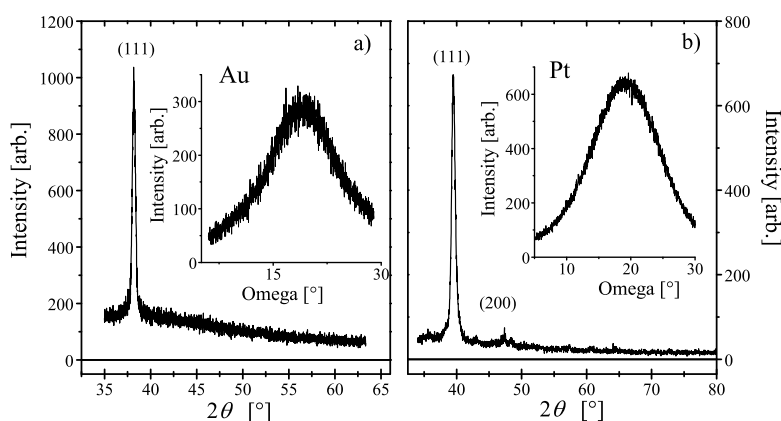
Figure 5.3: X-ray diffraction characterization of **a)** Au electrode and **b)** Pt electrode. Main graph: intensity *versus* scattering angle. Inset graph: rocking curve of intensity *versus* inclination angle for the (111) reflection.
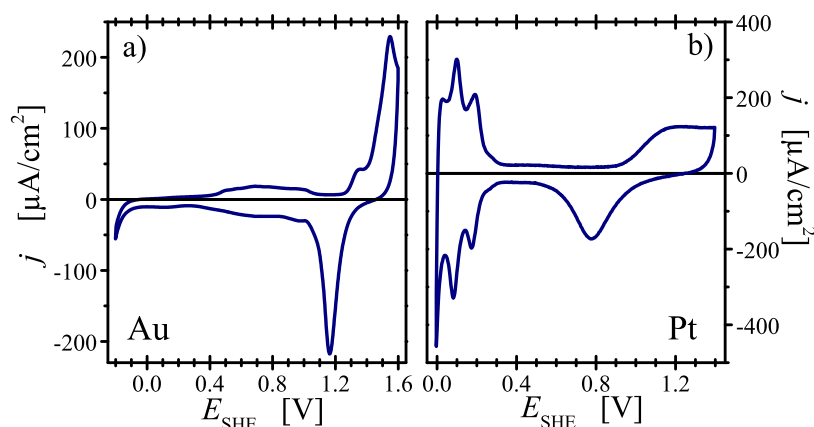
Figure 5.4: Cyclic voltammograms of current density, j, *versus* electrode potential, E, for **a)** Au and **b)** Pt thin film electrodes with a (111)-texture in 0.5 M H_2SO_4. Scan rate is 100 mV s^{-1}.

5.3 Impact of strain on hydrogen evolution reaction

The procedures of mechanical modulation of catalysis in this study are largely identical to Chapter 4 of DECMA on polarizable electrodes. The central differences are *i.*) the extension of the potential range to include the regime of hydrogen evolution and *ii.*) the focus on the Faraday current modulation. In the interest of a convenient description, a brief display of the procedures is presented here.

Using the strain as the reference signal, the in-phase (real) and out-of-phase (imaginary) components of the amplitude of potential or current modulation is detected by means of the lock-in amplifier. The potential-strain response, ς, is measured in potentiostatic mode during cyclic voltammetry as Fig. 4.5. The current modulation, ι, is measured from the potential drop over a shunt resistance in series with the counter electrode as Fig. 4.4. The real and imaginary

69

components of the modulation in potential or current, $\hat{E}$ or $\hat{I}$, are output data from the lock-in amplifier. With reference to Eqs. (5.1) and (5.6) the coupling coefficients were computed from the data as follows:

$$\varsigma = \hat{E}_{\text{real}}/\hat{e} \qquad (\text{constant } q), \qquad (5.30)$$

$$\iota = \hat{j}_{\text{real}}/\hat{e} = A^{-1}\hat{I}_{\text{real}}/\hat{e} \qquad (\text{constant } E), \qquad (5.31)$$

$$\lambda = \frac{RT}{F}\frac{\hat{I}_{\text{real}}}{I\,\hat{e}} \qquad (\text{constant } E), \qquad (5.32)$$

where I denotes the net current as measured by the potentiostat and A is the area wetted by the meniscus.

Electrochemical impedance spectroscopy (EIS) used a voltage perturbation in root mean square of 10 mV. The uncompensated solution resistance, R_{U}, was measured immediately after cyclic strain experiments using EIS in the frequency range 0.01 Hz - 1 kHz and identifying the real part of the impedance in its high-frequency limit with R_{U}. A typical value was $R_{\text{U}} = 18\ \Omega$. All electrode potentials shown here are corrected for the potential drop in solution by subtracting $I(E)R_{\text{U}}$ from the nominal electrode potential value.

Tafel plots were recorded at a scan rate 2 mV s^{-1}, using the cyclic voltammetry staircase option with 3 mV potential step to eliminate the capacitive contribution. Decohesion of the metal films at large and negative potentials limited the lower vertex potentials. These were chosen so as to allow several consecutive experiments with any one sample.

Since the present DECMA setup prevents the use of a rotating disk anode, transport limitations may affect the results. While acidic solutions provide an abundant supply of protons as the reactants of the HER, accumulation of the product species molecular hydrogen in a layer of electrolyte near the electrode surface may retard the reaction, as may the bubble formation that has been observed for Pt at large negative overpotential [91]. Therefore, the present HER measurements typically used negative-going scans in order to minimize the accumulation of H$_2$ in solution. The small j^{ex} on Au implies in particular that the above-mentioned kinetic limitations are benign when working with Au electrodes in acidic solution [122].

Figure 5.5 displays the results for the HER. The DECMA data for Au on HER is first discussed.

5.3.1 Gold electrode

Figure 5.5 a) shows a Tafel plot for the gold electrode. Under forward bias ($\Delta E < 0$), two well-defined Tafel slopes are apparent, -79 mV dec^{-1} at low overpotential magnitude ($|\Delta E|$) and -224 mV dec^{-1} at higher $|\Delta E|$. From the intersection of straight lines of best fit, the transition is found at $\Delta E = -0.31$ V. By extrapolating the data at low $|\Delta E|$ to the equilibrium potential, the exchange current density is estimated at $j^{\text{ex}} \approx 0.08\ \mu\text{A cm}^{-2}$. In view of Fig. 5.2 the break in the Tafel graph is consistent with the signature of H electrosorption in the Heyrowsky kinetics, suggesting that for H on Au $\Delta E^{\text{ad}} \approx -0.31$ V.

As outlined in the theory section at the onset of this chapter, the analysis of DECMA data requires the separation of capacitive and Faraday effects. It was found useful to inspect electrochemical impedance data. Figure 5.5 c) shows the impedance, $\mathbf{Z}$, measured at the frequencies, 20 and 70 Hz, with the same as in the DECMA experiment. The key observation is a transition
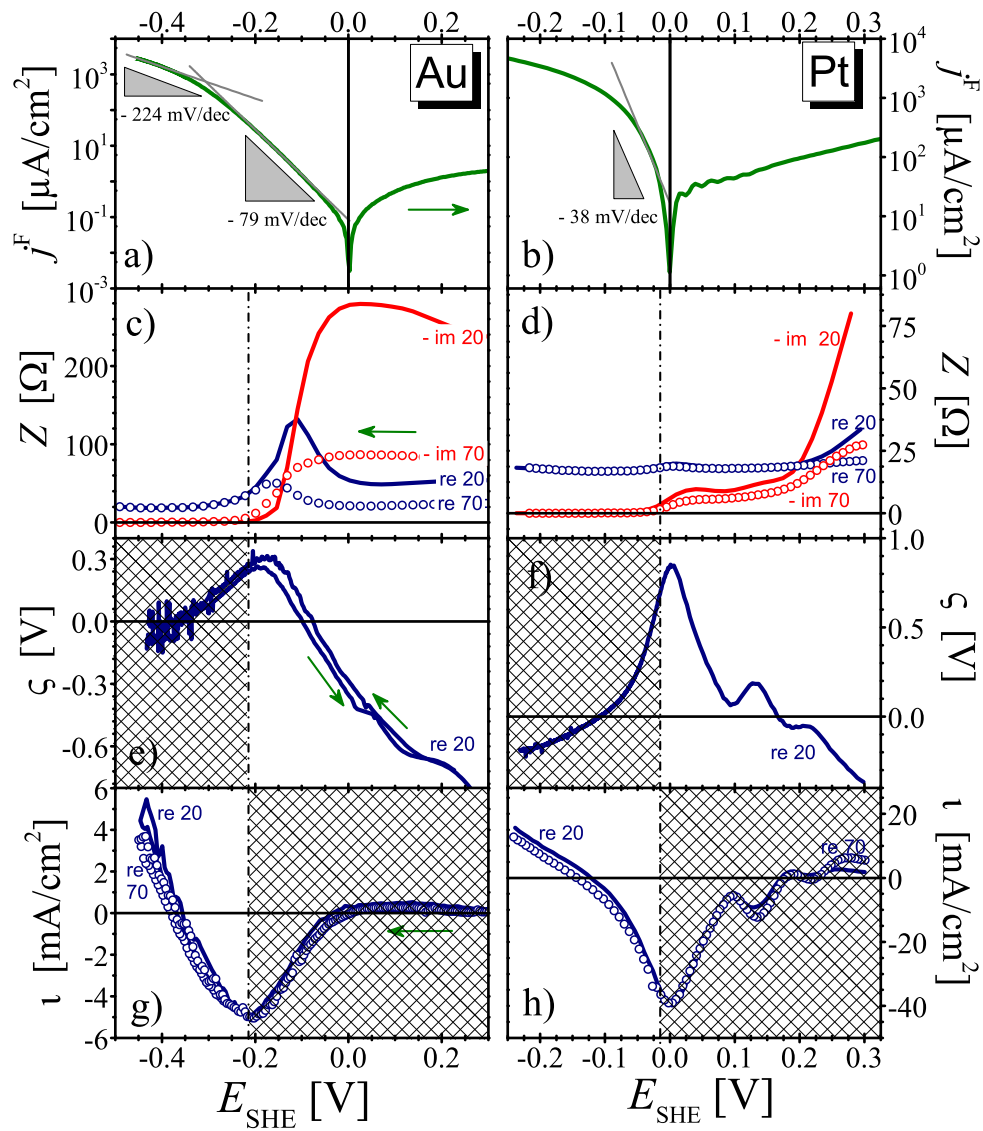
Figure 5.5: Electro-chemo-mechanical characterization of Au (left column) and Pt (right column) electrodes in 0.5 M H_2SO_4. **a,b)** Tafel plots of current density, j^F, *versus* electrode potential, E, during scans at 2 mV s^{-1}. Thin green solid lines are straight-line fits in regions of linear response in the log-linear representation. **c,d)** Real and imaginary parts of the impedance, **Z**, *versus* E at frequencies of 20 and 70 Hz, as indicated by labels. Vertical dash-dotted line marks transition between dominantly capacitive and dominantly Faraday currents. **e,f)** Electrocapillary coupling parameter ς at strain frequency 20 Hz and at 20 mV s^{-1} scan rate. **g,h)** Current-strain response parameter $\iota = dj/de$ recorded at 20 Hz (lines) and 70 Hz (circles) with 20 mV s^{-1} scan rate. Shaded regions mark potential regime were the respective technique is inappropriate since the requirements of dominantly capacitive (for ς) or dominantly Faraday (for ι) processes are violated.

at $E \approx -0.2$ V (dash-dotted vertical line in the left column of Fig. 5.5): When E is reduced below that value, the imaginary part of **Z** vanishes and the data of real part loses its frequency dependence. Both aspects are signatures of the transition from a regime of dominantly capacitive processes for $E \gtrsim -0.2$V to dominantly Faraday behavior for $E \lesssim -0.2$ V. This implies that DECMA data recorded for E below -0.2 V is dominated by the response of the HER rate to strain, whereas the DECMA data at the more positive E is dominated by capacitive processes. Shaded regions in the graphs of Fig. 5.5 mark the potential regimes where the respective technique is inappropriate since the requirements of dominantly capacitive (for ς) or dominantly Faraday (for ι) processes are violated.

Results for the potential-strain response near equilibrium, as represented by the electrocapillary coupling parameter ς, are plotted in Fig. 5.5 e). The finding of a negative value of ς at the more positive potentials agrees with results of Chapter 4 in study of ς on Au in the vicinity of its *pzc*. As the hydrogen electrosorption potential is approached, ς changes to positive. The value of ς reaches a maximum value of $+0.3$ V, right before the entry into the regime of dominantly Faraday behavior where the discharge of the interface by the reaction current prevents further measurement of ς by the present approach.
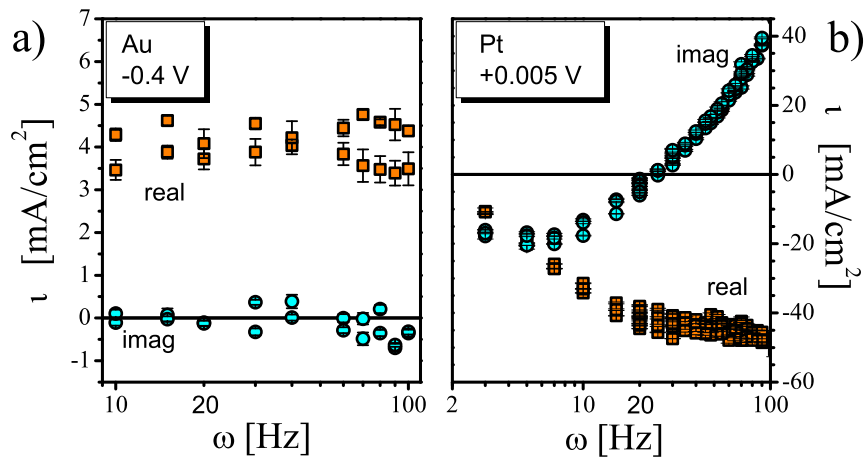
Figure 5.6: Real and imaginary parts of the current-strain response parameter ι of Au and Pt electrodes *versus* the strain frequency ω. Potential values are indicated in the legends. Data for Au is in the Faraday regime, with vanishing imaginary part. For Pt, data in the capacitive regime reveals mixed (real/imaginary) behavior at elevated frequencies, consistent with results of the electrochemical impedance spectroscopy.

Figure 5.5 g) displays the results for the current-strain coupling coefficient ι for frequencies of 20 and 70 Hz. The frequency dependence of the current-strain response of Au has been recorded at $E = -0.40$ V in more detail, see Fig. 5.6 a). In agreement with Eq. (5.6), the real part of the current modulation signal - which measures ι - is independent of the strain frequency. This supports the identification of that signal with the response of Faraday current to the cyclic strain. In particular, the real part of the current-strain response in Fig. 5.5 g) can be identified with the Faraday current modulation when $E \lesssim -0.2$ V. The data shows the parameter ι as positive-valued at the lowest end of the potential range under study. Since the net Faraday

current is negative here, the positive sign of ι implies that tensile (positive) strain inhibits the reaction. It is seen that ι decreases with increasing potential, changing sign at $E \sim -0.38$ V and then leveling off. The decrease in magnitude of the current-strain response at even more positive potential E ($\gtrsim -0.2$ V) reflects capacitive behavior and so cannot be discussed as a signature of ι.
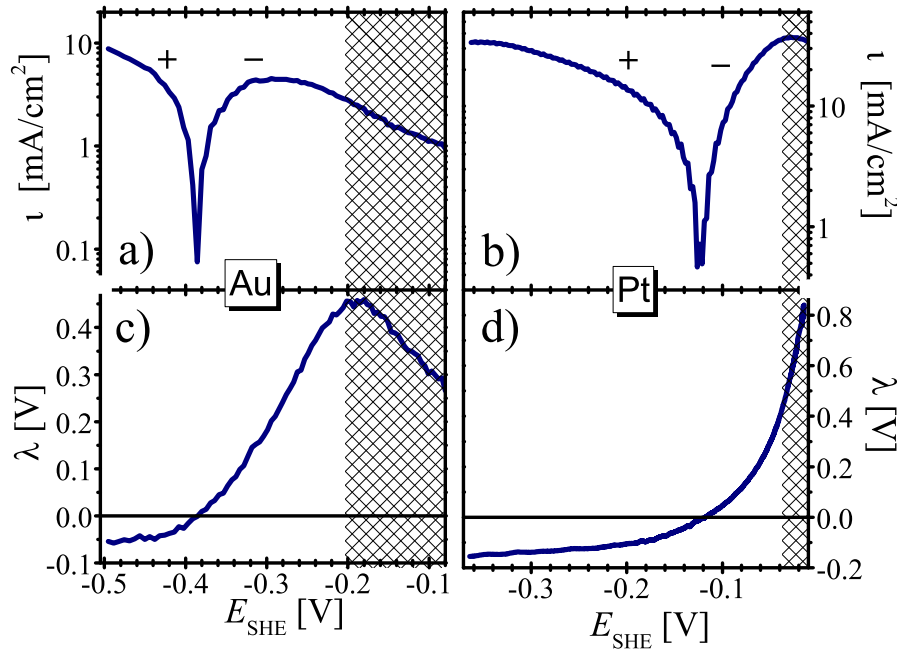

Figure 5.7: Current-strain response parameters $\iota = \mathrm{d}j/\mathrm{d}e$ (**a,b**)) and $\lambda = (RT/F)\mathrm{d}\ln j^{\mathrm{F}}/\mathrm{d}e$ (**c,d**)) of Au and Pt as measured during negative-going potential scans at 2 mV s^{-1}. Shaded regions mark potential regime were capacitive processes dominate, preventing valid measurements of ι and λ.

Figures 5.7 a) and c) show results of an experiment in the HER regime, focusing on the two current-strain response parameters, ι and λ and using a slower potential scan rate (2 mV/s as compared to 20 mV/s in Fig. 5.5) and a slightly extended potential range for closer inspection of the current-strain coupling. As above, the shaded regions in Fig. 5.7 mark potentials in which capacitive processes mask the Faraday-current strain response. The agreement of the experiment with the theory is apparent when the log-linear plot of ι versus E in Fig. 5.7 is compared to the schematic graph of the theory prediction in Fig. 5.2 c). The key observation is that the response parameters change sign near $E = -0.38$ V, slightly negative of E^{ad}. This manifests itself in the graph of $\log \iota$ by the prominently cusp at -0.38 V. In other words, at lesser overpotential magnitude the tensile strain acts to *enhance* the reaction current (more negative current), whereas at higher overpotential magnitude (more negative E) tensile strain *inhibits* the reaction.

It is also remarkable that the parameter λ levels off in the most negative potential range, approximating a constant value $\lambda \sim -0.05$ V. At higher potential λ increases, reaching the maximum value $\lambda \sim +0.45$ V at the entry into the capacitive regime.

5.3.2 Platinum electrode

The Tafel plot of Pt electrode, Fig. 5.5 b), is curved in the entire potential range under investigation. This is consistent with previous observations of Refs. [79, 91, 120]. In series of consecutive scans with the same electrode, this thesis obtains highly reproducible results, as shown in Fig. 5.8. This confirms the curvature as an inherent feature of the kinetics and not a signature of electrode degradation. An estimate of Tafel slope, -38 mVdec^{-1}, is obtained at low overpotential from a straight-line fit to the data for -0.05 V $\leq \Delta E \leq -0.015$ V. The value of Tafel slope is also in agreement with previous results [79, 120, 130].
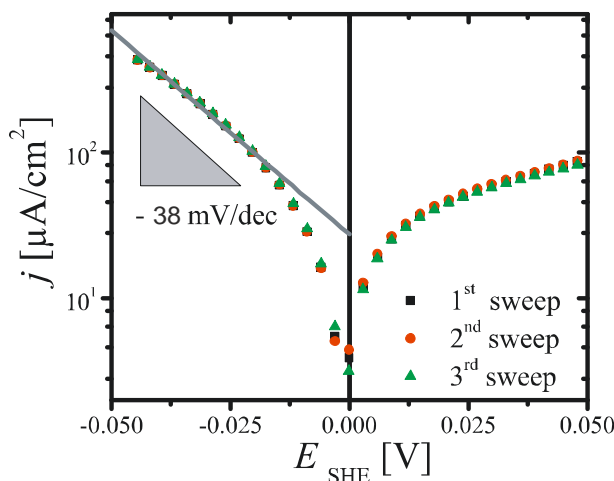

Figure 5.8: The reproducible results of Tafel plots of Pt electrode in 0.5 M H$_2$SO$_4$ in series of consecutive scans at a rate of 2 mV s^{-1}. The Tafel slope, -38 mVdec^{-1}, is obtained at low overpotential.

The EIS data of Fig. 5.5 d) show the imaginary part vanishing for $E \lesssim$ -0.03 V, indicating that Faraday behavior dominates in that regime, whereas pseudo-capacitive processes are dominant at the higher potentials. This notion is confirmed by the current-strain response data of Fig. 5.5 h). The Faraday current must vanish at equilibrium, irrespective of the strain, implying $\iota = 0$ at $\Delta E = 0$. Yet, the experimental current modulation does not vanish there. In fact, the graph of the current-strain modulation exhibits an extremum at a potential only slightly positive. This agrees with a capacitive rather than Faraday process dominating the response at and above $E = 0$.

The first and second UPD peaks, at $E = 0.174$ V and 0.083 V in the CVs of Fig. 5.4 b), coincide with minima in the potential-strain response, Fig. 5.5 f). The observed shifts of phase and sign are in agreement with those of Eqs. (5.1) and (5.6), confirming that the experiment here measures the values of ς of the corresponding electrosorption processes as in Chapter 4.

The graph of current-strain response for Pt in Fig. 5.5 h) is remarkably similar to that for Au (Fig. 5.5 g) above), with an extremum at potentials positive of the H electrosorption potential and a sign inversion at potentials negative thereof, here at ~ -0.13 V. Most notably, the sign inversion – reflected by the prominent cusps in Fig. 5.7 a) for Au and Fig. 5.7 b) for Pt – is common to both metals. For Pt, as for Au, tensile strain accelerates the reaction ($\iota < 0$) at lesser

overpotentials, whereas the trend is reversed at the higher overpotentials, where tensile strain inhibits the reaction ($\iota > 0$).

Based on the electrochemical impedance data of Fig. 5.5 d), the signals at potentials positive of -0.03 V have been identified as the signatures of capacitive processes. Yet, the lack of a noticeable frequency dependence in the current-strain response data of Fig. 5.5 h) seems to disagree with this notion. The frequency dependence of the current-strain response of Pt has therefore been inspected on in more detail, see Fig. 5.6 b). It can be seen that the real part of the current-strain response is only frequency-independent in the regime of $\omega \gtrsim 20$Hz. At lesser frequencies, the real part does depend on ω. Furthermore, the imaginary part is strongly frequency dependent throughout the entire frequency range under investigation. This behavior is indeed compatible with capacitive processes and not with Faraday behavior.

As for Au, the present work have studied the current-strain response for Pt in more detail at slower scan rate. The results, Fig. 5.7 b) and d), confirm the above observations. At the most negative E, the results for λ in Fig. 5.7 d) show only slow variation with potential, with a smallest value of $\lambda = -0.175$ V.

5.4 Discussion
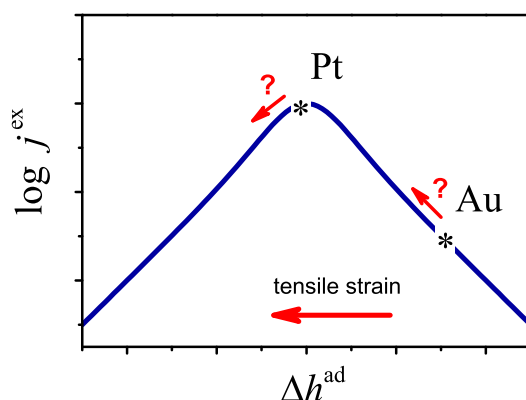
Figure 5.9: Schematic representation of the position of Pt and Au on the volcano curve of exchange current density j^{ex} *versus* H enthalpy of adsorption, Δh^{ad}, for the hydrogen evolution reaction. Tensile strain makes the surface more binding for H (large arrow), which might suggest that the reactivity of Au increases while that of Pt decreases (small arrows).

The Au and Pt electrodes of the experiment probe the HER on substrates with quite different adsorption strength. Pt undergoes UPD at slightly positive overpotentials ($\Delta h^{\text{ad}} \lesssim 0$), which puts it near to (but slightly to the left of) the peak of the volcano curve, Fig. 5.9, of exchange current density *versus* hydrogen enthalpy of adsorption. By contrast, gold metal lies the left hand side of the volcano curve with a very positive Δh^{ad} [28, 122].

In several respects, the HER on Pt is less suited for a discussion in terms of idealized models than the HER on Au. In view of the high reactivity of the Pt surface, accumulation of dissolved H_2 in the electrolyte [91] likely inhibits the reaction at more negative overpotentials. The impact

of such kinetic limitations may be mitigated by focusing on the coupling parameter λ, which is defined as the *relative* change of the current in response to strain. Since kinetic limitations act on j^F as well as δj^F, their impact is partly canceled when evaluating $\delta j^F / j^F$. In this sense, λ is an inherently robust parameter even when the current is affected by the solution resistance due to the accumulation of dissolved H_2 in the electrolyte.

Irrespective of that issue, the curved Tafel plot for Pt, which is found even when transport limitations are removed by using a rotating disk electrode [77, 91, 131], is ill consistent with simple models for the kinetics. In fact, a transition between Tafel kinetics at low overpotential and Heyrowsky kinetics at high (negative) overpotential has been suggested for Pt [77, 124]. Furthermore, Pt presents the additional challenge that the strong capacitive signals of hydrogen UPD nearly coincide with the equilibrium of the HER, complicating the separation of the modulated Faraday current.

As a consequence of the more challenging nature of the Pt case, the discussion of this first study focuses on the findings for Au, inspecting the Pt results in the spirit of a qualitative comparison only.

5.4.1   Electrosorption potential and Tafel slope

The present experiments for gold indicate Tafel slopes of -79 mV dec^{-1} at low overpotential magnitude ($|\Delta E|$) and -224 mV dec^{-1} at higher $|\Delta E|$, with a break at around $E = -0.31$ V and an exchange current density $j^{ex} \approx 0.08\ \mu A\ cm^{-2}$. These values will now be discussed in relation to the literature.

For the idealized case of symmetry factor $\alpha = {}^1/_2$, the Tafel slopes of the Heyrowsky reaction of Eq. (5.7) with a Langmuir isotherm, which underlies the discussion of the Au data, correspond to $d \ln j^{ex}/dE = -3F/(2RT)$ or -40 mV dec^{-1} and $-F/(2RT)$ or -119 mV dec^{-1} at low and high overpotential magnitudes, respectively. Previous experimental studies of the HER on polycrystalline gold, using rotating disk electrodes, indeed find Tafel slopes that support the model, namely -48 ± 12 mV dec^{-1} and -110 ± 11 mV dec^{-1} at low and high overpotential, respectively [84, 130]. The experiment, in this chapter, finds a factor three difference between the slopes in the respective regimes, which also agrees with the model. Yet, the absolute values of the present experimental Tafel slopes are here consistently higher than the prediction. That observation is consistent with published data, which show Tafel slopes (at low overpotential) of -73 ± 20 mV dec^{-1} for Au electrodes in acidic solution [82, 83, 120, 132] when no rotating disk electrode is used. This implies that the deviation between the model Tafel slopes and the present experiment is a signature of transport limitations. The findings in this chapter are otherwise consistent with the intrinsic behavior of the HER on clean polycrystalline Au surfaces.

The change in Tafel slope is an inherent feature of the Heyrowsky kinetics, where it demarcates the transition between dilute and concentrated hydrogen coverage at the electrosorption potential, $E^{ad} = -\Delta g^{ad}/F$. The observation here of the Tafel break at $\sim E = -0.31$ V suggests that the free energy of hydrogen adsorption on Au is $\Delta g^{ad} = +0.31$ eV or +29 kJ mol^{-1}. *Ab initio* computations for H on Au(111) put Δg^{ad} at +0.45 eV [28] and +0.41 eV [133]. Furthermore, Δg^{ad} reflects the metal-hydrogen bond strength, which for Au has been reported 0.50 eV more positive than for Pt metal [19]. This latter value would suggest that $E^{ad} \approx$ -0.3 to -0.4 V for Au in view of the H UPD signatures on Pt at +0.1 to +0.2 V, see Fig. 5.4. It is seen that the observed potential of -0.31 eV puts the Tafel break in our data within the interval of reported

values for the electrosorption potential of H. Furthermore, the exchange current density for the Au electrode in the present experiment, $j^{\mathrm{ex}} \approx 0.08$ μA cm^{-2}, agrees well with the published values 0.08 μA cm^{-2} in Ref. [97] and 0.12 μA cm^{-2} in Ref. [122].

To summarize these observations, the results here overestimate the Tafel slopes, but provide values for the apparent adsorption potential E^{ad} and for the exchange current density j^{ex} that are consistent with previous reports. This thesis attributes the deviation in Tafel slope to transport limitations, but conclude from the agreement of E^{ad} and j^{ex} that the impact of the solution resistance is limited and that the data here for Au give a reasonable qualitative representation of the inherent kinetics of the reaction.

As motivated above, this chapter refrains from discussing the Pt data in detail. However, it is recalled that the qualitative behavior of $\iota(E)$ of Pt is found similar to Au. This lends qualitative support to the present discussion of the impact of strain on the reactivity at Au surface.

5.4.2 Potential-strain response

As argued in Result Section, the experimental data for potential- and current modulation with strain for both electrodes are consistent with a transition between dominantly capacitive or pseudo-capacitive behavior at the more positive potentials and dominantly Faraday behavior at more negative potential. The respective regimes allow, exclusively, the measurement of the potential-strain response at constant charge (pseudo-capacitive processes) and of the current-strain response at constant potential (Faraday processes).

Chapter 4 has found that $\varsigma < 0$ for capacitive processes with little chemisorption on transition and noble metal surfaces and specifically on Au, which is also consistent with Refs. [37, 38, 48, 54, 101, 134]. This is born out by the present results at the most positive potentials. During negative-going scans, as the potential approaches E^{ad}, pseudo-capacitive adsorption of H will become more important and eventually dominate the potential-charge and potential-strain response. In view of the definition of ς^{ad}, Eq. (5.12), the experimental potential-strain response parameter will then gradually change; when chemisorption dominates the response will eventually take on the value of ς^{ad} [32]. In view of the change of sign in ς and its continuing increase upon decreasing the potential (Fig. 5.5e), this chapter therefore concludes that ς^{ad} of H on Au is positive valued with a lower bound of +0.3 V. The finding for Au is consistent with positive values of ς during hydrogen electrosorption experiments on Pd [32, 103] and Pt [32, 101]. The positive ς^{ad} imply that tensile strain makes the metal surfaces more binding for hydrogen. This experimental finding is consistent with the predictions of the d-band model, which quite generally implies an enhanced binding on laterally expanded surfaces [24, 26, 29].

5.4.3 Current-strain response

For the current-strain response the experimental results here indicate that the graphs of $\lambda(E)$ for both, Pt and Au, agree well with the theoretical model in Section 5.1, specifically inasmuch as *i*.) both surfaces display the change of sign in $\lambda(E)$; *ii*.) $\lambda(E)$ becomes approximately constant in the limit of large negative overpotential; and *iii*.) the change in sign is at a potential negative of the break in the Tafel plot that may be linked to E^{ad}. This thesis takes these observation as a confirmation of the concept of a strain-dependent Heyrowsky or Tafel kinetics, as explored by the model. Details will now be addressed.

The central finding for current-strain response on Au is that λ changes sign at $E \approx -0.38$ V near E^{ad}. As was pointed out above, the negative value of λ at lesser $|\Delta E|$ implies that tensile strain here enhances the reactivity, whereas $\lambda > 0$ at higher $|\Delta E|$ means that tensile strain here diminishes the reactivity. The same qualitative behavior is found for Pt, except that the change in sign of λ here occurs much closer to the equilibrium potential of the HER.

Upon comparing Figs. 5.2 and 5.7 it is seen that the graphs of ι and λ in theory and experiment agree well if, for Au, the model takes ς^{ex} of same sign as and moderately lesser magnitude than ς^{ad}. In view of Table 5.1, the constant value of $\lambda \approx -0.05$ V at the lowest negative overpotential implies that $\varsigma^{\text{ex}} - \varsigma^{\text{ad}} \approx -0.05$ V. The current-strain coupling reaches a maximum value of $\lambda = +0.45$ V at the transition between capacitive and Faraday behavior, implying $\varsigma^{\text{ex}} \geq +0.45$ V and, therefore, $\varsigma^{\text{ad}} \geq +0.50$ V. This is also consistent with the finding for the potential-strain coupling, which tends to increase with decreasing potential, reaching a maximum value $\varsigma = +0.3$ V before the transition to Faraday behavior prevents further observation with the present technique.

It is of interest to inspect the observation of $|\varsigma^{\text{ad}}| \gtrsim |\varsigma^{\text{ex}}|$ in the light of the Brønsted-Evans-Polanyi relation, which links the enthalpies of adsorption to the enthalpies of the transition states [27, 135–137]. DFT data for adsorption on different substrates reveal a scaling factor, connecting Δh^{ex} to Δh^{ad}, near to but slightly less than unity [137]. This is compatible with present observation for surfaces under different states of strain. However, the theory also highlights counter examples: For CO on Ru (0001), the dissociation barrier is more strongly strain-dependent than the adsorption enthalpy [26]. Furthermore, a study of the energies of intermediates in methanol oxidation over strained copper surfaces [29] finds no clear trends for the variation of reaction barriers with strain. The quite different findings for the individual processes highlight the need for approaches–such as the present one–affording a separation of the two enthalpy-strain coupling coefficients in experiment.

Inasmuch as the results for Pt provide a qualitative description of the current-strain coupling, it is concluded that the reactivity at finite overpotential here also decreases with tensile strain. The apparent change in sign of λ, quite close to the transition to capacitive behavior, suggests that the exchange current density as defined through Eq. (5.7) shows the opposite trend, with enhanced current under strain in tension. Note, however, that empirical values for j^{ex} are typically derived by extrapolation from currents at finite overpotential to $\Delta E = 0$. The j^{ex} measured in this way depends on strain through the current in the regime where λ may be negative. Since the strain dependence of the 'empirical' HER exchange current on Pt is governed by λ at finite overpotential, and since the corresponding reaction may be inhibited by tensile strain, the strain-induced variation of the empirical exchange current may be of different sign compared to the variation of the j^{ex} of Eq. (5.7).

At first sight, the observations that tensile strain inhibits the reactivity of both, Au and Pt under forward bias are not immediately obvious if one considers the volcano curve (Fig. 5.9) for the reactivity - as represented by the exchange current density - of metal surface for the HER. Since tensile strain makes the surface more binding for H, it shifts both Au and Pt to lesser Δh^{ad} on the graph. With Au on the descending branch of the volcano and Pt near to its top, a finite tensile strain would make Au more reactive and Pt less reactive, contrary to the observation. The apparent discrepancy is related to the different strain-dependence of two measures for the reactivity, namely the exchange current density of j^{ex} of Eq. (5.7) on the one hand and the Faraday current at finite overpotential on the other. The present discussion of the

results for Au indicates that the exchange current density is indeed enhanced by tensile strain since, at $\Delta E = 0$, the theory implies $\lambda \approx \varsigma^{ex}$, which is positive. Yet, significant current can only be obtained at higher overpotential, where the hydrogen coverage has changed from dilute to concentrated. Here, the theory indicates $\lambda \approx \varsigma^{ex} - \varsigma^{ad}$, which takes on negative values.

5.5 Conclusion

In the study of this chapter, the consequences of elastic strain of an electrode have been inspected on its electrocatalytic activity for the hydrogen evolution reaction. The present approach is motivated by the data from theory and experiment that establish the enthalpies of adsorbates and of transition states as significantly strain-dependent.

The key findings here are: *i.*) successfully separation of the modulated pseudo-capacitive current and Faraday current in current-strain response measurement; *ii.*) the feasibility of an *in situ* measurement of the mechanical modulation of the electrocatalytic reactivity during potential scans; *iii.*) an inversion in sign – supported by experiment and theory – in the reactivity-strain coupling strength at a potential somewhat negative of electrosorption; and *iv.*) the experimental verification of assumptions that strain-dependent adsorption enthalpy and strain-dependent activation enthalpy in hydrogen evolution reaction.

Starting out with the kinetic rate equation for the Heyrowsky or Tafel reactions with Langmuir sorption characteristics, this chapter introduces separate coupling coefficients, ς^{ad} and ς^{ex}, respectively, for the strain dependence of the adsorption enthalpy of H and for the activation energy.

The relative change of the Faraday current in response to strain can be quantified by the parameter λ, which emerges as a weighted sum of the two coupling coefficients. The weighting factors depend on the overpotential, ΔE. Near equilibrium ($\Delta E = 0$) it is found $\lambda = \varsigma^{ex}$, so that the current modulation is entirely governed by the strain dependence of the transition state energy. By contrast, the reactivity at higher overpotential can also reflect the strain-dependence of the adsorption enthalpy as measured by ς^{ad}. The coupling far from equilibrium depends on the sign of ΔE and on the strength of H adsorption. The present study of the HER on Au electrodes indicates that ς^{ad} and ς^{ex} are of identical sign, with a larger magnitude for ς^{ad}.

These experiments under study explore an approach towards monitoring the mechanical modulation of electrocatalytic reactions by using a small cyclic strain of the electrode and a lock-in technique to detect the ensuing modulation of the reaction current. This cyclic strain can be applied and the current modulation analyzed simultaneously with the potential scan which is used to obtain the data for a Tafel plot. While the absence of forced liquid flow - as in a rotating disk experiment - impairs the results in the present implementation, meaningful data was obtained for the exchange current density and the electrosorption potential of the HER on Au.

In the experiment, the variation of the reactivity-strain coupling (λ) with overpotential (ΔE) exhibits qualitatively similar behavior for Au and Pt. The most prominent observation is a change of sign of $\lambda < 0$. The transition is consistent with our theory. With $\lambda < 0$ at large and negative overpotential (*i.e.*, forward bias of the HER) and a transition to $\lambda > 0$ when ΔE is increased near the H electrosorption potential, for Au as well as Pt, present work finds that tensile strain reduces the reactivity under sufficiently large forward bias, and a transition to

tensile strain enhancing the reactivity under lesser bias.

By contrast, the two metals may differ in respect to the impact of strain on the exchange current density: while j^{ex} of Au increases under tensile strain, the data are at least compatible with an empirical exchange current density j^{ex} of Pt decreasing. The strain-dependence of j^{ex} is in agreement with expectation based on the position of the two elements on the volcano curve of j^{ex} *versus* H adsorption enthalpy. Yet, the different behavior of the reactivity under finite bias shows that the strain effect on the reaction kinetics is governed by additional factors, which are not appropriately measured by the exchange current alone.

Chapter 6

Summary and Outlook

The contribution of this dissertation to the material science is the successfully experimental investigation of the link between surface mechanical deformation and electrode processes. Imposing a cyclic strain on the electrode surface is so as to tune the lattice parameter of surface material, and then the response variations of relevant parameters of interest (*e.g.* potential and current) were precisely measured by the lock-in technique of dynamic electro-chemo-mechanical analysis (DECMA). This thesis thereby established the foundation of measuring the variations of the electrode potential and the current in response to the surface strain under the condition of controlled potentials. The data obtained relate to several electrochemical processes, full covering with the regions of the capacitive charging near the potential of zero charge (pzc), the electrosorption processes as well as the electrochemical reaction. Several original phenomenons were first observed and discussed for different electrochemical systems (*e.g.* different concentration of electrolytes and different transition nobel metals).

The most important conclusions of this thesis are summarized as following:

Coupling coefficient of electrode potential and strain

i) Verification of DECMA at equilibrium condition

The measurement strategies were successfully established as the first achievement of this dissertation. These strategies were validated by three independent different experimental methods. All results of methods were in perfect agreement with narrow margins throughout the entire potential range in study. Such agreement gave a strong indication that the experiments provided valid data for the quantity of the electrocapillary parameter of interest, $\varsigma_E = dE/de|_q$, the response of electrode potential to the strain at constant (Lagrangian) charge density condition.

The coupling coefficient ς_E was found strongly dependent on the electrode potential when studying 111-textured gold electrode as an example. The sign of coefficient was always negative in the capacitive process at a clean surface of gold electrode. The third finding was that ς_E had an extremum value, -1.9±0.2 V, in the $HClO_4$ dilute solution.

ii) Comparison between polarisable and nonpolarisable electrodes

The comparative experiments clarified the confusion of difference between the potential-strain response of polarisable (PE) and nonpolarisable (NPE) electrodes. The respective response

parameters were under separate condition: at constant charge density, q, for the PE ($dE/de|_q$) and at constant chemical potential of the metal atom, μ, for the NPE ($dE/de|_\mu$). These two parameters were thereby linked to variations of the chemical potential of the electron (PE) and of the metal atom (NPE), respectively. The present experimental results confirmed that: **a)** $dE/de|_\mu$ of the NPE was small and the magnitude of $dE/de|_\mu$ was about two orders less than the magnitude of $dE/de|_q$; **b)** ς_E of Ag near the *pzc* was negative valued, similar to Au electrode.

iii) Application of DECMA to different concentration

As a case-study, the method of measuring ς_E was applied to gold electrodes in $HClO_4$ and H_2SO_4 of different concentrations. The finding, that ς_E was essentially independent of the ion and of the solution concentration, appeared to link ς_E exclusively to the behavior of the metal surface. The most obvious observation was a peak in the magnitude of ς_E at a potential, which was suggested coinciding with the *pzc*. Then the extremum of $\varsigma_E(E)$ would provide a useful probe of the *pzc* of gold electrodes, which could be applied in general in electrochemical studies.

iv) Application of DECMA to electrosorption processes

The behavior of ς_E was studied in a wider potential range, which included the specific electrosorption on transition metals (Au, Pt and Pd). The sign of ς_E changed at different electrode states, *e.g.* hydrogen/oxgen electrosorption and clean/oxygen-covered surface . The positive valued ς_E during the hydrogen electrosorption gave a understanding that a tensile strain made the metal surface more binding for H on these metals. In fact, this is the first quantifiable measurement and report of ς_E for hydrogen adsorption on gold. This is indeed difficult to measure by other techniques, since the large Faraday current of the hydrogen evolution reaction hides the signal in conventional electrochemical measurement techniques.

At the onset of oxygen specific adsorption region, the negative valued ς_E for Au, Pd and Pt metals implies that the tensile strain enhances the adsorption of O or OH species. The present study found that the ς_E kept negative during whole oxygen adsorption process on Au electrode. Contrary to the Au metal, ς_E changed its sign to positive during oxygen species adsorption for Pd and Pt metals. This observation connected to the formation of an oxide monolayer on Pd and Pt but not on Au surface. The above findings underline that DECMA could provide attractive insights into electrode processes and could be used as a sensitive tool for characterizing adsorbate coverage.

Faraday current-strain coupling on hydrogen evolution reaction

i) Theoretical model of strain-dependent reaction rate

The focus of this thesis is on the investigation of the strain-dependence of electrocatalysis. A theoretical model was accordingly explored to the realm of electrocatalytic reaction. In short words, the model first introduced the strain-dependent term into the kinetic rate equations for strain surfaces, and derived results for the variation of coupling strength with the electrode state. The hydrogen evolution reaction (HER) was under study as a simple model process.

The model started out with the kinetic rate equations of the Heyrowsky ($H_{aq}^+ + H_{ad} + e^- \rightleftharpoons H_2$) and the Tafel ($H_{ad} + H_{ad} \rightleftharpoons H_2$) reactions with Langmuir sorption characteristics. The model

then introduced the separate coupling coefficients, ς^{ad} and ς^{ex}, respectively, for the strain-dependence of the adsorption enthalpy of H and of the activation energy.

The relative change of the Faraday current, j^F, in response to the strain, e, was quantified by the parameter $\lambda \propto \mathrm{d}\ln j^F/\mathrm{d}e$, which emerged as a weighted sum of the two coupling coefficients, ς^{ad} and ς^{ex}. The weighting factors depended on the overpotential, ΔE. Near equilibrium ($\Delta E = 0$) it was found $\lambda = \varsigma^{ex}$, so that the current modulation was entirely governed by the strain dependence of the transition state energy (the activation energy). By contrast, the reactivity at higher overpotential magnitude also reflected the strain-dependence of the adsorption enthalpy as measured by ς^{ad}. The coupling λ far from equilibrium depended on the sign of ΔE and on the strength of H adsorption. The gold electrode was focused in analysis as the example of weak H adsorption strength.

Since the Langmuir isotherm was unrealistic inasmuch as it ignored the consequences of the adsorbate-adsorbate (H-H) interaction, a theoretical analysis inspected the H-H interaction with attention to the Heyrowsky reaction allowing for strain-dependence of the interaction enthalpy by a coupling coefficient ς^{a-a}. The expression of λ, for the Heyrowsky reaction on Au at large forward bias ($\Delta E \ll 0$), the result implied that $\lambda = \varsigma^{ex} - \varsigma^{ad}$, which coincided with the model with a Langmuir isotherm. It was remarkable that the result for the coupling strength λ was independent of ς^{a-a}, even though the adsorbate layer was concentrated. That is to say, the H-H interaction on Au surfaces affected the reactivity, but its impact on the relative change of reactivity with strain was moderate. For surfaces with strong H adsorption, a strain-dependent H-H interaction was predicted to change the reactivity-strain coupling at positive ΔE (hydrogen oxidation reaction).

The study of the HER on Au electrodes indicated that ς^{ad} and ς^{ex} were of identical sign, with a larger magnitude for ς^{ad}. The modulated Faraday current, $\iota = \mathrm{d}j^F/\mathrm{d}e$, changed its sign going with large and negative overpotential for the HER on Au. More accurately, the value of ι was negative at less negative potential of equilibrium potential of HER, which gave a meaning that the tensile strain enhanced the Faradaic current, or the surface could be regarded as more reactive, since the nominal Faraday current exhibited negative valued in the whole region of HER. At large and negative potential, the sign of parameter ι turned to positive, which meant less reactive for the metal surface by a tensile strain.

ii) Experimental verification by DECMA measurement

Experimental investigations have been also conduced to verify the theoretical model. The experimental systems in study were the 111-textured polycrystalline Au and Pt thin film electrodes in the 0.5 M concentration of H_2SO_4 solution as the most studied system in the literature.

The experiments explored an approach towards monitoring the mechanical modulation of electrocatalytic reactions by the lock-in technique of a modified DECMA to detect the mechanical modulation of the reaction current. It primarily successfully separated the modulated pseudo-capacitive current component and Faraday current component in a current-strain response experiment.

Based on the observation of Tafel plots, the Au electrode exhibited two different Tafel slopes at low and high overpotential magnitudes ($|\Delta E|$). The factor three in difference between the slopes in the respective regimes agreed with the theoretically idealized case in the model. The change in Tafel slope was an inherent feature of the Heyrowsky kinetics, where it demarcated the

transition between dilute and concentrated hydrogen coverage at the electrosorption potential, ΔE^{ad}. Consequently, the data for Au electrode gave a reasonable qualitative representation of the inherent kinetics of the Heyrowsky reaction. The similar qualitative behavior of current-strain response of Pt lent qualitative support to the discussion of the impact of strain on the reactivity at Au surface.

The main finding, that the experimental data agreed with the theoretical model based on Heyrowsky reaction kinetics for Au electrode, supported the assumptions of strain effect on the reaction rate: **a)** strain affected surface coverage of hydrogen adsorption by a strain-dependent adsorption enthalpy; **b)** strain affected exchange current density by a strain-dependent activation enthalpy. This was first quantifiable measurement and experimental report for the reactivity-strain coupling strength.

More precisely, the variation of the reactivity-strain coupling in the experiment – as measured by $\lambda(E)$ – with ΔE was found qualitatively similar for Au and Pt. The most prominent observation was a sign change of the coupling at overpotential near the ΔE^{ad}. This transition was consistent with the prediction of the model. The parameter $\lambda(E)$ under observation became approximately negative constant in the limit of large and negative overpotential. With $\lambda(E) < 0$ at large and negative overpotential (i.e., forward bias of the HER) and a transition to $\lambda(E) > 0$ when ΔE increased, the tensile strain diminished the reactivity under sufficiently large forward bias, and a transition to tensile strain enhancing the reactivity under lesser bias.

The parameter of exchange current density, j^{ex}, is mostly used to describe the reactivity of the electrode surface for an electrochemical reaction. The Au and Pt electrodes in study probed the HER on substrates with quite different adsorption strength. Pt underwent underpotential deposition (UPD) at slightly positive overpotential (adsorption enthalpy $\Delta h^{\mathrm{ad}} \lesssim 0$), which put it near to (but slightly to the left of) the peak of the volcano curve of exchange current density versus hydrogen enthalpy of adsorption. By contrast, Au was way out at very positive Δh^{ad}. Thus, these two metals may differ in respect to the impact of strain on the exchange current density. Since tensile strain made the surface more binding for H species, it shifted both Au and Pt to lesser Δh^{ad} on the graph of the volcano curve. A finite tensile strain would make Au larger j^{ex} (or more reactive) and Pt less j^{ex} (or less reactive).

The discussion of the results for Au indicated that the tensile strain decreased the activation enthalpy of Au for Heyrowsky reaction by the coupling coefficient $\varsigma^{\mathrm{ex}} > 0$. Then the exchange current density was indeed enhanced by tensile strain since $\lambda \approx \varsigma^{\mathrm{ex}}$, which was positive. However, at first sight the tensile strain here inhibited the reactivity of both metals at large and negative overpotentials by the experimental observation and the theory indicated $\lambda \approx \varsigma^{\mathrm{ex}} - \varsigma^{\mathrm{ad}}$, which took on negative values. The apparent discrepancy was related to the different strain dependence of two measures for the reactivity, namely the exchange current density on the one hand and the Faraday current at finite overpotential on the other. Yet, the different behavior of the reactivity under finite bias shows that the strain effect on the reaction kinetics was governed by additional factors, which were not appropriately measured by the exchange current alone. The significant reaction current could be only obtained at higher overpotential, where the hydrogen coverage had changed from dilute to concentrated.

Outlook

In principle, the present approach towards monitoring mechanically modulated reaction rates in electrocatalysis can be applied generally to catalyst materials and to other electrocatalytic reactions, *e.g.* oxygen reduction reaction (ORR) and the oxidation of formic acid. It thus provides a new tool for studying strain-dependent catalysis on materials surfaces and for identifying the underlying microscopic processes in the interest of developing improved catalyst materials. The present investigation of strain-dependent reactivity for metal surfaces therefore opens a helpful insight into the design of catalyst in a chemical reaction.

Many experiments in the field of electrocapillarity use the electrodes with the surface that is not perfectly flat and contain defects *e.g.* step edges, terraces. The general results for the mechanics of such rough surface [138, 139] finds that corrugation has an important effect on the way in which the surface stress is transferred into the substrate. The action of the surface stress can even invert its sign.

Yet, the relevant corrections of roughness effect are not applied in the studies of electrocapillarity. The accuracy of the experimental data in the field of strain-dependence could be further enhanced if the roughness correction is established and applied in the general experimental studies. The observations in experiments (shown in Fig. 6.1) imply that ς_E varies significantly between as-prepared and annealed states of electrode, in which the surfaces show the different roughness.
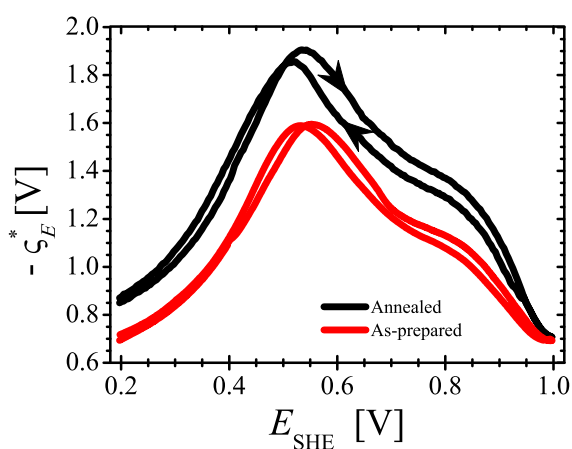

Figure 6.1: The DECMA experimental results of ς_E in 10 mM $HClO_4$ of as prepared and annealed gold electrodes within capacitive range with scan rate of 1 mV s^{-1} and at strain frequency of 20 Hz. The arrows show the sweep directions.

References

[1] G. Ertl and N. Thiele. XPS studies with ammonia synthesis catalysts. *Appl. Surf. Sci.*, 3:99, 1979.

[2] G. Ertl. Surface science and catalysis-studies on the mechanism of ammonia synthesis: The P. H. Emmett Award Address. *Catal. Rev. Sci. Eng.*, 21:201–223, 1980.

[3] G. Ertl, D. Prigge, R. Schloegl, and M. Weiss. Surface characterization of ammonia synthesis catalysts. *J. Catal.*, 79:359–377, 1983.

[4] P. S. Weiss. 2007 nobel prizes span nanoscience from ideas and motivation to applications. *ACS Nano*, 1:239–240, 2007.

[5] F. C. Meunier. Bridging the gap between surface science and industrial catalysis. *ACS Nano*, 2:2441–2444, 2008.

[6] B. Hammer and J.K. Nørskov. Electronic factors determining the reactivity of metal surfaces. *Surf. Sci.*, 343:211–220, 1995.

[7] M. Haruta. Size- and support- dependency in the catalysis of gold. *Catal. Today*, 36:153–166, 1997.

[8] P. Dolle, R. Baudoing-Savois, M. De Santis, M.C. Saint-Lager, M. Abel, J.C. Bertolini, and P. Delichère. Strained Pd films, by epitaxial growth on Au(110), to control catalytic properties. *Surf. Sci.*, 518:1–13, 2002.

[9] S.K. Shaikhutdinov, R. Meyer, M. Naschitzki, M. Bäumer, and H.-J. Freund. Size and support effects for CO adsorption on gold model catalysts. *Catal. Lett.*, 86:211–219, 2003.

[10] H.-J. Freund. Model studies on heterogeneous catalysts at the atomic level. *Catal. Today*, 100:3–9, 2005.

[11] B. R. Cuenya. Synthesis and catalytic properties of metal nanoparticles: Size, shape, support, composition, and oxidation state effects. *Thin Solid Films*, 518:3127–3150, 2010.

[12] H. Pan and C. M. Wai. One-step synthesis of size-tunable rhodium nanoparticles on carbon nanotubes: A study of particle size effect on hydrogenation of xylene. *J. Phys. Chem. C*, 114:11364–11369, 2010.

[13] M. Mavrikakis, P. Stoltze, and J.K. Nørskov. Making gold less noble. *Catal. lett.*, 64:101, 2000.

[14] L.A. Kibler, A.M. El-Aziz, and D.M. Kolb. Electrochemical behaviour of pseudomorphic overlayers: Pd on Au(111). *J. Mol. Catal. A: Chem.*, 199:57–63, 2003.

[15] L. A. Kibler, A. M. El-Aziz, R. Hoyer, and D. M. Kolb. Tuning reaction rates by lateral strain in a palladium monolayer. *Angew. Chem. Int. Ed.*, 44:2080–2084, 2005.

[16] W.M.H. Sachtler and P.V.D. Plank. The role of individual surface atoms in chemisorption and catalysis by nickel-copper alloys. *Surf. Sci.*, 18:62–79, 1969.

[17] J.H. Sinfelt. Heterogeneous catalysis: some recent developments. *Science*, 195:641–646, 1977.

[18] J. H. Sinfelt. Catalysis by alloys and bimetallic clusters. *Acc. Chem. Res.*, 10:15–20, 1977.

[19] J. Greeley and M. Mavrikakis. Alloy catalysts designed from first principles. *Nat. Mater.*, 3:810–815, 2004.

[20] J.L. Fernández, D.A. Walsh, and A.J. Bard. Thermodynamic guidelines for the design of bimetallic catalysts for oxygen electroreduction and rapid screening by scanning electrochemical microscopy. M-Co (M: Pd, Ag, Au). *J. Am. Chem. Soc.*, 127:357–365, 2005.

[21] S. Alayoglu, A.U. Nilekar, M. Mavrikakis, and B. Eichhorn. RuPt coreshell nanoparticles for preferential oxidation of carbon monoxide in hydrogen. *Nat. Mater.*, 7:333–338, 2008.

[22] F. Tao, M.E. Grass, Y. Zhang, D.R. Butcher, J.R. Renzas, Z. Liu, J.Y. Chung, B.S. Mun, M. Salmeron, and G.A. Somorjai. Reaction-driven restructuring of Rh-Pd and Pt-Pd core-shell nanoparticles. *Science*, 322:932–934, 2008.

[23] X. Teng, D. Black, N.J. Watkins, Y. Gao, and H. Yang. Platinum-maghemite core-shell nanoparticles using a sequential synthesis. *Nano Lett.*, 3:261–264, 2003.

[24] B. Hammer and J.K. Nørskov. Electronic factors determining the reactivity of metal surfaces. *Surf. Sci.*, 343:211–220, 1995.

[25] A. Ruban, B. Hammer, P. Stoltze, H.L. Skriver, and J.K. Nørskov. Surface electronic structure and reactivity of transition and noble metals. *J. Mol. Catal. A: Chem.*, 115:421–429, 1997.

[26] M. Mavrikakis, B. Hammer, and J. K. Nørskov. Effect of strain on the reactivity of metal surfaces. *Phys. Rev. Lett.*, 81:2819–2822, 1998.

[27] T. Bligaard, J. K. Nørskov, S. Dahl, J. Matthiesen, C. H. Christensen, and J. Sehested. The Brønsted-Evans-Polanyi relation and the volcano curve in heterogeneous catalysis. *J. Catal.*, 224:206–217, 2004.

[28] J. K. Nørskov, T. Bligaard, A. Logadottir, J. R. Kitchin, J. G. Chen, S. Pandelov, and U. Stimming. Trends in the exchange current for hydrogen evolution. *J. Electrochem. Soc.*, 152:J23–J26, 2005.

[29] S. Sakong and A. Groß. Density functional theory study of the partial oxidation of methanol on copper surfaces. *J. Catal.*, 231:420–429, 2005.

[30] M. Gsell, P. Jakob, and D. Menzel. Effect of substrate strain on adsorption. *Science*, 280:717–720, 1998.

[31] A. Schlapka, M. Lischka, A. Groß, U. Käsberger, and P. Jakob. Surface strain *versus* substrate interaction in heteroepitaxial metal layers: Pt on Ru (0001). *Phys. Rev. Lett.*, 91:016101, 2003.

[32] J. Weissmüller, R. N. Viswanath, L. A. Kibler, and D.M. Kolb. Impact of surface mechanics on the reactivity of electrodes. *Phys. Chem. Chem. Phys.*, 13:2114–2117, 2011.

[33] M.M. Günter, T. Ressler, B. Bems, C. Büscher, T. Genger, O. Hinrichsen, M. Muhler, and R. Schlögl. Implication of the microstructure of binary Cu/ZnO catalysts for their catalytic activity in methanol synthesis. *Catal. Lett.*, 71:37–44, 2001.

[34] M. Shao, P. Liu, J. Zhang, and R. Adzic. Origin of enhanced activity in palladium alloy electrocatalysts for oxygen reduction reaction. *J. Phys. Chem. B*, 111:6772–6775, 2007.

[35] L.A. Kibler. Dependence of electrocatalytic activity on film thickness for the hydrogen evolution reaction of Pd overlayers on Au (111). *Electrochim. Acta*, 53:6824–6828, 2008.

[36] P. Strasser, S. Koh, T. Anniyev, J. Greeley, K. More, C. Yu, Z. Liu, S. Kaya, D. Nordlund, H. Ogasawara, M.F. Toney, and A. Nilsson. Lattice-strain control of the activity in dealloyed coreshell fuel cell catalysts. *Nat. Chem.*, 2:454–460, 2010.

[37] F. Weigend, F. Evers, and J. Weissmüller. Structural relaxation in charged metal surfaces and cluster ions. *Small*, 2:1497–1503, 2006.

[38] Y. Umeno, C. Elsässer, B. Meyer, P. Gumbsch, M. Nothacker, J. Weissmüller, and F. Evers. Ab initio study of surface stress response to charging. *Europhys. Lett.*, 78:13001, 2007.

[39] Y. Umeno, C. Elsässer, B. Meyer, P. Gumbsch, M. Nothacker, and J. Weissmüller. Reversible relaxation at charged metal surfaces: An ab initio study. *Europhys. Lett.*, 84:13002, 2008.

[40] J.-M. Albina, C. Elsässer, J. Weissmüller, P. Gumbsch, and Y. Umeno. Ab initio investigation of surface stress response to charging of transition and noble metals. *Phys. Rev. B*, 85:125118, 2012.

[41] A.Ya. Gokhshtein. The estance method. *Russ. Chem. Rev.*, 44:921–932, 1975.

[42] G. Valincius. Electrocapillary equations of solid electrodes. *J. Electroanal. Chem.*, 478:40–49, 1999.

[43] M.Smetanin, D.Kramer, S.Mohanan, U. Herr, and J. Weissmüller. Response of the potential of a gold electrode to elastic strain. *Phys. Chem. Chem. Phys.*, 11:9008–9012, 2009.

[44] M.Smetanin, Q. Deng, D.Kramer, S.Mohanan, U. Herr, and J. Weissmüller. Reply to the 'Comment on "Response of the potential of a gold electrode to elastic strain" ' by Á. Horváth, G. Nagy and R. Schiller. *Phys. Chem. Chem. Phys.*, 12:7291–7292, 2010.

[45] H. Ibach, C.E. Bach, M. Giesen, and A. Grossmann. Potential-induced stress in the solid-liquid interface: Au (111) and Au (100) in an HClO$_4$ electrolyte. *Surf. Sci.*, 375:107–119, 1997.

[46] W. Haiss, R. J. Nichols, J. K. Sass, and K. P. Charle. Linear correlation between surface stress and surface charge in anion adsorption on Au (111). *J. Electroanal. Chem.*, 452:199–202, 1998.

[47] N. Vasiljevic, T. Trimble, N. Dimitrov, and K. Sieradzki. Electrocapillarity behavior of Au(111) in SO$_4^{2-}$ and F$^-$. *Langmuir*, 20:6639–6643, 2004.

[48] M. Smetanin, R. N. Viswanath, D. Kramer, D. Beckmann, T. Koch, L. A. Kibler, and J. Weissmüller. Surface stress-charge response of a (111)-textured gold electrode under conditions of weak ion adsorption. *Langmuir*, 24:8561–8567, 2008.

[49] J. Weissmüller, R. N. Viswanath, D. Kramer, P. Zimmer, R. Würschum, and H. Gleiter. Charge-induced reversible strain in a metal. *Science*, 300:312–315, 2003.

[50] M. C. Lafouresse, U. Bertocci, C. R. Beauchamp, and G. R. Stafford. Spectroscopy using cantilever curvature simultaneous electrochemical and mechanical impedance. *J. Electrochem. Soc.*, 59:H816–H822, 2012.

[51] D. Kramer and J. Weissmüller. A note on surface stress and surface tension and their interrelation via Shuttleworth's equation and the Lippmann equation. *Surf. Sci.*, 601:3042–3051, 2007.

[52] Á. Horváth and R. Schiller. The effect of mechanical stress on the potential of the Ag/Ag$^+$ electrode. *Phys. Chem. Chem. Phys.*, 3:2662–2667, 2001.

[53] M. Smetanin. *Mechnicas of Electrified Interfaces in Diluted Electrolytes*. PhD thesis, Universität des Saarlandes, 2010.

[54] M. Smetanin, Q. Deng, and J. Weissmüller. Dynamic electro-chemo-mechanical analysis during cyclic voltammetry. *Phys. Chem. Chem. Phys.*, 13:17313–17322, 2011.

[55] Q. Deng, M. Smetanin, and J. Weissmüller. Dynamic electro-chemo-mechanical analysis. *ECS Meeting Abstract*, MA2012-01(23):959, 2012.

[56] Q. Deng and J. Weissmüller. Electrocapillary coupling during electrosorption. *Langmiur*, submitted, 2014.

[57] Q. Deng, M. Smetanin, and J. Weissmüller. Mechanical modulation of reaction rates in electrocatalysis. *J. Catal.*, 309:351–361, 2014.

[58] Allen J. Bard and Larry R. Faulkner. *Electrochemical Methods: Fundamentals and Applications*. John Wiley, New York, 2001.

[59] Allen J. Bard, György Inzelt, and Fritz Scholz. *Electrochemical Dictionary*. Springer, Berlin, 2008.

[60] Mark E. Orazem and Bernard Tribollet. *Electrochemical impedance spectroscopy*. John Wiley, Hoboken, 2008.

[61] Eliezer Gileadi. *Electrode Kinetics for Chemists, Chemical Engineers, and Materials Scientists*. VCH, New York, 1993.

[62] G. Gouy. Sur la constitution de la charge electrique a la surface d'un electrolute. *J. Phys. Radium (France)*, 9:457–468, 1910.

[63] Y. Oren, H. Tobias, and A. Soffer. The electrical double-layer of carbon and graphite electrodes: Part I. dependence on electrolyte type and concentration. *J. Electroanal. Chem.*, 162:87, 1984.

[64] D.L. Chapman. A contribution to the theory of electrocapillarity. *Phil. Mag.*, 25:475–481, 1913.

[65] Cynthia G. Zoski. *Handbook of Electrochemistry*. Elsevier, Amsterdam, 2007.

[66] John O´M Bockris, Amulya K. N. Reddy, and Maria Gamboa-Aldeco. *Modern Electrochemistry: Ionics*. Kluwer Academic, New York, 2002.

[67] John O´M Bockris, Amulya K. N. Reddy, and Maria Gamboa-Aldeco. *Modern Electrochemistry: Fundamentals of Electrodics*. Kluwer Academic, New York, 2002.

[68] International Union of Pure and Applied Chemistry (IUPAC). *Compendium of Chemical Terminology, 2nd ed. (the "Gold Book")*. Blackwell Scientific Publications, Oxford, 1997.

[69] *http://en.wikipedia.org/wiki/Nernst_equation*.

[70] J. Weissmüller. *Electrocapillarity of Solids and its Impact on Heterogeneous Catalysis, in Electrocatalysis: Theoretical Foundations and Model Experiments, R.V Alkire, L. Kibler, D.M. Kolb, J. Lipkowski (Eds.)*, volume 14. Wiley-VCH, Weinheim, Germany, 2013.

[71] J. Weissmüller and D. Kramer. Balance of force at curved solid metal-liquid electrolyte interfaces. *Langmuir*, 21:4592–4603, 2005.

[72] R.J. Needs and M. Mansfield. Calculations of the surface stress tensor and surface energy of the (111) surfaces of iridium, platinum and gold. *J. Phys.: Condens. Matter*, 1:7555–7563, 1989.

[73] R. Cammarata. Surface and interface stress effects in thin films. *Prog. Surf. Sci.*, 46:1–38, 1994.

[74] H. Ibach. The role of surface stress in reconstructure, expitaxial growth and stabilization of mesoscopic structures. *Surf. Sci. Rep.*, 29:193–263, 1997.

[75] W. Schmickler and E. Leiva. A note on the surface stress and tension of solid metal electrodes. *J. Electroanal. Chem.*, 453:61–67, 1998.

[76] N.M. Marković, B.N. Grgur, and P.N. Ross. Temperature-dependent hydrogen electro-chemistry on platinum low-index single-crystal surfaces in acid solutions. *J. Phys. Chem. B*, 101:5405–5413, 1997.

[77] B.E. Conway and L. Bai. Determination of adsorption of OPD H species in the cathodic hydrogen evolution reaction at Pt in relation to electrocatalysis. *J . Electroanal. Chem.*, 198:149–175, 1986.

[78] J. O´M. Bockris and D.F.A. Koch. Comparative rates of the electrolytic evolution of hydrogen and deuterium on iron, tungsten and platinum. *J. Phys. Chem.*, 65:1941–1948, 1961.

[79] M.C. Tavares, S.A.S. Machado, and L.H. Mazo. Study of hydrogen evolution reaction in acid medium on Pt microelectrodes. *Electrochim. Acta*, 46:4359–4369, 2001.

[80] M.Ø. Pedersen, S. Helveg, A. Ruban, I. Stensgaard, E. Lægsgaard, J.K. Nørskov, and F. Besenbacher. How a gold substrate can increase the reactivity of a Pt overlayer. *Surf. Sci.*, 426:395–409, 1999.

[81] H. Kita, S. Ye, and Y. Gao. Mass transfer effect in hydrogen evolution reaction on Pt single-crystal electrodes in acid solution. *J. Electroanal. Chem.*, 334:351–357, 1992.

[82] A.T. Khun and M. Byrne. The hydrogen- and deuterium-evolution reactions on gold in acid solution. *Elcctrochim. Acta.*, 16:391–399, 1971.

[83] G.M. Schmid. Hydrogen overvoltage on gold. *Electrochim. Acta.*, 12:449–459, 1967.

[84] J. Perez, E.R. Gonzalez, and H.M. Villullas. Hydrogen evolution reaction on gold single-crystal electrodes in acid solutions. *J. Phys. Chem. B*, 102:10931–10935, 1998.

[85] T. Sasaki and A. Matsuda. Mechanism of hydrogen evolution reaction on gold in aqueous sulfuric acid and sodium hydroxide. *J. Res. Inst. Catalysis Hokkaido University*, 29:113–132, 1981.

[86] P. Ferrin, S. Kandoi, A.U. Nilekar, and M. Mavrikakis. Hydrogen adsorption, absorption and diffusion on and in transition metal surfaces: A DFT study. *Surf. Sci.*, 606:679–689, 2012.

[87] B.E. Conway, J.H. Barber, L. Gao, and S.Y. Qian. Effects of catalyst poisons on UPD and OPD H coverage at H_2-evolving cathodes in relation to H sorption into metals. *J. Alloys Compd.*, 253:475–480, 1997.

[88] Y. Xu. The hydrogen evolution reaction on single crystal gold electrode. *Int. J. Hydrogen Energy*, 34:77–83, 2009.

[89] E. Rasten. *Electrocatalysis in Water Electrolysis with Solid Polymer Electrolyte*. PhD thesis, Norwegian University of Science and Technology, 2001.

[90] B.E. Conway and G. Jerkiewicz. Relation of energies and coverages of underpotential and overpotential deposited H at Pt and other metals to the 'volcano curve' for cathodic H_2 evolution kinetics. *Electrochimica Acta*, 45:4075–4083, 2000.

[91] J. Barber, S. Morin, and B.E. Conway. Specificity of the kinetics of H_2 evolution to the structure of single-crystal Pt surfaces, and the relation between opd and upd H. *J. Electroanal. Chem.*, 446:125–138, 1998.

[92] G. Jerkiewicz. Electrochemical hydrogen adsorption and absorption. Part 1: Underpotential deposition of hydrogen. *Electrocatal.*, 1:179–199, 2010.

[93] R. Parsons. The rate of electrolytic hydrogen evolution and the heat of adsorption of hydrogen. *Trans. Faraday Soc.*, 54:1053–1063, 1958.

[94] M.R. Gennero de Chialvo and A.C. Chialvo. Hydrogen evolution reaction: analysis of the Volmer-Heyrovsky-Tafel mechanism with a generalized adsorption model. *J. Electroanal. Chem.*, 372:209–223, 1994.

[95] M. Bhardwaj and R. Balasubramaniam. Uncoupled non-linear equations method for determining kinetic parameters in case of hydrogen evolution reaction following Volmer-Heyrovsky-Tafel mechanism and Volmer-Heyrovsky mechanism. *Int. J. Hydrogen Energy*, 33:2178–2188, 2008.

[96] S. Trasatti. Work function, electronegativity, and electrochemical behaviors of metals: electrolytic hydrogen evolution in acid solutions. *J. Electroanal. chem.*, 39:163–184, 1972.

[97] G. J. Brug, M. Sluyters-Rehbach, J. H. Sluters, and A. Hamelin. The kinetics of the reduction of protons at polycrystalline and monocrystalline gold electrodes. *J. Electroanal. Chem.*, 181:245–266, 1984.

[98] UBE Europe GmbH. Technical information UPILEX-S. *http://www.ube.de/index.html*.

[99] L.J. Matienzo and F.D. Egitto. Polymer oxidation downstream from oxygen microwave plasmas. *Polym. Degrad. Stabil.*, 35:181–192, 1992.

[100] R.N. Viswanath, D. Kramer, and J. Weissmüller. Variation of the surface stress-charge coefficient of platinum with electrolyte concentration. *Langmuir*, 21:4604–4609, 2005.

[101] R.N. Viswanath, D. Kramer, and J. Weissmüller. Adsorbate effects on the surface stress-charge response of platinum electrodes. *Electrochim. Acta.*, 53:2757–2767, 2008.

[102] G. R. Stafford and U. Bertocci. *In situ* stress and nanogravimetric measurements during hydrogen adsorption/absorption on Pd overlayers deposited onto (111)-textured Au. *J. Phys. Chem. C*, 113:13249–13256, 2009.

[103] J. W. Shin, U. Bertocci, and G. R. Stafford. *In situ* stress measurement during hydrogen sorption on ultrathin (111)-textured Pd films in alkaline electrolyte. *J. Electrochem. Soc.*, 158:F127–F134, 2011.

[104] R. Behrisch. *Sputtering by Particle Bombardment*. Springer, Berlin, 1981.

[105] Physik Instrumente (PI) GmbH. Piezoelectrics in positioning: Tutorial on piezotechnology in nanopositioning applications. *http://www.physikinstrumente.com*.

[106] J. Dolbow and M. Gosz. Effect of out-of-plane properties of a polyimide on the stress fields in microelectronic structures. *Mechanics of Materials*, 23:314–321, 1996.

[107] B. Özkaya, S.R. Saranu, S. Mohanan, and U. Herr. Effects of uniaxial stress on the magnetic properties of thin films and GMR sensors prepared on polyimide substrates. *Phys. Stat. Sol. (a)*, 205:1876–1879, 2008.

[108] S. Djaziri, D. Faurie, E. Le Bourhis, Ph. Goudeau, P.-O. Renault, C. Mocuta, D. Thiaudière, and F. Hild. Deformation modes of nanostructured thin film under controlled biaxial deformation. *Thin Solid Films*, 530:30–34, 2013.

[109] V. Tabard-Cossa, M. Godin, I.J. Burgess, T. Monga, R.B. Lennox, and P. Grütter. Microcantilever-based sensors: effect of morphology, adhesion, and cleanliness of the sensing surface on surface stress. *Anal. Chem.*, 79:8136–8143, 2007.

[110] H.B. Callen. *Thermodynamics and an Introduction to Thermostatistics*. Wiley, New York, 1985.

[111] H. Angerstein-Kozlowska, B.E. Conway, A. Hamelin, and L. Stoicoviciu. Flementary steps of electrochemical oxidation of singlecrystal planes of Au: Part II. A chemical and structural basis of oxidation of the (111) plane. *J. Electroanal. Chem.*, 228:429–453, 1987.

[112] J.R. Macdonald. *Impedance Spectroscopy*. Wiley, New York, 1987.

[113] Ray G. Powell. *Introduction to Electric Circuits*. Butterworth-Heinemann, London, 1995.

[114] Z. Shi, J. Lipkowski, M. Gamboa, P. Zelenay, and A. Wieckowski. Investigations of SO_4^{2-} adsorption at the Au(111) electrode by chronocoulometry and radiochemistry. *J. Electroanal. Chem.*, 366:311–326, 1994.

[115] P.P. Craig. Direct observation of stress-induced shifts in contact potentials. *Phys. Rev. Lett.*, 22:700–703, 1969.

[116] D. M. Kolb and J. Schneider. Surface reconstruction in electrochemistry:Au (100)-(5×20), Au (111)-(1×23) and Au (110)-(1×2). *Electrochim. Acta*, 31:929–936, 1986.

[117] Z. Shi, J. Lipkowski, M. Gamboa, P. Zelenay, and A. Wieckowski. Investigations of SO_4^{2-} adsorption at the Au (111) electrode by chrono-coulometry and radiochemistry. *J. Electroanal. Chem.*, 366:317–326, 1994.

[118] A.Y. Lozovoi and A. Alavi. Reconstruction of charged surfaces: General trends and a case study of Pt (110) and Au (110). *Phys. Rev. B: Condens. Matter*, 68:245416, 2003.

[119] H. Jin, S. Parida, D. Kramer, and J. Weissmüller. Sign-inverted surface stress-charge response in nanoporous gold. *Surf. Sci.*, 602:3588–3594, 2008.

[120] B.E. Conway and L. Bai. State of adsorption and coverage by overpotential-deposited H in the H_2 evolution reaction at Au and Pt. *Electrochim. Acta.*, 31:1013–1024, 1986.

[121] W. Sheng, H.A. Gasteiger, and Y. Shao-Horn. Hydrogen oxidation and evolution reaction kinetics on platinum: acid *vs* alkaline electrolytes. *J. Electrochem. Soc.*, 157:B1529–B1536, 2010.

[122] L.A. Kibler. Hydrogen electrocatalysis. *Chem. Phys. Chem.*, 7:985–991, 2006.

[123] K. Kunimatsu, T. Senzaki, G. Samjeské, M. Tsushima, and M. Osawa. Hydrogen adsorption and hydrogen evolution reaction on a polycrystalline Pt electrode studied by surface-enhanced infrared absorption spectroscopy. *Electrochim. Acta.*, 52:5715–5724, 2007.

[124] S. A. Vilekar, I. Fishtik, and R. Dattaz. Kinetics of the hydrogen electrode reaction. *J Electrochem. Soc.*, 157:B1040–B1050, 2010.

[125] N.M. Marković and P.N Ross Jr. Surface science studies of model fuel cell eletrocatalysts. *Surf. Sci. Rep.*, 45:117–229, 2002.

[126] E. Skúlason, G.S. Karlberg, J. Rossmeisl, T. Bligaard, J. Greeley, H. Jónsson, and J. K. Nørskov. Density functional theory calculations for the hydrogen evolution reaction in an electrochemical double layer on the Pt(111) electrode. *Phys. Chem. Chem. Phys.*, 9:3241–3250, 2007.

[127] R. Fowler and E.A. Guggenheim. *Statistical Thermodynamics*. Cambridge University Press, Cambridge UK, 1960.

[128] A. Sarapuua, K. Tammeveskia, T.T. Tennoa, V. Sammelselgb, K. Kontturic, and D. J. Schiffrin. Electrochemical reduction of oxygen on thin-film Au electrodes in acid solution. *Electrochem. Commun.*, 3:446–450, 2001.

[129] J.M. Delgado, J.M. Orts, J.M. Pérez, and A. Rodes. Sputtered thin-film gold electrodes for in situ ATR-SEIRAS and SERS studies. *J. Electroanal. Chem.*, 617:130–140, 2008.

[130] M.N. Dešić, M.M. Popovoć, M.D. Obradović, L.M. Vračar, and B.N. Grgur. Study of gold-platinum and platinum-gold surface modification and its influence on hydrogen evolution and oxygen reduction. *J. Serb. Chem. Soc.*, 2:231–242, 2005.

[131] B.E. Conway and B.V. Tilak. Interfacial processes involving electrocatalytic evolution and oxidation of H_2, and the role of chemisorbed H. *Electrochim. Acta.*, 47:3571–3594, 2002.

[132] N. Pentland, J. O´M. Bockris, and E. Sheldon. Hydrogen evolution reaction on copper, gold, molybdenum, palladium, rhodium, and iron. *J. Electrochem. Soc.*, 104:182–194, 1957.

[133] E. Santos, A. Lundin, K. Pötting, P. Quaino, and W. Schmickler. Model for the electrocatalysis of hydrogen evolution. *Phys. Rev. B*, 79:235436, 2009.

[134] W. Haiss. Surface stress of clean and adsorbate-covered solids. *Rep. Prog. Phys.*, 64:591–648, 2001.

[135] J.N. Brønsted. Acid and basic catalysis. *Chem. Rev.*, 5:231–338, 1928.

[136] M.G. Evans and M. Polanyi. Inertia and driving force of chemical reactions. *Trans. Faraday Soc.*, 34:11–24, 1938.

[137] J. K. Nørskov, T. Bligaard, A. Logadottir, S. Bahn, L.B. Hansen, M. Bollinger, H. Bengaard, B. Hammer, Z. Sljivancanin, M. Mavrikakis, Y. Xu, S. Dahl, and C.J.H. Jacobsen. Universality in heterogeneous catalysis. *J. Catal.*, 209:275–278, 2002.

[138] J. Weissmüller and H. Duan. Cantilever bending with rough surfaces. *Phys. Rev. Lett.*, 101:146102, 2008.

[139] Y. Wang, J. Weissmüller, and H. Duan. Mechanics of corrugated surfaces. *J. Mech. Phys. Sol.*, 58:1552–1566, 2010.

Curriculum Vitae

Personal Data

Name   DENG
First Name   Qibo
Date of Birth 02 September, 1985
Place of Birth Guangxi, People's Republic of China

Education

09.1992 – 07.1997   Elementary school in Guangxi, Nankang Central Elementary School

09.1997 – 07.2000   Junior high school in Guangxi, Nankang Middle School

09.2000 – 07.2003   High school in Guangxi, Nankang Middle School

09.2003 – 07.2007   Undergraduate study at the Department of Mechanics,
Beijing Institute of Technology, Beijing ,China
Degree: Bachelor of Engineering
Title of Thesis: *Computational Study of Electromagnetic Metamaterials: Transmission Line*

09.2007 – 07.2009   Graduate study at the Department of Mechanics,
Beijing Institute of Technology, Beijing, China
Degree: Master of Engineering
Title of Thesis: *The Design and Fabrication of Multifunction Electromagnetic Materials*

09.2009 – 10.2010   Scientific research at the Institute of Nanotechnology,
Karlsruhe Institute of Technology, Karlsruhe, Germany

10.2010 – 04.2014   Ph.D study at the Institute of Materials Physics and Technology,
Hamburg University of Technology, Hamburg, Germany
Title of Thesis: *Dynamic Electro-Chemo-Mechanical Analysis at the Metal-Electrolyte Interface*